New methods of observation and characterization of fractional quantum Hall states

Kyrylo Snizhko

This thesis is submitted in partial fulfilment of the requirements for the degree of Doctor of Philosophy

April 23, 2014

To the virtue of simplicity of explanation,

which is always a good thing to aim at,

but rarely an easy thing to achieve

Abstract

New methods of observation and characterization of fractional quantum Hall states

Kyrylo Snizhko

Thesis submitted for the degree of Doctor of Philosophy in April 2014

In this work we study new ways to observe and characterize specific fractional quantum Hall (FQH) states.

In the first chapter we investigate the possibility to realize specific FQH states in bilayer graphene (BLG). BLG is a novel material in which the electron-electron interaction can be tuned with the help of external parameters. This allows one to make one or another FQH state favourable. We develop a framework for theoretical investigation of the stability of FQH states in BLG. We apply our framework to investigate the stability of the Pfaffian state. We find that the region in which our framework allows for making reliable predictions is quite restricted because of Landau level mixing effects. However, within that region we find the conditions under which the Pfaffian is more stable than in the conventional "non-relativistic" systems. These conditions can, in principle, be realized experimentally.

In the second chapter we focus on characterizing the FQH states with the help of measurements of the noise of the electric current tunnelling between two FQH edges. We develop a theoretical framework allowing for analysing such data, and test it by successfully applying it to describe the results of the experiment [Bid et al., Nature **466**, 585 (2010)]. We further develop our framework and show that it is possible to determine the tunnelling quasiparticle scaling dimension from such measurements. We also investigate experimental conditions necessary for this.

Contents

Abstract **2**

Contents **3**

Declaration **7**

Acknowledgements **8**

List of Figures **10**

List of abbreviations and conventions **17**

Introduction **19**

1 Ways to observe specific fractional quantum Hall states in bilayer graphene **22**

1.1 Numerical diagonalization approach to the quantum Hall effect in non-relativistic systems 23

1.1.1 Problem of a free non-relativistic electron in magnetic field . 23

1.1.2 Interaction of two electrons in a non-relativistic Landau level 27

1.1.3 Many-particle problem 30

1.1.3.1 Examples of trial wave functions 32

1.1.4 Summary of the section 36

1.2 Numerical diagonalization approach to the quantum Hall effect in bilayer graphene (single Landau level approximation) 36

1.2.1 Bilayer graphene. Hamiltonian of a free electron in bilayer graphene . . . 36
1.2.2 Problem of a free electron in magnetic field (bilayer graphene) 38
1.2.3 Interaction of two electrons in a Landau level of bilayer graphene . . . 41
1.2.4 Summary of the section . . . 44
1.3 Deviations from the single Landau level approximation in bilayer graphene . . . 45
1.3.1 Effects important in bilayer graphene . . . 45
1.3.1.1 Vacuum polarization . . . 46
1.3.1.2 Landau level mixing and population reversal . . . 47
1.3.1.3 Renormalization of pseudopotentials due to virtual hopping . . . 48
1.3.1.4 General plan for numerical study of a fractional QHE in bilayer graphene . . . 49
1.3.2 Effects important in bilayer graphene: calculation details . . 50
1.3.2.1 Calculation of the polarization function . . . 50
1.3.2.2 Population reversal of Landau levels and level mixing 53
1.3.2.3 Calculation of corrections to the SLLA pseudopotentials due to virtual hopping . . . 57
1.3.3 Summary of the section . . . 60
1.4 Possibility to observe the Moore-Read state in bilayer graphene . . 60
1.5 Summary of the chapter . . . 66

2 Characterization of fractional quantum Hall states with the help of tunnelling current noise measurements 67

2.1 $\nu = 2/3$: counterflowing neutral mode and its properties from tunnelling current noise measurements . . . 68
2.1.1 Introduction . . . 68
2.1.2 Description of the experiment [1] . . . 69

2.1.3 Theoretical picture of the experiment 71
2.1.4 Formalism of the edge field theory 73
2.1.4.1 General formalism 73
2.1.4.2 The minimal model of the $\nu = 2/3$ QH edge 77
2.1.4.3 Tunnelling of quasiparticles across the QPC 78
2.1.5 Calculation of observable quantities 79
2.1.5.1 Tunnelling rate 79
2.1.5.2 Excess noise 80
2.1.5.3 Noise to tunnelling rate ratio 82
2.1.6 Comparison with the experiment 84
2.1.7 Discussion 86
2.1.8 Summary of the section 92
2.2 Tunnelling quasiparticle's scaling dimension from tunnelling current noise measurements 92
2.2.1 Introduction 92
2.2.2 Scaling dimension from the noise to tunnelling rate ratio . . 94
2.2.2.1 What experimental conditions are necessary for successful extraction of the scaling dimension? . . . 95
2.2.3 Exact answers for $\nu = 1/3$ and the conditions to extract the scaling dimension by perturbative formulae 99
2.2.4 Summary of the section 106

Conclusions **107**

A Appendices related to Chapter 1 **108**
A.1 Derivation of the expression for pseudopotentials through the Fourier transform of the interaction potential 108
A.2 Full Hartree energy of a Landau level 111
A.3 Peculiarities of calculations of virtual hopping corrections 115
A.4 Supplemental material 118

B Appendices related to Chapter 2 **125**

B.1 Useful one-edge correlation functions 125

B.2 Tunnelling current 127

B.3 Tunnelling current (continued) 128

B.4 Noise 129

B.5 Noise — the TT term 130

B.6 Noise — the 0T term 131

B.7 Excess noise 133

B.8 Putting things together 134

B.9 How general are the answers of the subsection 2.1.5? 134

B.10 Large I_s asymptotic behaviour of the noise to tunnelling rate ratio . 136

B.11 Analytic expressions for NtTRR for equal temperatures of the upper and the lower edges 137

Bibliography **139**

Declaration

This thesis is a result of the author's original work and has not been submitted in whole or in part for the award of a higher degree elsewhere. This thesis documents the work carried out between November 2010 and April 2014 at Lancaster University, UK, under the supervision of Dr. V. Cheianov.

The list of author's relevant publications:

1. Kyrylo Snizhko, Vadim Cheianov, and Steven H. Simon "Importance of interband transitions for the fractional quantum Hall effect in bilayer graphene", Phys. Rev. B **85**, 201415(R) (2012).
   DOI: http://dx.doi.org/10.1103/PhysRevB.85.201415
   Copyright (2012) by the American Physical Society.

2. O. Shtanko, K. Snizhko, and V. Cheianov "Non-equilibrium noise in transport across a tunneling contact between $\nu = 2/3$ fractional quantum Hall edges", Phys. Rev. B **89**, 125104 (2014).
   DOI: http://dx.doi.org/10.1103/PhysRevB.89.125104

In both of the publications, the author's contribution to the research strategy, theoretical calculations, and the article text has been significant.

Chapter 1 of the present thesis presents in more detail the research published in the article 1 (as numbered in the list above) with some amendments and corrections. Section 2.1 with appendices referenced in it essentially copies the article 2. The rest of the thesis has not been published anywhere yet, and the author's contribution to it has been dominant.

Kyrylo Snizhko

April 23, 2014

Acknowledgements

I do not really like writing acknowledgements, preferring to express my gratefulness in person. However, writing this thesis turned out to be quite a challenging task with lots of skills needed to complete it. Therefore, I deem this to be a good place to say "thank you" to people who helped me get here, in one or another way.

First of all, I would like to thank my adviser Dr. Vadim Cheianov, from whom I learned a lot and without whom this work would not be possible.

I would also like to thank Dr. Oleksii Boyarsky, my former adviser who I worked with on my Bachelor's thesis, who also influenced me significantly (and who actually introduced me to Dr. Vadim Cheianov).

In respect of the present work, I thank Prof. Vladimir Fal'ko for useful discussions relating to the work of chapter 1. I thank the authors of DiagHam code I used for numerical diagonalization, especially Dr. Nicolas Regnault who patiently answered all my stupid questions on the code usage (and not so stupid ones as well). I thank Prof. Moty Heiblum and his group in Weizmann Institute of Science for giving me an opportunity to present and discuss the work of chapter 2. Special thanks to Ms. Anna Grivnin, a member of Prof. Heiblum's group, for useful discussions regarding the results of section 2.2. I greatly thank my co-authors on the articles upon which part of this thesis is based: Prof. Steve Simon and Mr. Oles' Shtan'ko.

I feel deeply obliged to Physics Department of Taras Shevchenko National University of Kyiv, especially to the Quantum Field Theory chair, especially to Prof. Stanislav Vilchynskyy and to Dr. Eduard Gorbar. I cannot avoid mentioning Scientific and Educational Center at Bogolyubov Institute for Theoretical Physics in Kyiv and its heart Dr. Vitaly Shadura. A huge part of my physics-related knowledge comes from these two institutions.

I would also like to express gratitude to my school teachers including (but not limited to) Alexander Shamovich (mathematics), Oleksii Ovsyannikov (physics),

Alexey Rozenwein (physics), Naum Reznichenko (literature!), Lidiya Korshak, Lyubov' Dusanskaya.

I thank Lancaster University for the nice atmosphere I have found here. I am grateful to my friends in Lancaster, in Kyiv and in other places for the great atmosphere I have found in Lancaster, in Kyiv and in other places.

Among the last, but by no means the least (and maybe the most important). I thank to my family, especially to my mother Lena, father Sergey and younger brother Eugene, for the great support I have felt (and hopefully will feel) throughout my life, for inspiring me, making me think or rest, move or stop and look around... for just being there!

Finally, I would like to thank my country, Ukraine, for giving me inspiration... and some trust in people.

P.S. I would also like to thank all those people whom I did not mention here but whose influence also helped me on the way of producing this thesis.

List of Figures

1.1 **Dependence of the lowest LLs' energies on (a) the magnetic field B for $U = 50$ meV, and (b) on the mini-gap parameter U for $B = 10$ T.** Each level is labeled by a pair of quantum numbers (n, ξ). Only positive-energy part of the spectrum is shown. 42

1.2 **Feynman diagrams showing renormalization of the electron-electron interaction** due to (a) the vacuum polarization processes, and (b) the simplest processes involving virtual hopping of one or both of the two interacting electrons from the n-th LL to the n'-th LL. 47

1.3 **The region of the applicability of perturbative analysis for fixed values of $\kappa = 5$ (yellow), 10 (green) and 15 (blue) for the $(1, -1)$ LL.** The size of the region increases with increasing κ. For (a) the typical interaction energy scale is taken to be the zeroth pseudopotential of the screened interaction potential, for (b) — of the bare Coulomb potential. The thick black line shows where the maximum overlap with the Moore-Read Pfaffian state for the bare Coulomb interaction is achieved. 62

1.4 **The region of the applicability of perturbative analysis for fixed values of $\kappa = 2.5$ (brown), 5 (yellow) and 10 (green) for the $(2, -1)$ LL.** The size of the region increases with increasing κ. For (a) the typical interaction energy scale is taken to be the zeroth pseudopotential of the screened interaction potential, for (b) — of the bare Coulomb potential. At $\kappa = 2.5$ in (b) the condition of smallness of level mixing is not satisfied anywhere within the range of external parameters shown. The thick black line shows where the maximum overlap with the Moore-Read Pfaffian state for the bare Coulomb interaction is achieved. 63

1.5 **Color plot of the overlap of the ground state with the Moore-Read Pfaffian for 12 particles as a function of the magnetic field B and the dielectric constant κ.** (a) – for the $(1, -1)$ LL at $U = 50$ meV, (b) – for the $(2, -1)$ LL at $U = 30$ meV. Contours show the lines of constant overlap. The region where perturbative analysis is not applicable according to the type C estimate is hatched. Data is not shown beyond the region where perturbative analysis is applicable according to the type S estimate. 64

2.1 **Scheme of the experimental device**. Contacts *Ground 1* and *Ground 2* are grounded. *Source N* and *Source S* are used to inject some electric current into the system. Measurement of the electric current and its noise is performed at *Voltage probe*. 70

2.2 **Theoretical picture of the experiment**. The injected current I_n "heats" the neutral mode of the upper edge to the temperature T_n. Equilibration processes between the charged and the neutral modes lead to the charged mode temperature $T_n' = T_n$. Both modes at the lower edge have the temperature of the environment: $T_s' = T_s = T_0$. Tunnelling of the quasiparticles at the constriction induces extra noise in the charged mode of the lower edge which is detected at the *Voltage probe*. Injection of the current I_s only changes the chemical potential of the charged mode of the lower edge. 72

2.3 **Excess noise to tunnelling rate ratio as a function of the current I_s.** Shown are experimental points and fits thereof by theoretical curves for different values of the current I_n. The legend shows the I_n value in nA for each curve (plot symbol). Fitting parameters λ and θ are defined independently for each value of I_n. . 87

2.4 **Excess noise to tunnelling rate ratio as a function of the current I_s.** Shown are experimental points and fits thereof by theoretical curves for different values of the current I_n. The legend shows the I_n value in nA for each curve (plot symbol). Fitting parameter λ is defined independently for each value of I_n. Parameter θ is set to $\theta = \theta_{\rm mean} = \sum_i \theta_i/5 = 0.39$. 88

2.5 **Excess temperature of the upper edge $T_n - T_0$ as a function of the current I_n.** (Color online). Comparison of the points obtained from the data in Table 2.3 with the fit of these points by formula (2.48) is shown. 88

2.6 **Excess noise to tunnelling rate ratio for $I_s = 0$ as a function of current I_n.** (Color online). Experimental points are taken from Fig. 2 of [1] for the tunnelling rate $r \approx 0.2$. The theoretical curve is obtained for $\theta = \theta_{mean} = \sum_i \theta_i/5 = 0.39$. The values of λ are given by Eq. (2.48). No fitting procedure is involved. 89

2.7 **Noise to tunnelling rate ratio vs its asymptotic behaviour**. The green curve is the original noise to tunnelling rate ratio at $\lambda = 1$ (2.52) for $Q = 1/3$, $\delta = 1/6$. The cyan curve is the large I_s asymptote (2.51) for the same values of Q and δ. The asymptote almost coincides with the original curve for $|I_s| \geq 3I_0$. 97

2.8 **Tunnelling rate at $\nu = 1/3$. Perturbative answer vs exact answer.** The red curve is the exact tunnelling rate given by Eqs. (2.54), (2.55). The green curve is the lowest order perturbation theory answer for the tunnelling rate, which can be obtained by taking only the first term in the sum in Eq. (2.54). We remind the reader that the system temperature is equal to $T_0 = 0$. 102

2.9 **Noise to tunnelling rate ratio at $\nu = 1/3$. Perturbative answer vs exact answer.** The red curve is the exact NtTRR plotted using the Eqs. (2.54)–(2.60). The green curve is the lowest order perturbation theory answer for the NtTRR, which can be obtained by taking only the first term in the sums in Eqs. (2.54), (2.59). We remind the reader that the system temperature is equal to $T_0 = 0$. 103

2.10 **Noise to tunnelling rate ratio at $\nu = 1/3$. Perturbative answer vs exact answer in the regime of constant tunnelling rate ratio.** The red curve is the exact NtTRR plotted using the Eqs. (2.54)–(2.60) for $\Xi = 0.5|I_s|$. The green curve is the lowest order perturbation theory answer for the NtTRR, which can be obtained by taking only the first term in the sums in Eqs. (2.54), (2.59). We remind the reader that the system temperature is equal to $T_0 = 0$. 105

A.1 **Color plot of the gap between the ground state and the first excited state computed for** 12 **particles as a function of the magnetic field** B **and the dielectric constant** κ**.** (a) – for the $(1,-1)$ LL at $U = 50$ meV, (b) – for the $(2,-1)$ LL at $U = 30$ meV. The region where perturbative analysis is not applicable according to the type C estimate is hatched. Data is not shown beyond the region where perturbative analysis is applicable according to the type S estimate. 119

A.2 **Color plot of the gap between the ground state and the first excited state computed for** 12 **particles as a function of the magnetic field** B **and the dielectric constant** κ**.** (a) – for the $(1,-1)$ LL at $U = 50$ meV, (b) – for the $(2,-1)$ LL at $U = 30$ meV. The region where perturbative analysis is not applicable according to the type C estimate is hatched. Data is not shown beyond the region where perturbative analysis is applicable according to the type S estimate. 120

A.3 **Dependence of the gap between the ground state and the first excited state computed for** 12 **particles at the** $(1,-1)$ **LL for** $U = 50$ **meV and** $\kappa = 25$ **as a function of the magnetic field** B**.** (a) – in K, (b) – in $e^2/(\kappa\ell)$ units. Only the part where perturbative analysis is applicable is shown. 120

A.4 **Dependence of the gap between the ground state and the first excited state computed for** 12 **particles at the** $(1,-1)$ **LL for** $U = 50$ **meV and** $B = 6.5$ T **as a function of the dielectric constant** κ**.** (a) – in K, (b) – in $e^2/(\kappa\ell)$ units. Only the part where perturbative analysis is applicable is shown. 121

A.5 **Dependence of the gap between the ground state and the first excited state computed for** 12 **particles at the** $(2,-1)$ **LL for** $U = 30$ **meV and** $\kappa = 6$ **(green dotdashed),** 12.5 **(blue dashed), and** 25 **(black solid line) as a function of the magnetic field** B**.** (a) – in K, (b) – in $e^2/(\kappa\ell)$ units. Only the part where perturbative analysis is applicable is shown. 121

A.6 **Dependence of the gap between the ground state and the first excited state computed for** 12 **particles at the** $(2,-1)$ **LL for** $U = 30$ **meV and** $B = 8$ T **as a function of the dielectric constant** κ**.** (a) – in K, (b) – in $e^2/(\kappa\ell)$ units. Only the part where perturbative analysis is applicable is shown. 121

A.7 **Dependence of the overlap with the Pfaffian and gap to the first excited state on the number of particles** N **(**$N = 8, 10, 12, 14$**).** Solid black line is for the non-relativistic $n = 1$ LL. Dashed black line is for the $(1,-1)$ LL at $U = 50$ meV, $\kappa = 25$ and $B = 6.5$ T. Dot-dashed lines are for the $(2,-1)$ LL at $U = 30$ meV, $\kappa = 25$ and $B = 8$ T (black), $\kappa = 12.5$ and $B = 8$ T (blue), $\kappa = 6$ and $B = 6$ T (green). The gap is presented in units of typical Coulomb energy $e^2/\kappa\ell$. 122

A.8 **Dependence of the overlap with the Pfaffian and gap to the first excited state on the number of particles** N **(**$N = 8, 10, 12, 14$**) for the** $(1,-1)$ **LL at** $U = 50$ **meV,** $\kappa = 25$**.** Shown are the dependences for $B = 6.5$ T (dashed black line), $B = 5$ T (dashed grey line), $B = 10$ T (dashed brown line), and $B = 15$ T (dashed purple line). 122

A.9 **Dependence of the overlap with the Pfaffian and gap to the first excited state on the number of particles N ($N = 8, 10, 12, 14$) for the $(2, -1)$ LL at $U = 30$ meV, $\kappa = 25$.** Shown are the dependences for $B = 8$ T (dot-dashed black line), $B = 6$ T (dot-dashed grey line), $B = 10$ T (dot-dashed brown line), and $B = 15$ T (dot-dashed purple line). 123

A.10 **Dependence of the overlap with the Pfaffian and gap to the first excited state on the number of particles N ($N = 8, 10, 12, 14$) for the $(2, -1)$ LL at $U = 30$ meV, $\kappa = 12.5$.** Shown are the dependences for $B = 8$ T (dot-dashed blue line), $B = 6$ T (dot-dashed grey line), $B = 10$ T (dot-dashed brown line), and $B = 15$ T (dot-dashed purple line). 123

A.11 **Dependence of the overlap with the Pfaffian and gap to the first excited state on the number of particles N ($N = 8, 10, 12, 14$) for the $(2, -1)$ LL at $U = 30$ meV, $\kappa = 6$.** Shown are the dependences for $B = 6$ T (dot-dashed green line), $B = 5$ T (dot-dashed grey line), $B = 8$ T (dot-dashed brown line), and $B = 15$ T (dot-dashed purple line). 123

A.12 **Color plot of the overlap of the ground state with the Moore-Read Pfaffian for 12 particles as a function of the magnetic field B and the dielectric constant κ with no virtual hopping corrections taken into account.** (a) – for the $(1, -1)$ LL at $U = 50$ meV, (b) – for the $(2, -1)$ LL at $U = 30$ meV. Contours show the lines of constant overlap. The region where perturbative analysis is not applicable according to the type C estimate is hatched. Data is not shown beyond the region where perturbative analysis is applicable according to the type S estimate. 124

List of abbreviations and conventions

$\{x\}$ — fractional part of number x. For example, $\{2.7\} = 0.7$.

$[A, B]$ — commutator of A and B: $[A, B] = AB - BA$.

$\{A, B\}$ — commutator of A and B: $\{A, B\} = AB + BA$.

δ_{ij} — Kronecker delta: $\delta_{ij} = 1$ for $i = j$, $\delta_{ij} = 0$ for $i \neq j$.

$\mathrm{sgn}(x)$ — sign of the number x: $\mathrm{sgn}(x > 0) = 1$, $\mathrm{sgn}(x < 0) = -1$, $\mathrm{sgn}(0) = 0$.

$\mathbb{N}$ — the set of natural numbers (1, 2, 3, ...).

$\mathbb{R}$ — the set of real numbers.

$\mathbb{R}_+$ — the set of non-negative real numbers.

$\mathbb{Z}$ — the set of integer numbers.

$\mathbb{Z}_+$ — the set of non-negative integer numbers.

2DEG — two-dimensional electron gas.

BLG — bilayer graphene.

CLL — chiral Luttinger liquid.

FQH — fractional quantum Hall.

FQHE — fractional quantum Hall effect.

h-BN — hexagonal Boron nitride.

IQHE — integer quantum Hall effect.

LL — Landau level.

NtTRR — noise to tunnelling rate ratio. For tunnelling experiments in FQHE, NtTRR is the ratio of the excess noise of the electric current flowing along a FQHE

edge to the electric current tunnelling rate.

Paragraph — part of the text numbered as w.x.y.z (e.g. 2.1.4.2).

QH — quantum Hall.

QHE — quantum Hall effect.

QPC — quantum point contact.

RPA — random phase approximation.

Section — part of the text numbered as x.y (e.g. 2.1).

SLLA — single Landau level approximation.

Subsection — part of the text numbered as x.y.z (e.g. 2.1.3).

TPQC — topologically protected quantum computations.

Type C estimate — estimate of smallness of Landau level mixing so that the typical electron-electron interaction energy scale is smaller than the distance between two Landau levels, with typical interaction energy scale calculated with the help of the bare Coulomb potential.

Type S estimate — estimate of smallness of Landau level mixing so that the typical electron-electron interaction energy scale is smaller than the distance between two Landau levels, with typical interaction energy scale calculated with the help of the screened interaction potential.

Introduction

The quantum Hall effect (QHE), observed in two-dimensional electron systems subjected to a strong perpendicular magnetic field, is a quantum version of classical Hall effect with Hall conductivity taking quantized values of $\sigma = \nu\ e^2/h$ [2, 3] (ν is called "filling factor"). The history of the QHE started with the integer QHE (IQHE) for which ν takes on integer values. Except for the transitions between the plateaux of constant Hall conductivity, the IQHE is believed to be pretty well understood in terms of the theory of non-interacting electrons in disordered samples. It also has a practical application: the currently used standard for electrical resistance is based on the IQHE [2].

Quite different is the situation with the fractional QHE (FQHE), in which ν takes on fractional values. With interactions between the electrons playing a crucial role [3], the FQHE exhibits collective behaviour of the electrons with strong correlations between them. Thus, the FQHE cannot be analyzed in terms of weakly interacting electron-like quasiparticles, making it extremely hard for theoretical study. However, not only the challenge of theoretical investigation made it one of the most intensively studied areas in condensed matter physics during the last 30 years.

Some FQHE states have been predicted to support quasiparticle excitations with non-abelian statistics, which may allow for topologically protected quantum computations (TPQC) [4]. I.e., with the help of some FQHE states it is, in principle, possible to create a quantum computer intrinsically protected from (or rather, stable against) decoherence. The challenges of building such a quantum computer

based on a particular FQHE state require significant theoretical and experimental effort, but it turns out that getting a specific FQHE state to work with poses an equally hard task.

For a given filling factor there are usually several likely candidate states, one of which gets realized in the system depending on the specific details of the system and the experimental conditions (such as the magnetic field strength). Not all of the candidate states are expected to allow for TPQC. Thus, it is important to be able to get a specific state in a controlled reproducible way. This problem can be approached in two main ways: one can either study theoretically conditions which make a particular state favourable and try to implement these conditions experimentally; or one can find theoretically the measurements allowing to discriminate between the states and then experimentally find the system that supports a specific state.

Both ways are explored in the present work.

The first chapter expounds a microscopic study of the possibility to realize the so-called Pfaffian (or Moore-Read) FQHE state [5] in bilayer graphene. Bilayer graphene is a novel material consisting of two sheets of graphene. It turns out that this material allows for unprecedented tunability of the parameters important for FQHE by means of external electric and magnetic fields. It was first proposed to use this property to tune the system into the regime which favours the Pfaffian state in Ref. [6]. However, it turns out that the effects of Landau level mixing, vacuum polarization etc., not considered in Ref. [6], are extremely important in this system. The analysis of such effects is performed in order to figure out the conditions under which theoretical predictions are reliable. Under appropriate conditions the possibility to realize the Pfaffian state is investigated. The methodology presented in the chapter can be readily applied to study the possibility to realize any other FQHE state in bilayer graphene given the state's trial wave function.

The second chapter focuses on characterization of FQHE states with the help of electric current noise measurements. Namely, measurements of the noise of the

current tunnelling between two edges of a FQHE state through a narrow constriction. It is a well-known result that in the weak-backscattering limit such a measurement gives information about the electric charge of the quasiparticle responsible for the tunnelling (see, e.g., Refs. [7, 8, 9]). By presenting theoretical analysis of the data of the experiment of Ref. [1] this chapter shows that much more information can be inferred from such measurements, including some information about the interaction of an Ohmic contact with an FQHE edge. More importantly in the context of the problem outlined above, we show that information about the edge physics such as the tunnelling quasiparticle scaling dimension can, in principle, be obtained from such measurements.

It is worth mentioning that different methodologies are used in the two chapters. As the problem attacked in the first chapter concerns comparison of the exact system state and a model state, the microscopic quantum-mechanical methodology based on many-particle wave functions is used. In this methodology FQHE states are primarily characterized by their trial ground state wave function. In the second chapter transport measurements are dealt with, and it is more convenient to use the methodology based on the low-energy effective field theories in this case. In this methodology a FQHE state is characterized by its low-energy edge theory. There are some widely used hypotheses about the connection between the two approaches (namely, on how to relate a ground state trial wave function with the corresponding edge theory). However, the connection between the two approaches is not considered in the present work.

The results of the present work concerning possibility to observe specific FQHE states and ways to characterize them by no means fully resolve the problem of getting in a controlled reproducible way a FQHE state which allows for TPQC. However, they may constitute an important piece in the way of finding an answer to the problem.

Chapter 1

Ways to observe specific fractional quantum Hall states in bilayer graphene

In this chapter we develop a methodology which allows to study the possibility to realize specific FQHE states in bilayer graphene.

It is well-known that the electron-electron interaction is crucial for the FQHE [3]. Depending on the exact form of the interaction potential one can get at the same filling factor different FQHE states or even no FQHE at all. Bilayer graphene is a novel material that allows adjusting properties of the electron-electron interaction with the help of external parameters: perpendicular to the material sheet magnetic and electric fields. Using this property to tune the system into the regime which favours a specific FQHE state was first proposed in Ref. [6].

However, there is a number of effects that make theoretical studying of such possibilities more complicated. These complications arise due to significance of the interaction between different Landau levels in bilayer graphene. A methodology allowing to deal with the complications is developed and expounded in the present chapter.

The first section reminds the reader the methodology for studying FQHE in

conventional ("non-relativistic") systems basing on the exact numerical diagonalization of the system Hamiltonian in the single Landau level approximation.

In the second section we expound a formalism which allows to use the same methodology in bilayer graphene.

In the third section we discuss the effects of interaction of different Landau levels and incorporation of them into the single-Landau-level-based methodology introduced earlier.

Finally, in the fourth section we apply our methodology that takes into account the deviations from the single Landau level approximation to study the possibility to realize the Pfaffian [5] state in bilayer graphene.

1.1 Numerical diagonalization approach to the quantum Hall effect in non-relativistic systems

1.1.1 Problem of a free non-relativistic electron in magnetic field

In this section we recall how Landau levels (LLs) emerge in two-dimensional non-relativistic systems in magnetic field, we also introduce some notation that will be used in the following sections.

The single electron Hamiltonian in the uniform magnetic field, perpendicular to the plane of the system, is

$$H_{1-part} = \frac{\boldsymbol{\pi}^2}{2m^*} - \frac{e\hbar}{m_e c} B S_z, \tag{1.1}$$

where $\boldsymbol{\pi} = (\pi_x, \pi_y)$ (since the system is two-dimensional), $\pi_i = p_i + eA_i/c$, $p_i = -i\hbar\partial_i$, e is the elementary charge, $\mathbf{A} = [\mathbf{B} \times \mathbf{r}]/2$ is the vector potential of the uniform magnetic field $\mathbf{B} = -B\mathbf{e_z}$, S_z is the z-component of the electron spin, m_e

is the free electron mass and m^* is the effective mass of the electron.

We introduce the magnetic length l, the cyclotron frequency ω_c, and the complex coordinate w in the plane:

$$l = \sqrt{\frac{\hbar c}{eB}}\ ,\ \omega_c = \frac{eB}{m^* c}\ ,\ w = \frac{x+iy}{l},\ \bar{w} = \frac{x-iy}{l}. \tag{1.2}$$

We also introduce operators $\hat{a}, \hat{a}^\dagger, \hat{b}, \hat{b}^\dagger$:

$$\hat{a} = \sqrt{2}(\bar{\partial} + \frac{w}{4}), \hat{a}^\dagger = \sqrt{2}(-\partial + \frac{\bar{w}}{4}), \tag{1.3}$$

$$\hat{b} = \sqrt{2}(\partial + \frac{\bar{w}}{4}), \hat{b}^\dagger = \sqrt{2}(-\bar{\partial} + \frac{w}{4}). \tag{1.4}$$

where ∂ and $\bar{\partial}$ denote $\partial/\partial w$ and $\partial/\partial \bar{w}$ respectively. All commutation relations between these four operators are trivial except for the following:

$$\left[\hat{a}, \hat{a}^\dagger\right] = \left[\hat{b}, \hat{b}^\dagger\right] = 1. \tag{1.5}$$

We can then rewrite the Hamiltonian in the form

$$H_{1-\text{part}} = \hbar\omega_c(\hat{a}^\dagger\hat{a} + \frac{1}{2}) - \frac{e\hbar}{m_e c}BS_z. \tag{1.6}$$

The operators $\hat{a}, \hat{a}^\dagger$ are similar to the ladder operators in the problem of the harmonic oscillator, thus the system's spectrum consists of Landau levels with energies $E_n = \hbar\omega_c(n + 1/2) - e\hbar BS_z/(m_e c)$, $n \in \mathbb{Z}_+$, $S_z = \pm 1/2$. Operators $\hat{b}, \hat{b}^\dagger$ commute with the Hamiltonian, thus they transform one state into another state within the same Landau level.

Let us consider the operator of the z-projection of the angular momentum:

$$\hat{L} = \hat{L}_z/\hbar = \left[\mathbf{r} \times \mathbf{p}\right]_z/\hbar = z\partial - \bar{z}\bar{\partial} = \hat{b}^\dagger\hat{b} - \hat{a}^\dagger\hat{a}. \tag{1.7}$$

It is easy to see that

$$\left[\hat{L},\hat{a}\right]=\hat{a},\left[\hat{L},\hat{a}^{\dagger}\right]=-\hat{a}^{\dagger},\left[\hat{L},\hat{b}\right]=-\hat{b},\left[\hat{L},\hat{b}^{\dagger}\right]=\hat{b}^{\dagger} \tag{1.8}$$

$$\Rightarrow\left[\hat{L},H_{1-\mathrm{part}}\right]=0. \tag{1.9}$$

Thus the eigenstates of the Hamiltonian (1.1) can be labeled by three quantum numbers: Landau level number $n\in\mathbb{Z}_{+}$, z-projection of the angular momentum $m\in(\mathbb{Z}_{+}-n)$ and the electron spin projection $S_z=\pm1/2$

$$|n,m,S_z\rangle=\psi_{nm}(w)\otimes|S_z\rangle. \tag{1.10}$$

The orbital wave function ψ_{nm} can be expressed as

$$\psi_{nm}(w) = \frac{1}{\sqrt{n!(n+m)!}}(\hat{b}^{\dagger})^{n+m}(\hat{a}^{\dagger})^{n}\psi_{00}(w), \tag{1.11}$$

$$\psi_{00}(w) = \frac{1}{\sqrt{2\pi l^2}}e^{-\frac{|w|^2}{4}},\ \hat{a}\psi_{00}=\hat{b}\psi_{00}=0. \tag{1.12}$$

Note that the wave functions (1.11) are polynomials of complex coordinates $w,\bar{w}$, multiplied by the exponential $\exp\left(-|w|^2/4\right)$ which is the same for all of the states. In particular,

$$\psi_{n=0,m}(w)=\frac{1}{\sqrt{2^{m+1}\pi l^2}}w^{m}e^{-\frac{|w|^2}{4}}. \tag{1.13}$$

So, the system's energy levels are Landau levels with energies $E_{n,S_z}=\hbar\omega_c(n+1/2)-e\hbar BS_z/(m_ec)$, with eigenstates in a LL labeled by the angular momentum projection $m\geq-n$.

In a finite sample there is only a finite number of states available to an electron in a Landau level. One can estimate their number using the fact that the states (1.11)-(1.12) are spatially localized: the number of states in a Landau level of a finite round sample is approximately equal to the number of states (1.11)-(1.12) that are localized mainly in the area of the sample. Thus, one can introduce the

filling factor ν:

$$\nu = 2\pi l^2 n_e = N_e/N_{\text{orb}}, \tag{1.14}$$

where n_e is the density of electrons, N_e is the total number of electrons in the system and N_{orb} is the number of orbits in a LL in the sample.

Typically in GaAs heterostructures $m^* \approx 0.07m_e$, thus LLs with the same number but different spin projections form quasidegenerate doublets. For a typical fractional quantum Hall (FQH) experiment in such systems the typical Coulomb energy scale $e^2/(\kappa l)$ (κ is the dielectric constant, in GaAs $\kappa \approx 13$) is about of the same order as the cyclotron frequency $\hbar\omega_c$. For $B \gtrsim 5$T the interaction energy scale is less than the inter-doublet distance, thus for greater fields it is a not too bad approximation to consider only electrons which are in the two quasidegenerate LLs; all of the other levels — either not filled yet or fully filled already — differ in energy too much, so the interaction between electrons cannot throw electrons to the other Landau levels effectively. The corrections to this picture can be taken into account by means of perturbation theory but for the simplicity of exposition, in this section we neglect them.

The orbital wave function of the electrons in a fully polarized state is totally antisymmetric. Antisymmetric orbital wave function means that it is unlikely to have two electrons close to each other. This reduces their repulsion energy (if the interaction potential decreases monotonically which is typically the case). Another reason for the electrons to form spin-polarized states is the Zeeman splitting (even though it is small). Thus, usually electrons form spin-polarized states which are fully in one of the quasidegenerate Landau levels.

In the remaining part of this section we only consider one Landau level, neglecting the influence of another Landau levels. This approximation is called the single Landau level approximation (SLLA). We also assume that the state is spin-polarized, therefore we suppress spin variables.

1.1.2 Interaction of two electrons in a non-relativistic Landau level

We begin the discussion of the many-body problem with the two-particle case. For interaction potentials which depend only on the distance between the electrons this problem can be solved exactly. This solution gives an opportunity to introduce some important notions.

The two-electron Hamiltonian can be written as follows:

$$\hat{H}_{2-\text{part}} = \hat{H}_{\text{free}} + V(r), \tag{1.15}$$

$$\hat{H}_{\text{free}} = \hat{H}_{1-\text{part},1} + \hat{H}_{1-\text{part},2}, \tag{1.16}$$

where $r = |\vec{r_1} - \vec{r_2}| = l|w_1 - w_2|$, $V(r)$ is the interaction potential, e.g., the Coulomb potential.

Since we are working in the SLLA approximation, the single-particle part of the Hamiltonian is proportional to the identity operator and can be excluded from the consideration. Thus to diagonalize the Hamiltonian we only need to diagonalize the interaction potential operator $V(r)$ in the Hilbert space spanned by vectors

$$|m_1, m_2\rangle = \frac{1}{\sqrt{2}}(|m_1\rangle \otimes |m_2\rangle - |m_2\rangle \otimes |m_1\rangle), \tag{1.17}$$

with the angular momenta of the two electrons, m_1 and m_2, taking all the possible values in the LL considered.

We introduce z-projections of the relative angular momentum and the angular momentum of the center of mass:

$$\hat{L}_{\text{rel}} = \left(\frac{1}{2\hbar}[(\vec{r_1} - \vec{r_2}) \times (\vec{p_1} - \vec{p_2})]\right)_z = \frac{1}{2}\left(\hat{L}_1 + \hat{L}_2 - b_1^\dagger b_2 - b_2^\dagger b_1 + a_1^\dagger a_2 + a_2^\dagger a_1\right), \tag{1.18}$$

$$\hat{L}_{\rm cm} = \left(\frac{1}{2\hbar}[(\vec{r}_1 + \vec{r_2}) \times (\vec{p}_1 + \vec{p}_2)]\right)_z = \frac{1}{2}\left(\hat{L}_1 + \hat{L}_2 + b_1^\dagger b_2 + b_2^\dagger b_1 - a_1^\dagger a_2 - a_2^\dagger a_1\right). \quad (1.19)$$

These operators projected onto a single LL have the following form:

$$\hat{L}^p_{\rm rel} = \frac{1}{2}\left(\hat{L}_1 + \hat{L}_2 - b_1^\dagger b_2 - b_2^\dagger b_1\right), \quad (1.20)$$

$$\hat{L}^p_{\rm cm} = \frac{1}{2}\left(\hat{L}_1 + \hat{L}_2 + b_1^\dagger b_2 + b_2^\dagger b_1\right). \quad (1.21)$$

Raising and lowering operators for this "single-level angular momenta" are $\hat{b}_1^\dagger \mp \hat{b}_2^\dagger$ and $\hat{b}_1 \mp \hat{b}_2$ respectively. With the help of these operators we can represent the eigenstates of the "single-level angular momenta" in the (n, S_z) Landau level as follows:

$$|m, M\rangle = \frac{1}{\sqrt{2^{m+M} m! M!}} (\hat{b}_1^\dagger - \hat{b}_2^\dagger)^m (\hat{b}_1^\dagger + \hat{b}_2^\dagger)^M (\psi_{n,-n})_1 (\psi_{n,-n})_2, \quad (1.22)$$

$$\hat{L}^p_{\rm rel}|m, M\rangle = (m - n)|m, M\rangle, \quad (1.23)$$

$$\hat{L}^p_{\rm cm}|m, M\rangle = (M - n)|m, M\rangle. \quad (1.24)$$

Here $M, m \geq 0$. We will say that $|m, M\rangle$ is a state with the relative angular momentum m and the center of mass angular momentum M. Since every state has to be antisymmetric with respect to the permutation of the electrons, only states with odd m are present in our Hilbert space. The states $|m, M\rangle$ for $m \in 2\mathbb{Z}_+ + 1$ and $M \in \mathbb{Z}_+$ form a complete orthonormal basis.

Commutation relations of the "angular momenta" with the operator $\hat{V} = V(r)$ are

$$\left[\hat{V}, \hat{L}^p_{\rm rel/cm}\right] = 0, \quad (1.25)$$

$$\left[\hat{V}, \hat{b}_1^\dagger + \hat{b}_2^\dagger\right] = 0 \quad , \quad \left[\hat{V}, \hat{b}_1 + \hat{b}_2\right] = 0, \tag{1.26}$$

$$\left[\hat{V}, \hat{b}_1^\dagger - \hat{b}_2^\dagger\right] \neq 0 \quad , \quad \left[\hat{V}, \hat{b}_1 - \hat{b}_2\right] \neq 0. \tag{1.27}$$

Thus the interaction potential operator can be represented in the LL as

$$\hat{V}(r) = \sum_{m,M} |m, M\rangle V_m^{(n,n)} \langle m, M|, \tag{1.28}$$

which solves the two-body problem in the LL.

Matrix elements $V_m^{(n,n)}$ which parametrize the operator are called pseudopotential coefficients (or just pseudopotentials), they were first introduced in [10]. Connection of the pseudopotentials with the interaction potential's matrix elements is obvious since the states $|m, M\rangle$ are orthonormal.

In the following section we shall also need a more general matrix element $V_m^{(n_1,n_2)}$:

$$|n_1, n_2, m, M\rangle = \frac{1}{\sqrt{2^{m+M} m! M!}} (\hat{b}_1^\dagger - \hat{b}_2^\dagger)^m (\hat{b}_1^\dagger + \hat{b}_2^\dagger)^M (\psi_{n_1,-n_1})_1 (\psi_{n_2,-n_2})_2, \tag{1.29}$$

$$V_m^{(n_1,n_2)} = \langle n_1, n_2, m, M|\hat{V}|n_1, n_2, m, M\rangle = \langle n_1, n_2, m, 0|\hat{V}|n_1, n_2, m, 0\rangle. \tag{1.30}$$

It is easy to check that $V_m^{(n_1,n_2)} = V_m^{(n_2,n_1)}$ for the potentials depending on the distance between the electrons.

For computations, it is often more convenient to express $V_m^{(n_1,n_2)}$ in terms of the potential's Fourier transform $\tilde{V}(q)$ [3]:

$$\tilde{V}(q) = \frac{1}{l^2} \int d^2 r V(r) e^{-i\vec{q}\vec{r}/l} = \frac{2\pi}{l^2} \int_0^\infty V(r) J_0(qr/l) r dr = 2\pi \int_0^\infty V(lx) J_0(qx) x dx, \tag{1.31}$$

$$V_m^{(n_1,n_2)} = \int_0^\infty \tilde{V}(q) L_m(q^2) L_{n_1}(q^2/2) L_{n_2}(q^2/2) e^{-q^2} \frac{q dq}{2\pi}, \tag{1.32}$$

where J_0 is the zeroth Bessel function of the first kind, L_k are the Laguerre polynomials, l is the magnetic length. Derivation of this formula is presented in the appendix A.1.

Thus, the electrostatic interaction between the electrons located in one Landau level can be expressed through a countable set of pseudopotentials $V_m^{(n,n)}$, where n is the LL number, and $m \in 2\mathbb{Z}_+ + 1$ is the "relative angular momentum" of the two interacting electrons.

1.1.3 Many-particle problem

Here we discuss the problem of many electrons in a Landau level and the approach of numerical diagonalization.

Since we know how to express the action of the electron-electron interaction in the Hilbert space of two electrons in a Landau level, we can, in principle, express the many-particle system's Hamiltonian through the pseudopotentials. Then, the task to do is to diagonalize it. Typically this cannot be done theoretically. What remains is to do this numerically. The problem is that the Hamiltonian is an infinite matrix (since there are an infinite number of orbits in a Landau level). However, any real system is finite: boundaries of the sample do not allow electrons to leave it. This can (and should!) be described by adding an external confining potential. For example, one can consider a system of electrons on a disk, with the confining potential

$$V_{\text{ext}}(r) = \begin{cases} 0, r < r_0 \\ +\infty, r > r_0 \end{cases}. \tag{1.33}$$

However, such a choice changes single-level states in a Landau level (especially those close to the boundary). At the same time we expect that for a large number of electrons the properties of the system do not depend significantly on the exact form of the bounding potential. Since in any Landau level each of the states ψ_{nm} is localized in a circle with width of the order of the magnetic length l and radius

$r \approx l\sqrt{2m}$ (for $m \gg 1$[1]), it should be a good approximation to consider a system with the same single-electron states as in the infinite system, but only orbits with $m \leq m_0$ available to the electrons. We shall refer such a system as a "system on disk".

Thus, the Hamiltonian of a system on disk is a finite matrix that can be expressed in terms of pseudopotentials introduced in the previous subsection and diagonalized numerically. This enables us to find the spectrum and the eigenstates of the system. A typical thing to do then is to compare the numerically found ground state (and, possibly, the excited states) with some trial wave function to check whether the real state is close to the proposed trial state.

There is some peculiarity in choosing the number of electrons and orbits in the system. If one studies the filling factor ν, then by definition in the thermodynamic limit number of electrons N_e in the LL considered and the number of orbits available to them N_{orb} are related by $N_e/N_{\text{orb}} \approx \{\nu\}$, where $\{\nu\}$ denotes the fractional part of the filling factor. On the contrary, trial wave functions (as it can be seen from examples below) fix the relation between the two numbers not approximately but exactly:

$$N_{\text{orb}} = N_e/\{\nu\} - S + 1. \tag{1.34}$$

Number S is called "shift" and can be different for different trial wave functions.[2]. Of course, we expect the properties of the system in the thermodynamic limit to be independent of the precise ratio between the number of electrons and the number of orbits; but in order to compare an exact state with a trial wave function, the numbers of orbits and electrons in the two should coincide.

Often they consider a system on sphere [10] instead of the system on disk (two-dimensional finite sphere with the uniform magnetic field transverse to the sphere is considered instead of plane). System on sphere is finite from the very beginning

[1] In fact, this is a good approximation already for $m \geq n$, where m is the angular momentum quantum number and n is the Landau level number.

[2] The summand $+1$ is for the number of the last available orbit in the zeroth LL m_{max} to be expressed as $m_{\text{max}} = N_e/\{\nu\} - S$. This is the commonly used definition of the shift.

so one does not need to introduce a boundary. The wave functions of the single particle states and pseudopotentials are expressed in a somewhat different way (so the matrix of the Hamiltonian is expressed somewhat differently via spherical pseudopotentials). However, for large enough systems the results on sphere should coincide with the results on disk (since the curvature of the sphere plays little role then). That's why they often use planar pseudopotentials for diagonalization on sphere (see e.g. [11])[3]. In this work we do a similar thing: we use diagonalization on sphere with planar pseudopotentials.

So, the procedure of numerical finding the system's ground state and its comparison with trial state is as follows: choose the trial state with which to compare; choose the number of electrons and orbits in such a way that it corresponds to the trial state; find pseudopotentials; calculate the system's Hamiltonian and diagonalize it; calculate the scalar product of the numerically found ground state with the trial state (the closer it is to 1 the more similar the states are).

Usually the numerical diagonalization can be performed only for relatively small numbers of electrons (around 10 to 20) in most cases. This is far from the thermodynamic limit. However, the experimental success of Laughlin's wave function (or rather predictions based on it) together with the numerical success of Laughlin's wave function gives hope that the results of numerical diagonalization for small numbers of electrons can be relied on, at least to some extent.

Before proceeding to application of this method to bilayer graphene, we show several examples of trial wave functions in the next paragraph.

1.1.3.1 Examples of trial wave functions

Now we are going to consider several examples of trial wave functions in order to understand how they look and how to interpret them (for the purposes of numerical diagonalization).

[3]There is a correspondence between trial states which are proposed for the sphere and for the plane, so a result of the diagonalization on sphere can be compared with a trial state just in the same way as a result of the diagonlization on disk.

The simplest example is a trial wave function for the fully filled zeroth LL. Let N be the number of electrons which occupy first N orbits of the $n = 0$ level. Due to the Pauli principle the only possible state is the Slater determinant of all the occupied single-particle orbits:

$$\psi(w_1, ..., w_N) = \det_{1\le i\le N, 0\le m\le N-1} \psi_{n=0,m}(w_i) \propto$$

$$\propto \begin{vmatrix} 1 & w_1 & \dots & w_1^{N-1} \\ 1 & w_2 & \dots & w_2^{N-1} \\ \vdots & \vdots & \ddots & \vdots \\ 1 & w_N & \dots & w_N^{N-1} \end{vmatrix} \times e^{-\sum_i |w_i|^2/4}, \quad (1.35)$$

where we used the explicit form of the single-particle wave functions in the zeroth LL (1.13). The determinant in the r.h.s. is the well known Vandermonde determinant. Therefore, we can write down the answer for the wave function, which, up to the normalization constant $\mathcal{N}$, looks as follows:

$$\psi(w_1, ..., w_N) = \mathcal{N} e^{-\sum_i |w_i|^2/4} \prod_{1\le i<j\le N} (w_i - w_j). \quad (1.36)$$

This example illustrates the fact that any wave function of electrons in the zeroth LL can be expressed as a polynomial of coordinates w_i — no $\bar{w}_i$ — times the exponent which is determined only by the number of electrons. In what follows in this paragraph instead of the wave function $\psi(w_1, ..., w_N)$ we will write out the polynomial $P(w_1, ..., w_N)$. For example, for the fully filled zeroth LL

$$P(w_1, ..., w_N) = \prod_{1\le i<j\le N} (w_i - w_j). \quad (1.37)$$

If electrons don't fill the whole LL they will try to keep as big a distance from each other as possible (because of the Coulomb repulsion). Starting from this argument, R. Laughlin proposed his famous trial wave function for the filling

factor $\nu = 1/3$ [12]:

$$P(w_1, ..., w_N) = \prod_{1 \le i < j \le N} (w_i - w_j)^3. \tag{1.38}$$

It is easy to convince oneself that it indeed corresponds to $\nu = 1/3$ by counting the number of orbits used by the electrons in this wave function. It has shift $S = 3$ (in contrast to the full filling, where $S = 1$). This trial wave function has been extremely successful, the key point is that power 3 significantly reduces the probability of finding two electrons close to each other.

This wave function has been generalized for the fillings $\nu = 1/m$:

$$P(w_1, ..., w_N) = \prod_{1 \le i < j \le N} (w_i - w_j)^m. \tag{1.39}$$

However, since the wave function of the electrons should be antisymmetric, m has to be odd. So, this wave function can be used only for fillings with odd denominators.

There had not been any need in description of even denominators until the $\nu = 5/2$ FQHE was observed. Moore and Read in 1991 proposed their trial wave function for a half-filled LL[4] [5]. The wave function, if written for the zeroth LL, looks like

$$P(w_1, ..., w_N) = \mathrm{Pfaff}\left(\frac{1}{w_i - w_j}\right) \prod_{1 \le i < j \le N} (w_i - w_j)^2 = \mathrm{AntiSymm}\left(\frac{1}{w_1 - w_2}\frac{1}{w_3 - w_4} \dots \frac{1}{w_{N-1} - w_N}\right) \times \prod_{1 \le i < j \le N} (w_i - w_j)^2. \tag{1.40}$$

AntiSymm $(\dots)$ denotes the expression in brackets antisymmetrized in electrons permutations. The antisymmetrized combination which is present here is called "Pfaffian" in honour of German mathematician Johann Friedrich Pfaff. After this

[4] As it has been mentioned already, it is assumed that only the partially filled level is important.

expression the Moore-Read wave function is also often called the Pfaffian. Filling factor associated with this wave function is $\nu = 1/2$, and the shift is $S = 3$; the wave function is evidently antisymmetric.

One can write wave functions for higher Landau levels in a similar explicit fashion, but, in fact, for numerical comparison one only needs the coefficients of the state vector expanded in the basis of orbital occupation numbers. For a zeroth LL wave function those coefficients can be obtained from the polynomial representing it by expanding the polynomial into a linear combination of monomials — each w_i^k up to the normalization factor corresponds to an electron occupying the state $\psi_{n=0,m=k}$. One can also interpret the zeroth LL trial wave function as a wave function for a higher LL. For that one should replace $\psi_{0,k} \to \psi_{n,k-n}$ in the very end of the procedure of getting the coefficients. Therefore, polynomials of electrons' coordinates w_i are used for representing trial wave functions for both zeroth LL and the higher LLs.

Absolutely similarly a polynomial can be interpreted as a trial state for any system where states in a LL are labeled by an integer number limited from below and corresponding to the angular momentum.

Thus, all the trial states, including the Pfaffian, can be used for higher LLs. In the $n = 1$ LL the Pfaffian state's overlap with the numerically found ground state for 12 electrons is close to 0.7[5]. This is not that impressive as Laughlin's $98 - 99\%$, but not that bad for the Hilbert space of dimension over 16 thousand (two random vectors would have an overlap near 1/16000 in such space). The FQHE with $\nu = 5/2$ (which corresponds to a half-filled $n = 1$ LL) is observed in GaAs heterostructures. However, it remains unclear up to now whether the state corresponds to the Moore-Read state or not — that is, among other reasons, due to the experimental fragility of the state, which makes it hard to work with.

[5]By overlap we mean scalar product's absolute value squared.

1.1.4 Summary of the section

In this section we review the basis of numerical diagonalization methodology for non-relativistic FQHE systems: introduce Landau levels, briefly discuss the applicability of the SLLA to the GaAs heterostructures, introduce pseudopotentials, and discuss peculiarities of numerical diagonalization in the non-relativistic systems. We also discuss several examples of trial wave functions, including the Pfaffian, and their representation in the form of holomorphic polynomials of complex coordinates.

1.2 Numerical diagonalization approach to the quantum Hall effect in bilayer graphene (single Landau level approximation)

In this section we discuss peculiarities of numerical diagonalization method in bilayer graphene in the SLLA. Landau levels in bilayer graphene are introduced, formulae for the pseudopotentials are found.

1.2.1 Bilayer graphene. Hamiltonian of a free electron in bilayer graphene

Graphene is a one-atom thick layer of graphite, or in other words — two dimensional hexagonal lattice with carbon atoms in lattice points. Bilayer graphene (BLG) is just two layers of graphene (two graphene sheets) with certain matching of lattice points. For a detailed review on graphene and bilayer graphene see Ref. [13]. We are going to recall only the facts necessary for the following consideration.

The Fermi surface of graphene comprises just two points, in vicinity of which the low-energy excitations are situated. One can usually neglect jumping of elec-

trons between the two vicinities (valleys)[6]. Therefore, to describe this system we can consider two Hamiltonians each of which describes dynamics of one valley.

In bilayer graphene the low-energy excitations are also situated near the same points in the momentum space. The low-energy bilayer graphene Hamiltonian (without external magnetic field) can be written then as [13, 14][7]

$$H_{1-part}^{BLG} = \xi \begin{pmatrix} -U & 0 & 0 & v\pi^\dagger \\ 0 & U & v\pi & 0 \\ 0 & v\pi^\dagger & U & \xi\gamma_1 \\ v\pi & 0 & \xi\gamma_1 & -U \end{pmatrix}, \tag{1.41}$$

where $\xi = \pm 1$ corresponds to the two valleys K ($\xi = +1$) and K' ($\xi = -1$), $\pi = p_x + ip_y$ is the complex momentum; the spectrum has a mini-gap $2U$, which can be tuned by the external electric field perpendicular to the bilayer graphene sheet[8]. We will call U the "mini-gap parameter". The Fermi velocity is taken to be $v \approx 10^6$ m/s, and the interlayer hopping constant is taken to be $\gamma_1 \approx 0.35$ eV [13].

In the absence of the external electric field (when $U = 0$) the low-energy spectrum has quadratic form $E = \pm|\pi|^2/(2m^*)$, where the effective mass $m^* = \gamma_1/(2v^2) \approx 0.03m_e$ [14].

[6]This is due to the fact that jumping needs transfer of a quite big momentum (of the order of h/a, where a is the lattice constant and has value around $0,25$ nm). For example, matrix element of the Coulomb potential decreases like $1/q$ as the transferred momentum q grows. Therefore, jumping between the valleys is suppressed with controlling parameter being the ratio of the lattice constant a to the typical spatial scale one is interested in (in our case this is the magnetic length l, typical values of the magnetic length are around $l = 10$ nm).

[7]The Hamiltonian is written in the basis corresponding to the atomic sites A, $\tilde{B}$, $\tilde{A}$, B in the K valley and $\tilde{B}$, A, B, $\tilde{A}$ in the K' valley. The sites A and B are situated in the bottom graphene layer, while $\tilde{A}$ and $\tilde{B}$ are in the top layer. Our convention is the same as the one used in Refs. [13, 14] except for a redefinition of U.

[8]One can think that the electrostatic potential of one layer is U, while the other layer's potential is $-U$.

1.2.2 Problem of a free electron in magnetic field (bilayer graphene)

The Hamiltonian of an electron in bilayer graphene in the perpendicular magnetic field is obtained by extending the derivatives and taking the spin energy into account:

$$H_{1-part}^{BLG} = \xi \begin{pmatrix} -U & 0 & 0 & v\pi^\dagger \\ 0 & U & v\pi & 0 \\ 0 & v\pi^\dagger & U & \xi\gamma_1 \\ v\pi & 0 & \xi\gamma_1 & -U \end{pmatrix} - \frac{e\hbar}{m_e c} B S_z, \tag{1.42}$$

where $\xi = \pm 1$ is for the two valleys, $\pi = \pi_x + i\pi_y$ (see definition of π_i after formula (1.1)). Without loss of generality we will consider only the case $B, U > 0$.

It is easy to express the complex momenta through the operators (1.3-1.4):

$$\pi = -i\sqrt{2}\hbar l^{-1}\hat{a}, \pi^\dagger = i\sqrt{2}\hbar l^{-1}\hat{a}^\dagger. \tag{1.43}$$

Thus the Hamiltonian can be expressed as

$$H_{1-part}^{BLG} = \xi\hbar\omega_c \begin{pmatrix} -u & 0 & 0 & i\gamma\hat{a}^\dagger \\ 0 & u & -i\gamma\hat{a} & 0 \\ 0 & i\gamma\hat{a}^\dagger & u & \xi\gamma^2 \\ -i\gamma\hat{a} & 0 & \xi\gamma^2 & -u \end{pmatrix} - 2\mu_B B S_z, \tag{1.44}$$

where we introduced $\omega_c = eB/(m^* c) = 2v^2 eB/\gamma_1 c$ (after definition of ref. [14]), $\gamma^2 = \gamma_1/(\hbar\omega_c)$, $u = U/(\hbar\omega_c)$.

It turns out that this Hamiltonian does not commute with the z-projection of the orbital angular momentum $\hat{L}$ defined in Eq. (1.7). We introduce the z-

projection of the "pseudospin angular momentum" $\hat{\Sigma}$:

$$\hat{\Sigma} = \begin{pmatrix} 1 & 0 & 0 & 0 \\ 0 & -1 & 0 & 0 \\ 0 & 0 & 0 & 0 \\ 0 & 0 & 0 & 0 \end{pmatrix}. \tag{1.45}$$

Then the z-projection of the full angular momentum $\hat{J} = \hat{L} + \hat{\Sigma}$ does commute with the Hamiltonian.

Now it is easy to express the general form of the spatial part of the Hamiltonian's (1.44) eigenstates through the non-relativistic wave functions (1.11-1.12):

$$\Psi_{nm} = \begin{pmatrix} A_n \psi_{nm} \\ B_n \psi_{n-2,m+2} \\ C_n \psi_{n-1,m+1} \\ D_n \psi_{n-1,m+1} \end{pmatrix}, \tag{1.46}$$

the sense of the number n is similar to the Landau level number, while m corresponds to the projection of the full angular momentum $j_z = m+1$. The amplitudes A_n, B_n, C_n, D_n do not depend on m.

Acting on this wave function by the Hamiltonian and demanding it to be an eigenfunction we find the equation for the eigenvalues:

$$((u - \xi\varepsilon)^2 - \gamma^2 n)((u + \xi\varepsilon)^2 - \gamma^2(n-1)) = \gamma^4(\varepsilon^2 - u^2) \tag{1.47}$$

where $\varepsilon = (E + 2\mu_B B S_z)/(\hbar\omega_c)$, and E is the energy.

Finding the single particle spectrum for the realistic values of the parameters, we see that the levels split into two groups: the one with $|E| < \gamma_1$ and the one with $|E| \geq \gamma_1$. The Zeeman splitting is negligibly small, just like in the non-relativistic case. The levels with $|E| < \gamma_1$, which we are interested in can be characterized by five quantum numbers: the valley index ξ, the LL number $n \in \mathbb{Z}_+$, the full

angular momentum projection $j_z = m + 1$ with $m \in (\mathbb{Z}_+ - n)$, $s = \pm 1$ (which shows whether the energy is positive or negative) and $S_z = \pm 1/2$. Thus the wave functions (their spatial components) in the n-th LL look like

$$\Psi_{nm}^{\xi s} = \begin{pmatrix} A_n^{\xi s}\psi_{nm} \\ B_n^{\xi s}\psi_{n-2,m+2} \\ C_n^{\xi s}\psi_{n-1,m+1} \\ D_n^{\xi s}\psi_{n-1,m+1} \end{pmatrix}. \tag{1.48}$$

The amplitudes which are present in this formula can be expressed like

$$A_n^{\xi s} = \mathcal{N}, \tag{1.49}$$

$$B_n^{\xi s} = -\frac{\sqrt{n-1}}{u + \xi\varepsilon_n^{\xi s}} \frac{(u - \xi\varepsilon_n^{\xi s})^2 - \gamma^2 n}{\xi\gamma^2\sqrt{n}}\mathcal{N}, \tag{1.50}$$

$$C_n^{\xi s} = -i\frac{(u - \xi\varepsilon_n^{\xi s})^2 - \gamma^2 n}{\xi\gamma^3\sqrt{n}}\mathcal{N}, \tag{1.51}$$

$$D_n^{\xi s} = i\frac{u - \xi\varepsilon_n^{\xi s}}{\gamma\sqrt{n}}\mathcal{N}, \tag{1.52}$$

where $\mathcal{N}$ is a normalization constant. Obviously, they depend on the magnetic field B and the mini-gap parameter U.

Before considering the two particle problem in bilayer graphene, have a look at the single-particle spectrum. Fig. 1.1a shows the dependence of the several lowest Landau levels on the magnetic field for $U = 50$ meV. Only positive part of the spectrum is shown, the negative part can be obtained with the help of electron-hole conjugation ($\varepsilon_n^{\xi,-s} = -\varepsilon_n^{-\xi,s}$). Each positive LL is labeled by a pair of quantum numbers (n, ξ). One can see that for large values of the magnetic field the levels form quasidegenerate doublets which are separated by the energies of the order of $\hbar\omega_c$. Fig. 1.1b shows the dependence of the same LLs' energies on the mini-gap parameter U for the magnetic field $B = 10$ T. Note that for large enough values of U (or for small enough values of B) multiple crossings of Landau levels occur. It is easy to understand that when several LLs are close to each other (for small

magnetic fields/large mini-gaps when the LLs cross, or for small values of the mini-gap when the levels in a doublet are almost degenerate) significant deviation from the SLLA can occur. Thus, the applicability of the SLLA puts constraints onto the external parameters. This point is discussed in details later. And now we move to the two-particle problem in bilayer graphene in the SLLA.

1.2.3 Interaction of two electrons in a Landau level of bilayer graphene

The two-particle problem within the SLLA in bilayer graphene can be solved analogously to the non-relativistic case.

Define the projections of the relative and the center of mass full angular momenta to a single Landau level:

$$\hat{J}^p_{rel/cm} = \hat{L}^p_{rel/cm} + \frac{1}{2}(\Sigma_1 + \Sigma_2) = \frac{1}{2}(\hat{J}_1 + \hat{J}_2 \mp (b_1^\dagger b_2 + b_2^\dagger b_1)). \tag{1.53}$$

The commutation relations of the projected angular momenta and their raising and lowering operators with the parts of the two-particle Hamiltonian are absolutely similar to the non-relativistic case:

$$\hat{H}^{BLG}_{2-part} = \hat{H}^{BLG}_{free} + V(r), \tag{1.54}$$

$$\hat{H}^{BLG}_{free} = \hat{H}^{BLG}_{1-part,1} + \hat{H}^{BLG}_{1-part,2}, \tag{1.55}$$

$$\left[\hat{H}^{BLG}_{free}, \hat{J}^p_{rel/cm}\right] = 0 \quad , \quad \left[\hat{H}^{BLG}_{free}, \hat{b}_1^\dagger \mp \hat{b}_2^\dagger\right] = 0, \tag{1.56}$$

$$\left[\hat{H}^{BLG}_{free}, \hat{b}_1 \mp \hat{b}_2\right] = 0 \quad , \quad \left[\hat{V}, \hat{J}^p_{rel/cm}\right] = 0, \tag{1.57}$$

$$\left[\hat{V}, \hat{b}_1^\dagger + \hat{b}_2^\dagger\right] = 0 \quad , \quad \left[\hat{V}, \hat{b}_1 + \hat{b}_2\right] = 0, \tag{1.58}$$

$$\left[\hat{V}, \hat{b}_1^\dagger - \hat{b}_2^\dagger\right] \neq 0 \quad , \quad \left[\hat{V}, \hat{b}_1 - \hat{b}_2\right] \neq 0. \tag{1.59}$$

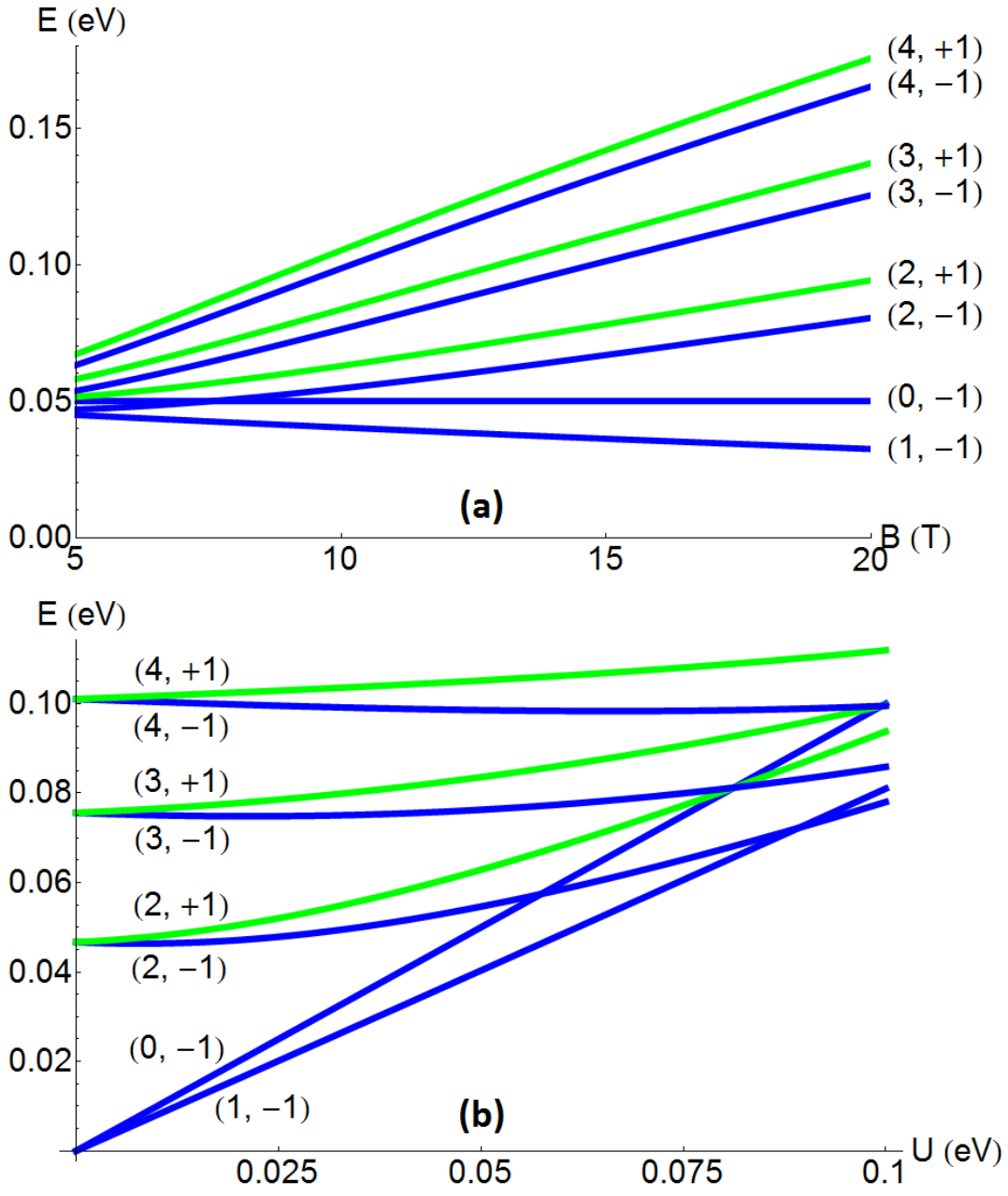

Figure 1.1: **Dependence of the lowest LLs' energies on (a) the magnetic field B for $U = 50$ meV, and (b) on the mini-gap parameter U for $B = 10$ T.** Each level is labeled by a pair of quantum numbers (n, ξ). Only positive-energy part of the spectrum is shown.

The eigenstates of the two "angular momenta" in a Landau level have the form

$$|m,M\rangle = \frac{1}{\sqrt{2^{m+M}m!M!}}(\hat{b}_1^\dagger - \hat{b}_2^\dagger)^m(\hat{b}_1^\dagger + \hat{b}_2^\dagger)^M(\Psi_{n,-n}^{\xi s})_1(\Psi_{n,-n}^{\xi s})_2, \tag{1.60}$$

$$\begin{aligned} \hat{J}_{rel}^p|m,M\rangle &= (m-n+1)|m,M\rangle, & (1.61)\\ \hat{J}_{cm}^p|m,M\rangle &= (M-n+1)|m,M\rangle. & (1.62) \end{aligned}$$

Thus, just like in a non-relativistic system, the two-particle interaction potential in a Landau level can be expressed through pseudopotentials:

$$\hat{V}(r) = \sum_{m,M} |m,M\rangle V_m^{n,\xi,s} \langle m,M|. \tag{1.63}$$

The expression for the pseudopotentials in terms of matrix elements of the potential is straightforward as the states $|m,M\rangle$ are orthonormal. These pseudopotentials can be expressed via the non-relativistic pseudopotentials:

$$\begin{aligned} V_m^{n,\xi,s} = |A_n^{\xi s}|^4 V_m^{(n,n)} + |B_n^{\xi s}|^4 V_m^{(n-2,n-2)} + \\ (|C_n^{\xi s}|^2 + |D_n^{\xi s}|^2)^2 V_m^{(n-1,n-1)} + \\ 2|A_n^{\xi s}|^2 |B_n^{\xi s}|^2 V_m^{(n,n-2)} + \\ 2|A_n^{\xi s}|^2 (|C_n^{\xi s}|^2 + |D_n^{\xi s}|^2) V_m^{(n,n-1)} + \\ 2|B_n^{\xi s}|^2 (|C_n^{\xi s}|^2 + |D_n^{\xi s}|^2) V_m^{(n-2,n-1)}. \end{aligned} \tag{1.64}$$

This expression makes obvious the possibility of tuning of the pseudopotentials by changing the values of the amplitudes $A_n^{\xi s}, B_n^{\xi s}, C_n^{\xi s}, D_n^{\xi s}$. Since the amplitudes depend on the external parameters U and B, the pseudopotentials can be tuned with the help of external perpendicular electric and magnetic fields.

For practical purposes it is useful to incorporate formula (1.32) into Eq. (1.64)

which leads to

$$V_m^{n,\xi,s} = \int_0^\infty \tilde{V}(q) L_m(q^2) \left(F_n^{\xi s}(q^2/2)\right)^2 e^{-q^2} \frac{qdq}{2\pi}, \tag{1.65}$$

$$F_n^{\xi s}(q^2/2) = |A_n^{\xi s}|^2 L_n(q^2/2) + |B_n^{\xi s}|^2 L_{n-2}(q^2/2) + (|C_n^{\xi s}|^2 + |D_n^{\xi s}|^2) L_{n-1}(q^2/2). \tag{1.66}$$

After pseudopotentials are calculated the numerical diagonalization procedure is absolutely similar to the non-relativistic case[9].

Let us emphasize that the consideration above is a consideration within the SLLA. As it is discussed in the next section, in BLG the SLLA is less justified than in GaAs systems. There are, however, conditions when the SLLA is a good approximation; in that regime the multi-LL physics can be incorporated into the SLLA by means of introducing corrections to the interaction potential and the pseudopotentials.

1.2.4 Summary of the section

In this section the explicit formulae for the SLLA in BLG are provided (wave functions in a Landau level, expression for the pseudopotentials). It is shown that application of the numerical diagonalization methodology to BLG system within the SLLA does not differ too much from the application to a non-relativistic system.

[9]Recall that though the trial wave functions are written in the form of complex polynomials, they, in fact, give decomposition of the wave function into Slater determinants of the single particle states. Thus they are applicable to any system with Landau levels having structure similar to the non-relativistic case, so they are applicable to the BLG. If a trial state is written in the basis of occupation numbers the only difference to the diagonalization and comparison procedure is that one has to use the BLG pseudopotentials instead of the non-relativistic ones.

1.3 Deviations from the single Landau level approximation in bilayer graphene

As discussed in the previous section, studying FQHE in BLG within the SLLA does not differ too much from the non-relativistic case. However, as it has already been mentioned the single-particle spectrum of BLG restricts applicability of the SLLA, and under the usual experimental conditions the restriction is significant. Depending on several factors, there are three regimes:

- when the SLLA is fully reliable;
- when one has to consider several Landau levels together since the electrons partially occupy each of those, the SLLA is completely inapplicable;
- in between the two previous regimes, the effects of presence of other Landau levels can be incorporated into the SLLA as corrections to the intra-level electron-electron interaction.

In this section we discuss factors which determine boundaries between the regimes, we also show how to take into account the corrections in the third regime. First, the brief discussion is presented in the subsection 1.3.1, with technical details are presented in the subsection 1.3.2.

1.3.1 Effects important in bilayer graphene

Now we discuss in details the effects which are important in BLG. As before, we are working in quite a good approximation when interaction does not change spin quantum numbers of electrons. The important effects are as follows:

- Firstly, BLG in perpendicular electric field is a narrow gap semiconductor, thus the effects of vacuum polarization are strong [15].
- Secondly, Coulomb interaction of electrons can lead to mixing of Landau levels, or to emergence of spin or/and valley unpolarized states. Coulomb

interaction can also lead to intervalley hopping of electrons. Even though such processes are suppressed compared to intravalley scattering one should still estimate their relevance.

- Thirdly, even when LL mixing is small, virtual hopping between the LLs can change (renormalize) intra-level electron-electron interaction.

Now, in more details about each of those.

1.3.1.1 Vacuum polarization

The virtual processes shown in Fig. 1.2a lead to renormalization of the electron-electron interaction. This is important since the interaction determines the FQHE. The Fourier transform of the renormalized (screened) interaction potential can be expressed as[10]

$$\tilde{V}_{scr}(q) = \frac{\tilde{V}(q)}{1 + l^2 \tilde{V}(q) \Pi(q, \omega = 0)} \tag{1.67}$$

where $\tilde{V}(q) = 2\pi e^2/(lq\kappa)$ is the Fourier transform of the unscreened Coulomb potential, κ is the dielectric constant, which is felt by the system's electrons[11], and $\Pi(q, \omega)$ is the polarization function. Since we are interested in the effects at the energy scales much less than the inter-LL distances we can neglect the retardation effects (use only $\omega = 0$).

We compute the polarization function for the BLG in magnetic field within the RPA (random phase approximation), which can be justified within the $1/N$-expansion [15] ($N = 2$ spin projections $\times$ 2 valleys $= 4$). Since $\Pi(q, \omega = 0) \propto q^2$, screening is not efficient at large distances; however, it strongly affects the first few Haldane pseudopotentials (corresponding to distances of the order of the magnetic length) which have the most significant impact on the stability of any FQHE state. Details of the calculation are described in the paragraph 1.3.2.1.

[10] A similar screening approach has been discussed in GaAs; see, for example, [16].

[11] The dielectric constant sensed by BLG is $\kappa = (\kappa_1 + \kappa_2)/2$, where κ_1 and κ_2 are the dielectric constants of the environment below and above the sheet of BLG.

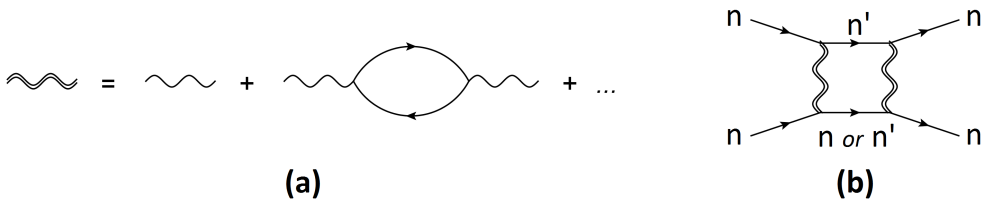

Figure 1.2: **Feynman diagrams showing renormalization of the electron-electron interaction** due to (a) the vacuum polarization processes, and (b) the simplest processes involving virtual hopping of one or both of the two interacting electrons from the n-th LL to the n'-th LL.

1.3.1.2 Landau level mixing and population reversal

The order of levels in Fig. 1.1 prescribes the natural order of filling of the LLs by electrons in the independent electrons approximation. However, it can happen that for some filling fractions the electron-electron interaction leads to a reversal of this natural order in a part of parameter space (by external parameters we mean the magnetic field, the mini-gap and the dielectric constant). For example, the Coulomb energy of the fully filled $(2, +1)$ LL is less than the one of the fully filled $(2, -1)$ for $U > 0$. In the region where the interaction is strong compared to the gap between the two levels this can lead to the fully filled $(2, +1)$ LL having lower total energy than the fully filled $(2, -1)$ level. Thus, the former would be filled before the latter.

Whereas for fractional filling such effects are much more difficult to analyze, population reversal at the integer filling fraction would be an indicator of a strong violation of the SLLA. Thus, we constrain our analysis to the region of the parameter space where no population reversal occurs at integer filling. More details on the population reversal issues are presented in paragraph 1.3.2.2.

When the quasidegenerate levels are from different valleys, valley-unpolarized states may be preferred, particularly for fractional filling. Furthermore, when the quasidegenerate levels are from the same valley (as in the $n = 0$ and $n = 1$ case) level mixing may occur. These are interesting effects which are, however, beyond the scope of this work.

In any of the cases (valley unpolarized state or level mixing) one has to consider

several LLs simultaneously. On the one hand, this is hard technically since for the same number of electrons the system's Hilbert space is significantly larger, which complicates use of numerical diagonalization. On the other hand, in such cases it is extremely unlikely to find a state similar to the ones expected for one LL. Therefore, we restrict study to the region of the parameter space where no valley unpolarized states and no level mixing occur. Our criteria for smallness of level mixing and valley unpolarization are discussed in paragraph 1.3.2.2.

For the valley-polarized states one can still investigate whether the state is spin polarized. Generally, spin-unpolarized states are not favored by Coulomb repulsion unless the potential/list of pseudopotentials is hollow core (does not fall off monotonically with distance/relative angular momentum). We find that the screened potentials do fall off monotonically for $\kappa \gtrsim 10$ in all the cases considered in section 1.4. For $\kappa \lesssim 10$ the potential does not fall off monotonically in some regions of the parameter space. However, the non-monotonicity of the list of pseudopotentials in the latter case is either absent or very small. Therefore, we consider only spin-polarized states and do not further restrict the external parameters' region due to possible spin-unpolarization issues.

1.3.1.3 Renormalization of pseudopotentials due to virtual hopping

The SLLA is exact in the limit of infinite difference of energies ΔE between the LLs. For finite ΔE the pseudopotentials acquire corrections due to virtual transitions between the LLs such as, for example, shown in Fig. 1.2b. Such corrections are theoretically tractable only in the perturbative regime (when they are small); however, even the presence of small corrections may dramatically affect the phase diagram due to the extreme sensitivity of the FQHE states to the details of the interaction (see e.g. [11]).

We restrict the region of validity of our consideration by requiring the typical interaction energy scale (it can be interaction potential value at the magnetic length distance or, almost equivalently, the zeroth pseudopotential) to be smaller

than the distances to each of the neighbouring LLs from the same valley. In these regions we take into account corrections to the pseudopotentials up to the second order perturbation theory (Fig. 1.2b).

Similar but higher order processes lead to emergence of three-body, four-body etc. electron-electron interactions. We neglect those interactions. This is justified by the fact that the typical interaction energy scale is smaller than the inter-LL distance, therefore higher order processes should be suppressed compared to the lower order ones.

The details of the calculation of the corrections are presented in the paragraph 1.3.2.3.

1.3.1.4 General plan for numerical study of a fractional QHE in bilayer graphene

With the remarks made above, the general plan for study of FQHE at a certain filling fraction on a certain LL can be formulated as follows:

1. Calculate the screened interaction potential.

2. Determine the region of parameter space in which no valley unpolarized states emerge and level mixing doesn't take place[12].

3. Calculate pseudopotentials in this region of parameter space. Take the corrections due to virtual hopping into account (the modified SLLA).

4. Use the calculated corrected pseudopotentials for numerical diagonalization and compare the exact numerically found ground state with the trial one.

The next subsection contains details of calculation of the polarization function, of the corrections to the pseudopotentials, of the criterion for absence of population reversal of LLs, and of the criteria for absence of valley unpolarization and LL mixing.

[12]By external parameters we mean the magnetic field, the mini-gap parameter and the dielectric constant.

1.3.2 Effects important in bilayer graphene: calculation details

1.3.2.1 Calculation of the polarization function

The polarization function within the RPA is just a density-density correlation function[13] in the free theory (this corresponds to the fermionic loop in Fig. 1.2a)

$$\Pi(\vec{r}-\vec{r}',t-t') = -i\langle T\rho(\vec{r},t)\rho(\vec{r}',t')\rangle, \tag{1.68}$$

$\hbar$ is put to be 1 in this paragraph, the T-symbol denotes time ordering:

$$T\rho(\vec{r},t)\rho(\vec{r}',t') = \begin{cases} \rho(\vec{r},t)\rho(\vec{r}',t'), t > t' \\ \rho(\vec{r}',t')\rho(\vec{r},t), t < t' \end{cases}. \tag{1.69}$$

The density-density correlator is translation-invariant since the system is uniform, so

$$\langle T\rho(\vec{r},t)\rho(\vec{r}',t')\rangle = \langle T\rho(\vec{r}-\vec{r}',t-t')\rho(\vec{0},0)\rangle. \tag{1.70}$$

Let's denote the set of quantum numbers (n,m,ξ,s) by k, and write $k < k_F$ if the state is occupied, and $k > k_F$ otherwise. The polarization function can be expressed with the help of the wave functions (1.48) in the following way:

$$\Pi(\vec{r},t) = -2i\left[\sum_{k<k_F,k'>k_F,\xi=\xi'} \Psi_k(x)^\dagger\Psi_{k'}(x)\Psi_{k'}(0)^\dagger\Psi_k(0)\times e^{i(E_k-E_{k'})t}\theta(t) + \right.$$
$$\left. \sum_{k>k_F,k'<k_F,\xi=\xi'} \Psi_k(x)^\dagger\Psi_{k'}(x)\Psi_{k'}(0)^\dagger\Psi_k(0)\times e^{i(E_k-E_{k'})t}\theta(-t)\right], \tag{1.71}$$

$$\theta(x) = \begin{cases} 1, x > 0 \\ 0, x < 0 \end{cases}. \tag{1.72}$$

The factor of 2 in front of the square brackets is due to spin.

[13]Density is meant to be normal ordered: electron/hole creation operators should be to the left of the annihilation operators.

The Fourier transform of the polarization function is then defined as

$$\Pi(\vec{q},\omega) = \int d^2 r dt e^{-i(\vec{q}\vec{r}/l - \omega t)} \Pi(\vec{r},t). \tag{1.73}$$

So the polarization function at the zero frequency $\Pi(\vec{q},\omega=0)$, which we need to find the interaction potential, can be expressed like

$$\Pi(\vec{q},\omega=0) = 2 \sum_{k>k_F, k'<k_F, \xi=\xi'} \frac{1}{E_k - E_{k'}} \times \int d^2 r e^{-i\vec{q}\vec{r}/l} (\Psi_k(x)^\dagger \Psi_{k'}(x) \Psi_{k'}(0)^\dagger \Psi_k(0) + c.c.). \tag{1.74}$$

After a short calculation we find that

$$\Pi(\vec{q},\omega=0) = \frac{2}{l^2} \sum_{j>j_F, j'<j_F, \xi=\xi'} \frac{1}{E_j - E_{j'}} \times (I_{n,s,n',s'} + c.c.) = \frac{1}{l^2 \hbar \omega_c} \Pi_{dimless}(q), \tag{1.75}$$

$$\begin{aligned} I_{n,s,n',s'} = (-1)^{(n-n')} \int_0^\infty dr\ r J_0(qr/l) \times \Big[& A_n^{\xi s} \overline{A_{n'}^{\xi s'}} \Big(\overline{A_n^{\xi s}} A_{n'}^{\xi s'} \overline{\psi_{n,0}(w)} \psi_{n',0}(w) + \\ & \overline{B_n^{\xi s}} B_{n'}^{\xi s'} \overline{\psi_{n-2,2}(w)} \psi_{n'-2,2}(w) + (\overline{C_n^{\xi s}} C_{n'}^{\xi s'} + \overline{D_n^{\xi s}} D_{n'}^{\xi s'}) \overline{\psi_{n-1,1}(w)} \psi_{n'-1,1}(w) \Big) + \\ & B_n^{\xi s} \overline{B_{n'}^{\xi s'}} \Big(\overline{A_n^{\xi s}} A_{n'}^{\xi s'} \overline{\psi_{n,-2}(w)} \psi_{n',-2}(w) + \overline{B_n^{\xi s}} B_{n'}^{\xi s'} \overline{\psi_{n-2,0}(w)} \psi_{n'-2,0}(w) + \\ & (\overline{C_n^{\xi s}} C_{n'}^{\xi s'} + \overline{D_n^{\xi s}} D_{n'}^{\xi s'}) \overline{\psi_{n-1,-1}(w)} \psi_{n'-1,-1}(w) \Big) + \\ & (C_n^{\xi s} \overline{C_{n'}^{\xi s'}} + D_n^{\xi s} \overline{D_{n'}^{\xi s'}}) \Big(\overline{A_n^{\xi s}} A_{n'}^{\xi s'} \overline{\psi_{n,-1}(w)} \psi_{n',-1}(w) + \overline{B_n^{\xi s}} B_{n'}^{\xi s'} \overline{\psi_{n-2,1}(w)} \psi_{n'-2,1}(w) \\ & + (\overline{C_n^{\xi s}} C_{n'}^{\xi s'} + \overline{D_n^{\xi s}} D_{n'}^{\xi s'}) \overline{\psi_{n-1,0}(w)} \psi_{n'-1,0}(w) \Big) \Big]. \end{aligned} \tag{1.76}$$

where j denotes a set (n,ξ,s), overbar denotes complex conjugation.[14] The inte-

[14]Note that for some values of n, n' this general expression has the non-defined wave functions like, e.g., $\psi_{n'-2,0}(w)$ for $n'=0$ or $n'=1$. These terms, however, do not contribute, which is ensured by the coefficients $B_{n'}^{\xi s'}$, $C_n^{\xi s}$ etc. which take zero values in those cases.

grals can be found analytically:

$$\int_0^\infty dr\ rJ_0(qr/l)\overline{\psi_{n,m}(w)}\psi_{n',m}(w) = \frac{1}{2\pi}\int d^2r\overline{\psi_{n,m}(w)}e^{i\vec{q}\vec{r}/l}\psi_{n',m}(w) = \frac{1}{2\pi}F_{n,n'}(x)F_{n+m,n'+m}(\bar{x})e^{-q^2/2}, \quad (1.77)$$

$$F_{i_1,i_2}(x)|_{i_1\geq i_2} = \sum_{k=0}^{i_2}\frac{\sqrt{i_1!i_2!}}{k!(k+i_1-i_2)!(i_2-k)!}\left(-\frac{|x|^2}{2}\right)^k\left(\frac{ix}{\sqrt{2}}\right)^{i_1-i_2} = \sqrt{\frac{i_2!}{i_1!}}\left(\frac{ix}{\sqrt{2}}\right)^{i_1-i_2}L_{i_2}^{(i_1-i_2)}(|x^2|/2), \quad (1.78)$$

$$F_{i_1,i_2}(x)|_{i_1\leq i_2} = F_{i_2,i_1}(\bar{x}), \quad (1.79)$$

where $x = q_x + iq_y$, and $L_n^{(\alpha)}$ are generalized Laguerre polynomials. The derivation is very similar to the derivation of formula (1.32) presented in Appendix A.1.

The Fourier transform of the interaction potential (1.31), (1.67) can be expressed then as

$$\tilde{V}_{scr}(q) = \frac{2\pi e^2}{\kappa q l}\frac{1}{1+2\pi\frac{e^2/(l\kappa)}{\hbar\omega_c}\frac{\Pi_{dimless}(q)}{q}}. \quad (1.80)$$

We take into account not only fully filled or entirely empty LLs but the partially filled ones as well. We do this with the help of the following approximation: for a partially filled level we add terms which correspond to the level as an empty one and as a filled one with coefficients $(1-\{\nu\})$ and $\{\nu\}$ respectively. For example, if some level is half-filled then all the terms in the polarization function which correspond to the hopping to this level appear with the coefficient $1/2 = 1 - 1/2$, and the terms which correspond to hopping from this level also appear with the coefficient $1/2$. Thus, we do not take into account correlations in a partially filled LL.

For this work the polarization function was calculated approximately: we cal-

culated only terms with $n, n' \leq n_{cutoff} = 4$. We checked that the pseudopotentials in the region we are interested in differ from the pseudopotentials calculated with $n_{cutoff} = 3$ by less than 2%.

1.3.2.2 Population reversal of Landau levels and level mixing

It was discussed in paragraph 1.3.1.2 that when typical energy scale of the electron-electron interaction becomes larger than the difference of kinetic energies of two LLs from the same valley it is natural to expect the SLLA to break down. The numerical study in such cases is significantly hampered. Moreover, it is hardly probable to find a state similar to a single-level state in this regime of strong level mixing. Therefore, we would like to work only in the regime where the mixing of LLs is small. For this we demand the typical energy scale of the electron-electron interaction to be smaller than the kinetic energy distance to the closest LL from the same valley. The remnants of the level mixing can be incorporated then into the corrections to the SLLA which are discussed in the next paragraph.

One can use different quantities to define the typical energy scale of the electron-electron interaction. For example, one can use the interaction potential value at the magnetic length distance $V(l)$ or the zeroth pseudopotential at the LL one is interested in $V_0^{n,\xi,s}$. They typically differ by a factor of order of unity, which is not too important. We choose to use value of the zeroth pseudopotential as the typical interaction energy scale. Therefore, we restrict the region of consideration to those values of external parameters U, B, κ for which $V_0^{n,\xi,s} \leq \Delta E$, where ΔE is the kinetic energy difference between the LL under consideration and the closest to it another LL.

There is a subtlety regarding this restriction. One can use the zeroth pseudopotential for the screened or for the bare Coulomb interaction potential. Using the Coulomb pseudopotential seems natural as it is the fundamental perturbation theory controlling parameter. However, for the weakened screened potential the Landau level mixing is smaller, and restricting the applicability region by Coulomb

interaction scale one excludes where our approach should still give reliable results. On the other hand, if the screening is so strong that the Coulomb energy scale significantly differs from the screened one, then the RPA approach we use for calculation of the screened potential may be not good enough, bringing in an error in the interaction potential. In section 1.4 we restrict our region of consideration by the screened energy scale. However, we also show the Coulomb energy scale restricted region, so the reader can decide what restriction is more appropriate on his own.

Besides mixing of LLs from one valley, a similar process can take place for neighbouring levels from different valleys like $(2, \pm 1)$ (see Fig. 1.1). This is due to Coulomb interaction on the lattice scale that can make electrons jump from one valley to another. This interaction is considered in more detail in [17]. What is important for us is that the typical energy scale of this interaction is

$$\tilde{V}_{\text{Coul}}(q)\Big|_{q=\frac{4\pi l}{3a}} = \frac{2\pi e^2}{\kappa q l}\Big|_{q=\frac{4\pi l}{3a}} = \frac{3e^2 a}{2\kappa l^2}, \tag{1.81}$$

where $a \approx 0.25$nm is the graphene lattice constant. We would like this interaction not to play a significant role. Therefore we restrict the parameters region by demanding that its energy scale is smaller than the distance between the LL under consideration and the closest to it LL from the different valley.[15]

Suppose level mixing of LLs from different valleys can be neglected. However, the electron-electron interaction can lead to a situation when filling a higher LL is energetically preferable than the lower one. This may lead to a situation when two levels are partially filled at the same time. If this happens, the two LLs, even not mixing, influence each other through the density-density interaction (since the electrons still repel each other). In such case the two levels from different valleys

[15]Unlike the case of level mixing in one valley, due to quasi-momentum conservation, mixing of the LLs from different valleys can happen only if both of them are filled with electrons at least partially. Naively, one would think that because of this argument the level $(2, +1)$ is not dangerous when we consider the $(2, -1)$ LL. However, the screening processes happen because of hopping of the electrons to higher LLs. Therefore, the $(2, +1)$ LL is "virtually" filled, to some extent. Thus, to be on the safe side, we still apply this restriction when we consider the $(2, -1)$ LL.

should be considered together just like in the case of level mixing. So from the same reasoning as in the case of mixing, we do not want to consider the system in the regime of two levels from different valleys partially filled.

Thus, we need to find the region of parameter space where such simultaneous filling does not occur — in order to use the SLLA there. Since the case of partially filled level is hard to analyze, as a criterion we choose the demand that for integer fillings there should be no change of the filling order. I.e., the full energy (kinetic plus interaction) per electron of fully filled levels should put them in the same order as their kinetic energy. For example, if the kinetic energy of the $(2,-1)$ LL is less than the one of the $(2,+1)$ LL, then the full energy per electron in the fully filled $(2,-1)$ level should also be less than the full energy per electron in the fully filled $(2,+1)$ level.

For the fully filled level it is easy to calculate its interaction energy since there is only one state possible — the Slater determinant of all the level's orbits. The interaction energy can be expressed through the pseudopotentials:

$$E_{\text{inter., } N\text{electrons}} = \frac{N(N-1)}{2}\text{Tr } \hat{V}\hat{\rho}_2, \tag{1.82}$$

$$E_{\text{inter. pp}} = \lim_{N\to\infty} \frac{E_{inter.,Nelectrons}}{N} = 2\sum_{m\in 2\mathbb{N}-1} V_m, \tag{1.83}$$

where $\hat{\rho}_2$ is the two-particle density matrix, pp in the subscript stands for "per particle".

This energy can be separated into the Hartree (density-density interaction) and the Fock (exchange) parts:

$$E_{\text{Hartree pp}} = \sum_{m=0}^{\infty} V_m = \frac{1}{2l^2}\int_0^\infty dr\ rV(r), \tag{1.84}$$

$$E_{\text{Fock pp}} = \sum_{m=0}^{\infty} (-1)^{m+1} V_m = \frac{1}{2l^2}\int_0^\infty dr\ rV(r)g(r). \tag{1.85}$$

The function $g(r)$ is related to two-particle and one-particle density matrices

ρ_2 and ρ_1:

$$\rho_1(x'|x) = \langle x'|\hat{\rho}_1|x\rangle, \tag{1.86}$$

$$\rho_2(x'y'|xy) = \langle x'| \otimes \langle y'| \ \hat{\rho}_2 \ |x\rangle \otimes |y\rangle, \tag{1.87}$$

$$\rho_2(x'y'|xy) = |N \to \infty, \text{Slater determinant state}| = \\ (\rho_1(x'|x)\rho_1(y'|y) - \rho_1(y'|x)\rho_1(x'|y)), \tag{1.88}$$

$$g(r) = N^2(\rho_2(r,0|r,0) - \rho_1(0|0)^2), \tag{1.89}$$

$$g(r) = -N^2\rho_1(0|r)\rho_1(r|0). \tag{1.90}$$

Notice that the Hartree energy can be expressed as an integral of the interaction potential, with the form of the integral independent of a Landau level. This is a consequence of the fact that the fully filled LL has constant density. We have to say that the integral for the Hartree energy is divergent at the upper limit for the Coulomb-like interaction potentials. However, only differences of the energies have physical meaning, thus we can calculate this integral with a certain regularization if only the regularization is always the same.

The Fock part of the energy is, on the contrary, convergent, but it depends on the LL through the function $g(r)$, which characterizes short-range correlations.

If the interaction potential is the same for two different Landau levels, their Hartree energies are identical. Naively one would think that if the screening is different, their Hartree energies can lead to population order reversal. However, one has to take into account the background positive charge (since the system is electrostatically neutral). The total electrostatic energy then, as we show in Appendix A.2, does not differ for different screened potentials.

Therefore, the interaction energy difference comes from the Fock term only. For the non-relativistic levels and the Coulomb potential the Fock energy is the greater (has smaller absolute value but negative sign) the bigger is level number n. This is an additional reason (the main is the large dielectric constant) for absence

of population reversal in the non-relativistic systems: interaction energy works together with the kinetic one.

Consider, for example, levels $(2,-1)$ and $(2,+1)$ in bilayer graphene (the latter has greater kinetic energy). The wave functions in the $(2,+1)$ level are close to the wave functions of the non-relativistic $n=0$ LL, while the wave functions in $(2,-1)$ are close to the ones in $n=2$. Thus, the Fock energy prefers the $(2,+1)$ LL, while the kinetic energy prefers the $(2,-1)$ LL. Therefore if the interaction is strong enough population reversal may happen.

While for the bare Coulomb interaction population reversal would happen in some regions of the parameter space, for the screened potentials we do not find such an effect for the $(2,-1)$ and $(2,+1)$ LLs. This makes improbable emergence of valley-unpolarized states.

Therefore, it is enough to restrict the region of parameter space by demanding the smallness of level mixing for LLs from one valley and from different valleys according to the criteria described in the beginning of this paragraph.

1.3.2.3 Calculation of corrections to the SLLA pseudopotentials due to virtual hopping

Suppose we are in the region where spin-/valley-unpolarized states do not emerge, and the LL mixing of the level under consideration with the levels from the same valley is small. Then the small mixing can be taken into account with the help of corrections to the electron-electron interaction within the SLLA. Those are the small corrections to the pseudopotentials. It is known that small corrections of the order of $5-10\%$ from the pseudopotentials' values can lead to significant change of the overlap with a trial state (see e.g. [11]). In this paragraph we present the formulae we use to compute such corrections.

Consider the two-particle problem. In the subsection 1.2.3, it was shown that the eigenstates of the two-particle problem within the SLLA are $|m,M\rangle$, with their energies being V_m^j, $j=(n,\xi,s)$. Let us denote $|m,M\rangle$ as $|m,M,j,j\rangle$ to emphasize

that both of the electrons are in the LL j. Now we add to our consideration the closest unfilled LLs from the same valley (for small deviations from the naive SLLA those are the levels above); we introduce the following basis in the Hilbert space:

$$|m, M, j, j'\rangle = \frac{1}{\sqrt{2^{m+M} m! M!}} (\hat{b}_1^\dagger - \hat{b}_2^\dagger)^m (\hat{b}_1^\dagger + \hat{b}_2^\dagger)^M (\Psi^{\xi s}_{n,-n})_1 (\Psi^{\xi s'}_{n',-n'})_2. \tag{1.91}$$

The leading correction to the eigenstates' energies, which is due to the virtual hopping to the higher LLs from the same valley, is given by the second order perturbation theory:

$$E_m^j = V_m^j - \sum_{(j_1,j_2)\neq(j,j),m',M'} \frac{|\langle m, M, j, j|\hat{V}|m', M', j_1, j_2\rangle|^2}{E_{j_1}^{kin} + E_{j_2}^{kin} - 2E_j^{kin}}. \tag{1.92}$$

Express the square of the distance between the two interacting electrons $r^2 = l^2|w_1 - w_2|^2$ through the operators (1.3-1.4):

$$r^2 = 2l^2(\hat{b}_1 - \hat{b}_2 + \hat{a}_1^\dagger - \hat{a}_2^\dagger)(\hat{a}_1 - \hat{a}_2 + \hat{b}_1^\dagger - \hat{b}_2^\dagger). \tag{1.93}$$

Since the interaction potential V is a function of r^2, one can show that the only non-zero matrix elements of all the $\langle m, M, j, j|\hat{V}|m', M', j_1, j_2\rangle$ are

$$V_m^{j,j,j_1,j_2} = \langle m, M, j, j|\hat{V}|m + (n_1 - n) + (n_2 - n), M, j_1, j_2\rangle, \tag{1.94}$$

$$V_m^{j,j,j_1,j_2} = (-1)^{(n_1-n)+(n_2-n)} V_m^{j,j,j_2,j_1}. \tag{1.95}$$

These matrix elements can be expressed through non-relativistic matrix elements, similarly to how the pseudopotentials in BLG are expressed via the non-relativistic pseudopotentials:

$$|m, M, n, n'\rangle = \frac{1}{\sqrt{2^{m+M} m! M!}} (\hat{b}_1^\dagger - \hat{b}_2^\dagger)^m (\hat{b}_1^\dagger + \hat{b}_2^\dagger)^M (\psi_{n,-n})_1 (\psi_{n',-n'})_2, \tag{1.96}$$

$$V_m^{n,n',n_1,n_2} = \langle m, M, n, n'|\hat{V}|m + (n_1 - n) + (n_2 - n'), M, n_1, n_2\rangle, \tag{1.97}$$

$$V_m^{n,n,n_1,n_2} = (-1)^{(n_1-n)+(n_2-n)} V_m^{n,n,n_2,n_1}, \tag{1.98}$$

$$V_m^{j,j,j_1,j_2} = V_m^{n,n,n_1,n_2} \overline{A_n^{\xi s}}^2 A_{n_1}^{\xi s_1} A_{n_2}^{\xi s_2} + V_m^{n-2,n,n_1-2,n_2} \overline{B_n^{\xi s} A_n^{\xi s}} B_{n_1}^{\xi s_1} A_{n_2}^{\xi s_2} + ... \tag{1.99}$$

The non-relativistic matrix elements can be expressed through the Fourier transform of the pseudopotential in a form quite similar to the expression for the pseudopotentials (1.32):

$$V_m^{n,n',n_1,n_2} = \int_0^\infty \tilde{V}(q) F_{m,m+(n_1-n)+(n_2-n')}(\bar{x}\sqrt{2}) \times F_{n,n_1}(x) F_{n',n_2}(-x) e^{-q^2} \frac{qdq}{2\pi}, \tag{1.100}$$

$$F_{i_1,i_2}(x)|_{i_1 \geq i_2} = \sum_{k=0}^{i_2} \frac{\sqrt{i_1! i_2!}}{k!(k+i_1-i_2)!(i_2-k)!} \left(-\frac{|x|^2}{2}\right)^k \left(\frac{ix}{\sqrt{2}}\right)^{i_1-i_2} = \sqrt{\frac{i_2!}{i_1!}} \left(\frac{ix}{\sqrt{2}}\right)^{i_1-i_2} L_{i_2}^{(i_1-i_2)}(|x^2|/2), \tag{1.101}$$

$$F_{i_1,i_2}(x)|_{i_1 \leq i_2} = F_{i_2,i_1}(\bar{x}), \tag{1.102}$$

$x = q_x + iq_y$, and $L_n^{(\alpha)}$ are generalized Laguerre polynomials. The derivation is very similar to the derivation of formula (1.32) presented in the appendix A.1. Since $F_{n,n}(x) = L_n(|x|^2/2)$, for $n = n_1$, $n' = n_2$ the formula (1.32) is restored, as it should be because by definition $V_m^{(n_1,n_2)} = V_m^{n_1,n_2,n_1,n_2}$.

We neglected here the corrections to the two-particle interaction, three- and more-particle interactions which appear from the higher orders of the perturbation theory. It is permissible since in the regime we work in the typical interaction energy scale is less than the distance to the closest LL. Therefore, the subleading corrections are expected to be smaller than the leading ones coming from the second order perturbation theory.

The correction (1.92) calculated here corresponds to the diagram in Fig. 1.2b in the approximation of neglecting the dependence of the polarization function on

frequency and neglecting the self-energy of the electron (corrections to the electron propagator). This approximation is discussed in the Appendix A.3.

1.3.3 Summary of the section

In this section we discuss important effects which restrict the applicability of the SLLA in BLG. We also discuss the conditions under which it is enough to introduce corrections to the SLLA to restore the theory applicability. The details of the calculations are presented in the second subsection.

1.4 Possibility to observe the Moore-Read state in bilayer graphene

In order to investigate the role of the effects discussed above on the stability of FQHE states we focus on the Pfaffian state. Our choice is motivated by the following considerations. Firstly, this state is particularly sensitive to the details of the interaction so it is a good illustration for our analysis. Secondly, the stability of this state in BLG was investigated in Refs. [6, 18] in the SLLA approximation but without these effects taken into account, so we can compare the phase diagrams. Thirdly, the Pfaffian itself is an important state because it is an example of the non-abelian topological fluid.

The tunable parameters are the magnetic field B, the electric field which determines the mini-gap parameter U and the effective dielectric constant κ[16] which controls the deviation from the naive SLLA (which is exact for $\kappa \to \infty$). We can also choose the half-filled LL number. Here we will concentrate only on the two levels: $(1,-1)$ and $(2,-1)$. The $(1,-1)$ level wave function is constructed from the nonrelativistic $n=0$ and $n=1$ LL wave functions, the $(2,-1)$ level wave function is constructed from the nonrelativistic $n=0,1,2$ LL wave functions. In both cases

[16]The dielectric constant sensed by BLG is $\kappa=(\kappa_1+\kappa_2)/2$, where κ_1 and κ_2 are the dielectric constants of the environment below and above the sheet of BLG.

for the bare Coulomb interaction one can tune the pseudopotentials close to their values at the nonrelativistic $n = 1$ LL, where the 5/2 state is observed in GaAs[17].

The tuning mechanisms are, however, different for the two levels. Amplitudes of the wave function (1.48) in the $(1, -1)$ LL show little dependence on U so the main control parameter is B[18]. In contrast, the amplitudes of the wave function in the $(2, -1)$ LL mainly depend on one parameter which is the $U/\hbar\omega_c$ ratio, so both B and U can be used for tuning.

The main factors determining deviation from the naive SLLA for the two levels are the polarization and virtual hopping to the nearby levels. For the $(1, -1)$ LL this is hopping to the $(0, -1)$ and the $(2, -1)$ LLs, while for the $(2, -1)$ LL the important hopping is to the $(3, -1)$ LL. In addition to this, for the $(2, -1)$ LL, it is important to consider effects of mixing with the $(0, -1)$ and $(2, +1)$ LLs. The latter are important factors restricting the region of applicability of perturbative analysis, however, when suppressed they do not lead to a renormalization of the intra LL interaction.

Figures 1.3a and 1.3b show the regions of the applicability of perturbative analysis for different values of κ for the $(1, -1)$ LL.[19] For Fig. 1.3a the typical interaction energy scale, which determines the significance of level mixing, is estimated with the help of the screened potential ("type S estimate"), while for Fig. 1.3b — with the help of the bare Coulomb potential ("type C estimate"). The regions are bounded from above by the condition of small hopping to the $(2, -1)$ LL, the lower bound is due to the condition of small hopping to the $(0, -1)$ LL. At small enough magnetic fields at least one of the conditions is violated at all values of U. The thick black line shows where the maximum overlap with the Pfaffian for the bare

[17]Though the $(2, +1)$ level wave function is also constructed from the nonrelativistic $n = 0, 1, 2$ LL wave functions the numerics shows that the high overlap with the Pfaffian state is not achieved here for the bare Coulomb interaction in contrast to the $(1, -1)$ and the $(2, -1)$ LLs.

[18]In the low-energy two-band model [14] (which corresponds to the $\gamma_1 \to \infty$ limit) such tuning is impossible because the amplitude $A_1^{-1,+1}$ is identically equal to 1 with other amplitudes being zero.

[19]Due to some mistakes in calculation of the region of applicability, in the original result-reporting paper [19] the form of the region is not entirely correct. Here we corrected the mistakes. This applies to both the $(1, -1)$ LL and the $(2, -1)$ LL case, which is considered next.

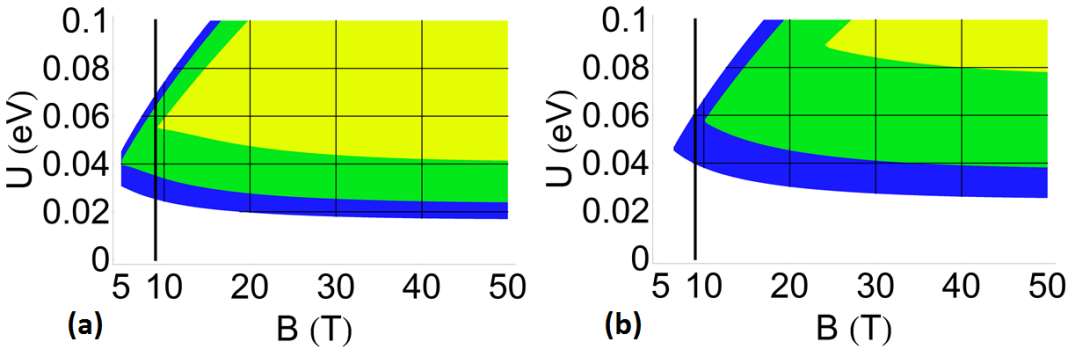

Figure 1.3: **The region of the applicability of perturbative analysis for fixed values of $\kappa = 5$ (yellow), 10 (green) and 15 (blue) for the $(1, -1)$ LL.** The size of the region increases with increasing κ. For (a) the typical interaction energy scale is taken to be the zeroth pseudopotential of the screened interaction potential, for (b) — of the bare Coulomb potential. The thick black line shows where the maximum overlap with the Moore-Read Pfaffian state for the bare Coulomb interaction is achieved.

Coulomb interaction is achieved. One can see that for small dielectric constants this line lies outside the region of validity of perturbative analysis, however for large enough κ they intersect near $U = 50$ meV.

Figures 1.4a and 1.4b show the regions of the applicability of perturbative analysis for different values of κ for the $(2, -1)$ LL. For Fig. 1.4a the type S estimate is used, while for Fig. 1.4b the type C estimate is used. The regions are bounded from above by the condition of small mixing with the $(0, -1)$ LL, the lower bound is due to the condition of small mixing with the $(2, +1)$ LL. The thick black line shows where the maximum overlap with the Pfaffian for the bare Coulomb interaction is achieved. One can see that for small dielectric constants this line lies outside the region of validity of perturbative analysis, however for large enough κ they intersect near $U = 30$ meV.

Figures 1.5a and 1.5b show the dependence of the overlap of the exact ground state of the system with the Pfaffian on the magnetic field and the dielectric constant at $U = 50$ meV for the $(1, -1)$ LL and at $U = 30$ meV for the $(2, -1)$ LL respectively.[20] We do not show the data in the region where the perturbative anal-

[20]Due to some mistakes in calculation of the screened potential, in the original result-reporting paper [19] the overlaps for the $(1, -1)$ LL behave somewhat differently. Here we corrected the mistakes. As to the $(2, -1)$ LL, here we consider another value of U than in the paper [19], see footnote 19.

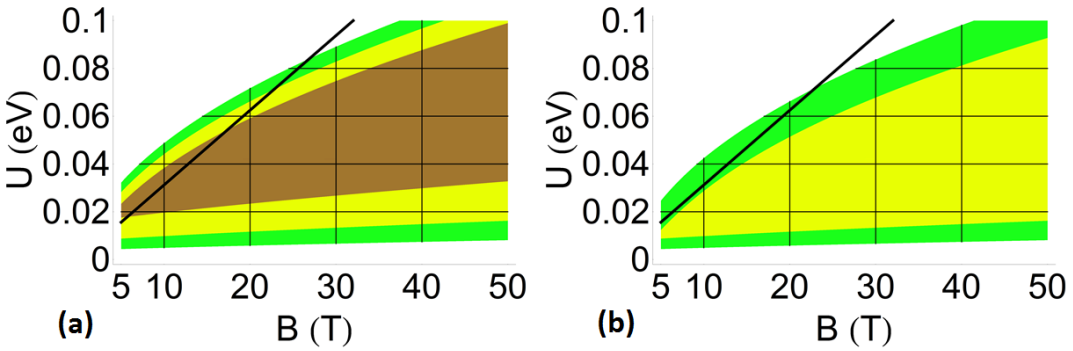

Figure 1.4: **The region of the applicability of perturbative analysis for fixed values of $\kappa = 2.5$ (brown), 5 (yellow) and 10 (green) for the $(2, -1)$ LL.** The size of the region increases with increasing κ. For (a) the typical interaction energy scale is taken to be the zeroth pseudopotential of the screened interaction potential, for (b) — of the bare Coulomb potential. At $\kappa = 2.5$ in (b) the condition of smallness of level mixing is not satisfied anywhere within the range of external parameters shown. The thick black line shows where the maximum overlap with the Moore-Read Pfaffian state for the bare Coulomb interaction is achieved.

ysis is not applicable according to type S estimate. The region of inapplicability of our theory according to the type C estimate is hatched. As one can see, for the $(1, -1)$ level, a high overlap up to 0.94 (compare with non-relativistic $n = 1$ level overlap of 0.7) can be achieved. For the $(2, -1)$ level a high overlap up to 0.92 is achieved. However, the behavior of the high-overlap (> 0.9) region is somewhat different in the two cases. For the $(1, -1)$ LL the region narrows down with decreasing of κ, and vanishes for $\kappa \approx 15$. Though, this happens in the "grey" area where our theory is still applicable according to the type S estimate, but already not applicable for according to the type C estimate, and one cannot be sure on the reliability of the data in that region. For the $(2, -1)$ LL the high-overlap region also gets narrower with decreasing κ, but we cannot say whether it continues to $\kappa \lesssim 5$ or not.

The authors of [6] found that in the $(1, -1)$ LL, high overlap is achieved in the region near $B = 10$ T. We find that the region of high overlap is situated there for large enough values of κ. However, for smaller values of $\kappa \lesssim 15$ the effect of level mixing becomes significant which makes observation of the Pfaffian state

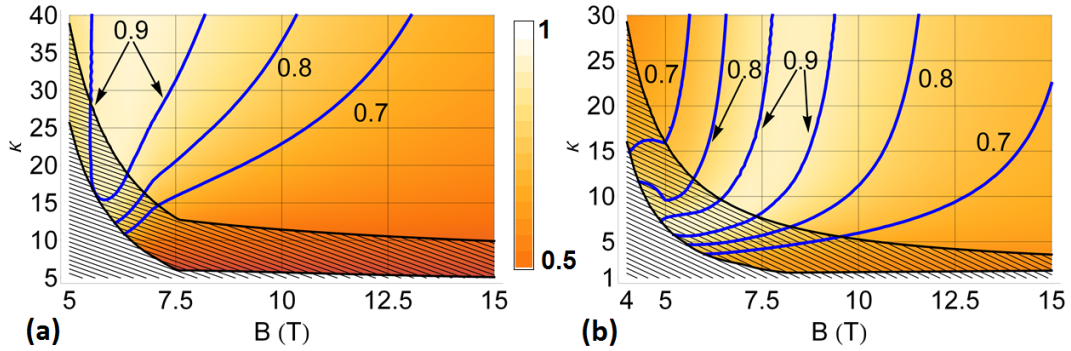

Figure 1.5: **Color plot of the overlap of the ground state with the Moore-Read Pfaffian for 12 particles as a function of the magnetic field B and the dielectric constant κ.** (a) – for the $(1,-1)$ LL at $U = 50$ meV, (b) – for the $(2,-1)$ LL at $U = 30$ meV. Contours show the lines of constant overlap. The region where perturbative analysis is not applicable according to the type C estimate is hatched. Data is not shown beyond the region where perturbative analysis is applicable according to the type S estimate.

unlikely.[21] The $(2,-1)$ LL was also considered in [6], where it was concluded that the maximal overlap with the Pfaffian on this level is less than 0.6. Our results do not support this conclusion (even for the bare Coulomb interaction).

The previous consideration shows that BLG can, in principle, be tuned into the regime of high overlap with the Pfaffian. However, one needs higher dielectric constant than the usual $\kappa \approx 2.5$ for graphene on SiO_2 or h-BN substrate. This is experimentally achievable. For example, on HfO_2 substrate [22] κ is around 12.5. This value of $\kappa = 12.5$ is enough to tune into the high-overlap region for the $(2,-1)$ LL around $B = 8$ T (with the overlap being about 0.92). The gap to the first excited state at these parameter values is around 2.2 K. With increasing magnetic field we find that the gap monotonically increases to the values of around 7.8 K at $B = 15$ T and 16 K at $B = 30$ T. At the same time the overlap decreases to around 0.6 which is still fairly large. This result, obtained for a finite number of particles, suggests that the system may still be in the same topological phase at higher magnetic fields. However, the experimental observation of the Pfaffian in

[21] It is interesting to note that recently a $\nu = 1/2$ FQHE state has been observed in suspended bilayer graphene [20] for $U \approx 0$. The parameters of the experiment lie far beyond the region of applicability of our methodology. However, the study [21], which does take into account the strong mixing between the quasidegenerate $(1,-1)$ and $(0,-1)$ LLs beyond perturbation theory, claims that the Pfaffian is a likely candidate to explain the observed $\nu = 1/2$ FQHE.

BLG in this way in the nearest future is unlikely. The main problem for observation of the fractional QHE in graphene (and BLG as well) is the too high disorder in the samples caused by the disorder in the substrate (evidently, it is impossible to observe FQHE when the typical height of the disorder potential is greater than the gap to the first excited state). For example, the FQHE with the filling factor $\nu = 1/3$ has been observed in suspended single-layer graphene [23] and in graphene on h-BN substrate [24] but not on a substrate with different lattice structure (which is the case for HfO_2 needed to achieve the high dielectric constant).

Another way to achieve higher dielectric constants is to use substrate on the both sides of BLG sheet. In that case the effective dielectric constant κ is equal to the substrate dielectric constant. Therefore, using h-BN one can get $\kappa = 5$. The region of high overlap comes quite close to this value of dielectric constant for the $(2, -1)$ LL. For example, at $U = 30$ meV, $B = 6$ T, and $\kappa = 6$ the overlap of the exact ground state and the Pfaffian state is about 0.91, with the gap to the first excited state being about 1.2 K. With increasing magnetic field the gap monotonically increases to the values of around 10 K at $B = 15$ T and 23 K at $B = 30$ T. At the same time the overlap decreases to around 0.6 which is still fairly large, which suggests that the system may still be in the same topological phase at higher magnetic fields. This, together with the fact that FQHE has been observed on h-BN substrate [24] (so one can hope to overcome the problems with disorder in this case), gives a hope that the Pfaffian state can be realized in BLG surrounded with h-BN.[22]

The reader can find some additional data on the behaviour of gaps and overlaps in Appendix A.4.

[22]Such configurations have recently started being explored experimentally from the perspective of FQHE: see Ref. [25].

1.5 Summary of the chapter

We analyze the influence of inter-Landau level transitions (vacuum polarization, virtual hopping) on the phase diagram of the FQHE states. We find that the SLLA can only be used under quite stringent conditions, and corrections to the SLLA should be taken into account. A method for taking the corrections into account by means of perturbation theory is developed. However, the region of applicability of the SLLA with our corrections is also quite restricted.

With the help of the developed method we study the possibility to observe the Moore-Read state in bilayer graphene. We find that the mentioned effects indeed lead to a substantial modification of the phase diagram. However, the external parameters needed to tune into the regime favouring the Moore-Read state are, in principle, achievable, for BLG surrounded with h-BN.

Chapter 2

Characterization of fractional quantum Hall states with the help of tunnelling current noise measurements

In this chapter a theoretical study regarding the information which can be extracted from tunnelling current noise measurements in FQHE regime is presented. The system considered in this chapter comprises two FQHE edges far apart from each other with a narrow constriction at which the edges come close to each other and interact via tunnelling of quasiparticles. In such a system the electric tunnelling current and its noise can be measured experimentally. A theoretical framework for quantitative analysis of such experiments is expounded here, together with the analysis of the data of the experiment of Ref. [1], and some proposals for the experiments.

The first section of the chapter is devoted to the analysis of the experiment of Ref. [1]. The experiment is analysed within the theoretical framework developed throughout the section.

In the second section the formulae obtained in the first one are used to show that

it is, in principle, possible to extract the tunnelling quasiparticle scaling dimension from such experiments, without knowing a specific model of the FQHE edge.

2.1 $\nu = 2/3$: counterflowing neutral mode and its properties from tunnelling current noise measurements

2.1.1 Introduction

The quasi-one-dimensional edge channels supported by fractional quantum Hall (FQH) states have for a long time attracted attention of both theorists and experimentalists. During the 1980-s models emphasizing the role of edge states for FQH transport developed into a powerful field-theoretical framework of a chiral Luttinger liquid (CLL) [26]. A very rigid mathematical structure of the latter leads to a number of non-trivial predictions such as fractionally charged quasiparticles, and excitations with anyonic or even non-abelian statistics.[1] Some of these predictions have been tested experimentally while others still pose a challenge to experimentalists.

One of the milestones in the experimental studies of the FQH effect is the recently reported observation [1] of the neutral current (a transport channel which does not carry electric charge) at the edge of the $\nu = 2/3$ FQH state. The $\nu = 2/3$ state is one of the simplest for which the CLL theory is not consistent without a neutral current. Moreover, the predicted flow direction of this current is opposite to the electrons' drift velocity [27, 28] and thus contradicts intuition based on the magnetic hydrodynamics [29].

Apart from the detection of the upstream neutral mode, the design of the

[1]The predictions related of fractional charge or unusual statistics of quasiparticles in the FQHE first appeared from different arguments, not from CLL framework. However, these properties appear extremely naturally within the CLL methodology. Since the CLL approach allows to obtain statements about these properties theoretically, one can still call them predictions of CLL.

experiment, Ref. [1], gave access to a significant amount of quantitative data characterizing the system [1, 30]. This motivated the work presented in this section where a detailed quantitative description of the experiment is developed basing on the minimal $\nu = 2/3$ edge model worked out in [27, 28] and supported by numerical simulations of small systems [31, 32]. Within the developed framework the data of [1] is analyzed in order to (a) check its consistence with the minimal $\nu = 2/3$ edge model quantitatively and (b) extract new information about $\nu = 2/3$ edge physics.

While an excellent agreement of our theory with the experimental data of Ref. [1] is found, it is worth making a remark that a number of alternative theories have been proposed recently in order to explain other experimental results such as those of Ref. [33]. These theories extend the minimal $\nu = 2/3$ edge model by introducing new physics, such as edge reconstruction [34] or bandwidth cutoffs [35], at some intermediate energy scale. Such extensions can be incorporated into our framework. However, as they contain additional unknown parameters, their comparison against experiment can only be insightful with more independent experimental data.

2.1.2 Description of the experiment [1]

Here the experiment [1], where the upstream neutral currents at the quantum Hall (QH) edge were investigated, is briefly discussed.

Figure 2.1 shows a sketch of the experimental device. The green region is the AlGaAs heterostructure with the light-green showing where the 2DEG (two-dimensional electron gas) is actually present. The sample is in the transverse magnetic field so that the filling factor is 2/3 and the corresponding quantization of the Hall conductivity is observed. Green arrows show the direction of the electrons' drift velocity which coincides with the flow direction of the charge transporting channel (charged mode). Yellow patches represent Ohmic contacts. The purple rectangular pads on top of the sample are the gates which allow one to make

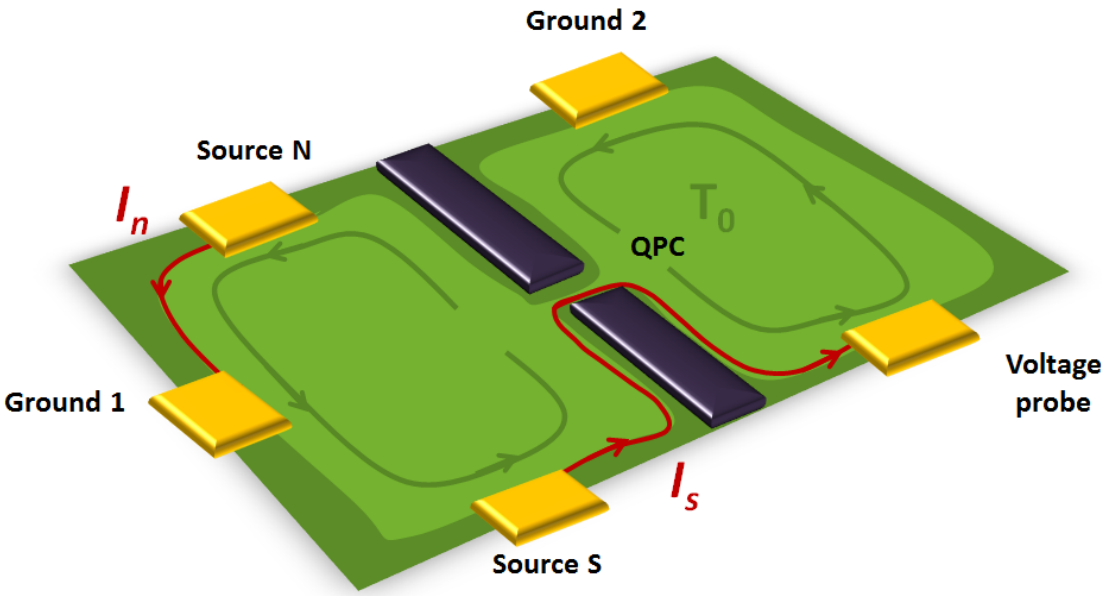

Figure 2.1: **Scheme of the experimental device**. Contacts *Ground 1* and *Ground 2* are grounded. *Source N* and *Source S* are used to inject some electric current into the system. Measurement of the electric current and its noise is performed at *Voltage probe*.

and adjust a constriction which plays the role of tunnelling junction (denoted as *QPC* in the figure). Contacts *Ground 1* and *Ground 2* are grounded. *Source N* and *Source S* are used to inject electric current into the device. Measurements of electric current and its noise are performed at *Voltage probe*.

The idea of the experiment is as follows. Suppose a current I_n is injected into *Source N*. If the edge supports only one chirality (counterclockwise) then anything injected into *Source N* will be absorbed by *Ground 1* and have no effect on *Voltage probe*. However, if we assume that there is a neutral mode flowing clockwise, information about the events in *Source N* carried by the neutral mode may reach *QPC*. In *QPC* such information may be transmitted to the opposite edge and then transported to *Voltage probe* by the charged mode. In particular, let us assume that the injection of the current I_n excites the neutral mode flowing out of *Source N* towards *QPC*. Due to the tunnelling across *QPC* of quasiparticles having both charged and neutral degrees of freedom the neutral mode excitations will be converted into the current noise at *Voltage probe*. Thus, the presence of the counterpropagating neutral mode implies that the noise observed at *Voltage*

probe should depend on the current I_n. Such a dependence was reported in [1].

The observation of the theoretically predicted upstream neutral mode is a very important qualitative result. However, experimental techniques and numerical data reported in [1] go far beyond this achievement providing a lot of implicit quantitative information about current fractionalization in Ohmic contacts, transport along the QH edges and quasiparticle tunnelling across the *QPC*. In order to effectively utilize this quantitative information one needs an analytical theory of the experiment based on the modern understanding of the FQH edge. The goal of this section is to discuss the results of [1] within such a theoretical framework.

2.1.3 Theoretical picture of the experiment

Our theoretical description of the experiment has three key ingredients: the effective theory of the quantum Hall edge, a model of the *QPC*, and phenomenological assumptions about the interaction of the Ohmic contacts with the QH edge. The former two are based on the standard theoretical framework which we briefly review in the next subsection. In this subsection we focus on the general picture of the experiment, paying particular attention to the assumptions regarding the Ohmic contacts.

Our theoretical model of the experiment is illustrated in Fig. 2.2. Each edge supports one counterclockwise charged mode and one clockwise neutral mode. The two edges approach each other in the *QPC* region where the tunnelling of the quasiparticles between the edges occurs. Our quantitative theory is developed for the case of weak quasiparticle tunnelling. The Ohmic contacts are shown as rectangles. We assume that any excitations of neutral and charged modes are fully absorbed by the Ohmic contacts they flow into. We further assume strong equilibration mechanisms at the edge so that the hydrodynamic description can be used. That is, each edge can be characterized by local point-dependent thermodynamic variables including the charged mode chemical potential $\mu^{(c)}$, the charged mode temperature T' and the neutral mode temperature T, and any other

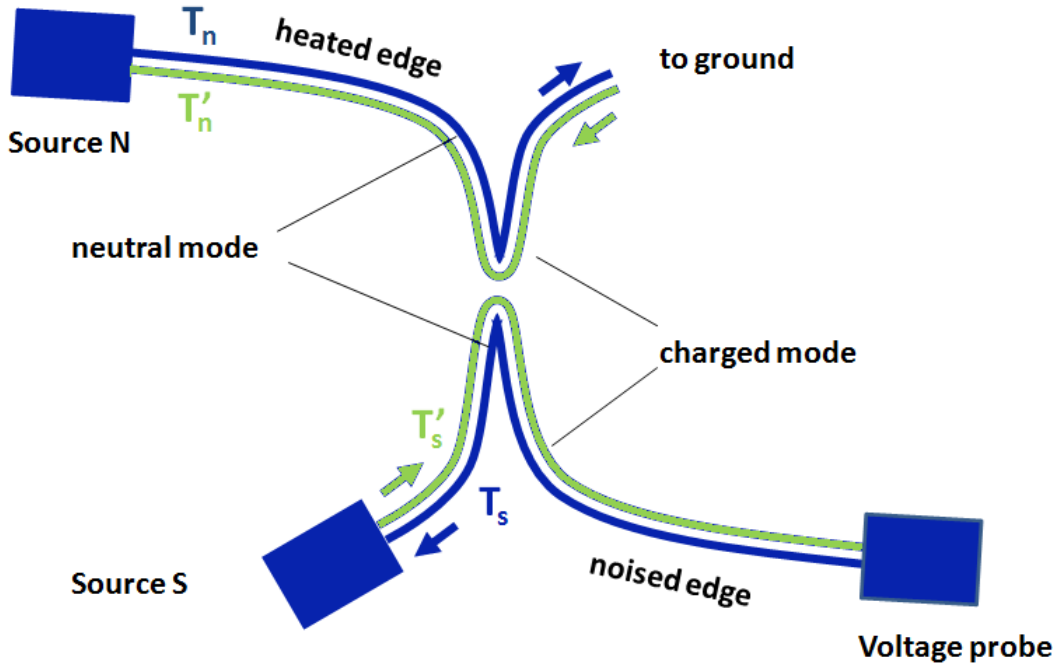

Figure 2.2: **Theoretical picture of the experiment**. The injected current I_n "heats" the neutral mode of the upper edge to the temperature T_n. Equilibration processes between the charged and the neutral modes lead to the charged mode temperature $T_n' = T_n$. Both modes at the lower edge have the temperature of the environment: $T_s' = T_s = T_0$. Tunnelling of the quasiparticles at the constriction induces extra noise in the charged mode of the lower edge which is detected at the *Voltage probe*. Injection of the current I_s only changes the chemical potential of the charged mode of the lower edge.

thermodynamic variables arising due to the existence of extra conserved quantities. We assume that in the absence of currents ($I_n = 0$ and $I_s = 0$) the edges are in equilibrium with the environment so that all modes' temperatures are equal to the base temperature T_0 and the chemical potentials are equal to zero. Away from this state the temperatures and chemical potentials are unknown functions of I_n and I_s, and other thermodynamic variables are assumed to be unaffected by the injection of currents I_n, I_s. The functions $\mu^{(c)}(I_n, I_s)$, $T(I_n, I_s)$, $T'(I_n, I_s)$ for each edge are defined by the interaction of the Ohmic contact with the edge, however no predictive theoretical model of such interaction is known today. As we show, these functions can be inferred from the experimental data under some plausible phenomenological assumptions.

We assume that there is a strong heat exchange between the modes at each

edge. In this approximation the local temperatures of the two modes coincide at each point along the edge: $T_n = T'_n$, $T_s = T'_s$. Moreover, following [1] we assume that the lower edge temperature is equal to the base temperature ($T_s = T'_s = T_0$); that is, the electric current I_s injected by the Ohmic contact *Source S* does not induce any non-equilibrium noise to the lower edge charged mode.

2.1.4 Formalism of the edge field theory

In this subsection we give a brief overview of the CLL formalism [26, 36, 37], which is believed to provide the effective theoretical description of a fractional QH edge. We then focus on a particular edge model relevant to the experiment [1]. We conclude this subsection by a discussion of the model Hamiltonian describing the tunnelling of quasiparticles between the QH edges.

2.1.4.1 General formalism[2]

Abelian QH edge theories are usually formulated in terms of bosonic fields $\varphi_i(x,t)$, where t is time and x is the spatial coordinate along the edge. Each field φ_i represents an edge mode. Suppose that we have N edge modes and correspondingly N fields φ_i with $i = 1, ..., N$. Then the dynamics of the edge is described by the effective action [38][3]

$$S = \frac{1}{4\pi} \int dxdt \sum_i \Big(-\chi_i D_x\varphi_i D_t\varphi_i - v_i (D_x\varphi_i)^2 + q_i \varepsilon^{\mu\nu} a_\mu \partial_\nu \varphi_i \Big), \tag{2.1}$$

where $v_i \in \mathbb{R}_+$ are the propagation velocities, $\chi_i = \pm 1$ represent chiralities of the modes (plus for the clockwise and minus for the counterclockwise direction), and $a_\mu(x,t)$ is the electromagnetic field potential at the edge. Covariant derivatives are defined as $D_\mu\varphi_i = \partial_\mu\varphi_i - \chi_i q_i a_\mu$. The coupling constants q_i provide information on how the electric charge is distributed between the modes. The symbol $\varepsilon^{\mu\nu}$

[2]Here and in what follows we put $e = \hbar = k_B = 1$ unless the opposite is stated explicitly. Here e is the elementary charge, $\hbar$ is the Planck constant, k_B is the Boltzmann constant.

[3]In fact, the action (2.1) has to be used with care because its chiral nature imposes implicit constraints on the external perturbation a_μ. This problem does not emerge in Hamiltonian formalism used in [36].

denotes the fully antisymmetric tensor with μ, ν taking values t and x (or 0 and 1 respectively) and $\varepsilon^{tx} = \varepsilon^{01} = 1$.

Conservation of total electric current in the whole volume of a 2D sample leads to the condition [36, 37]

$$\sum_i \chi_i q_i^2 = \nu. \tag{2.2}$$

The electric current at the edge is

$$J^\mu = \frac{\delta S}{\delta a_\mu} = \frac{1}{2\pi} \sum_i q_i \varepsilon^{\mu\nu} D_\nu \varphi_i + \frac{\nu}{4\pi} \varepsilon^{\mu\nu} a_\nu. \tag{2.3}$$

In the presence of the electric field it is not conserved:

$$\partial_\mu J^\mu = -\frac{\nu}{4\pi} \varepsilon^{\mu\nu} \partial_\mu a_\nu \neq 0, \tag{2.4}$$

which is a manifestation of the inflow of the Hall current from the bulk.

In the absence of the electric field $a_\mu(x,t) = 0$ the current is conserved and has the form

$$J^\mu = \frac{1}{2\pi} \sum_i q_i \varepsilon^{\mu\nu} \partial_\nu \varphi_i, \qquad \partial_\mu J^\mu = 0 \tag{2.5}$$

In the rest of this subsection we assume that $a_\mu(x,t) = 0$.

Further to the electric current one can also define neutral currents

$$J^\mu_{\text{n}} = \frac{1}{2\pi} \sum_i p_i \varepsilon^{\mu\nu} \partial_\nu \varphi_i, \qquad \partial_\mu J^\mu_{\text{n}} = 0, \tag{2.6}$$

with vector $\mathbf{p} = (p_1, ..., p_N)$ being linearly independent of vector $\mathbf{q} = (q_1, ..., q_N)$.[4]

The quantized fields φ_i can be presented as follows

$$\varphi_i(x,t) = \varphi_i^0 + \frac{2\pi}{L} \pi_i^0 X_i + i \sum_{n=1}^{\infty} \sqrt{\frac{2\pi}{Lk}} \Big(a_i(k) \exp(-ikX_i) - a_i^\dagger(k) \exp(ikX_i) \Big) \tag{2.7}$$

[4]The conserved neutral currents can give rise to neutral modes' chemical potentials $\mu^{(n)}$ — thermodynamic quantities dual to the neutral charges. In the main text, as it was pointed out in the previous subsection, we assume that these neutral chemical potentials are not involved in the experiment we are going to analyze. However, for the sake of generality we include them in formulae in Appendices B.1, B.8.

where $X_i = -\chi_i x + v_i t$, $k = 2\pi n/L$, $n \in \mathbb{N}$; $L \to \infty$ is the system size, $a_i(k)$ and $a_i^\dagger(k)$ are the annihilation and the creation operators respectively, φ_0 and π_0 are the zero modes:

$$[a_i(k), a_j^\dagger(k')] = \delta_{ij}\delta_{kk'}, \qquad [\pi_i^0, \varphi_i^0] = -i\delta_{ij}. \tag{2.8}$$

The fields φ_i obey the commutation relation of chiral bosons:

$$[\varphi_i(x,t), \varphi_j(x',t')] = -i\pi \mathrm{sgn}(X_i - X_i')\, \delta_{ij}. \tag{2.9}$$

The edge supports quasiparticles of the form

$$V_{\mathbf{g}}(x,t) = \left(\frac{L}{2\pi}\right)^{-\sum_i g_i^2/2} : \exp\left(i\sum_i g_i \varphi_i(x,t)\right) :, \tag{2.10}$$

which are important for the processes of tunnelling at the *QPC*. The notation : ... : stands for the normal ordering, and $\mathbf{g} = (g_1, ..., g_N)$, $g_i \in \mathbb{R}$ are the quasiparticle quantum numbers.

Among the quasiparticle fields there has to be a field representing an electron which is the fundamental constituent particle:

$$\psi(x,t) = \left(\frac{L}{2\pi}\right)^{-\sum_i a_i^2/2} : \exp\left(i\sum_i a_i \varphi_i(x,t)\right) :, \tag{2.11}$$

$a_i \in \mathbb{R}$. Minimal models of the QH states of Jain series $\nu = N/(2N \pm 1)$ have N electron operators each representing a composite fermion Landau level:

$$\psi_\alpha(x,t) = \left(\frac{L}{2\pi}\right)^{-\sum_i e_{\alpha i}^2/2} : \exp\left(i\sum_i e_{\alpha i} \varphi_i(x,t)\right) :, \qquad e_{\alpha i} \in \mathbb{R}. \tag{2.12}$$

The electron fields have to satisfy the following constraints:

$$\begin{aligned} &\{\psi_\alpha(x,t),\psi_\alpha(x',t)\}=0,\\ &\psi_\alpha(x,t)\psi_\beta(x',t)\pm\psi_\beta(x',t)\psi_\alpha(x,t)=0,\quad \alpha\neq\beta,\\ &[J^0(x,t),\psi_\alpha(x',t)]=\delta(x-x')\psi_\alpha(x,t). \end{aligned} \tag{2.13}$$

where J^0 is the charge density operator defined in Eq. (2.5), $\{...\}$ denotes the anti-commutator, and a plus or minus sign in the second equation can be chosen independently for each pair (α,β); $\alpha,\beta=1,...,N$.

For the parameters $e_{\alpha i}$ in Eq. (2.12) these constraints imply

$$\mathbf{e}_\alpha\cdot\mathbf{e}_\alpha\in 2\mathbb{Z}+1,\quad \mathbf{e}_\alpha\cdot\mathbf{e}_\beta\in\mathbb{Z},\quad \mathbf{q}\cdot\mathbf{e}_\alpha=-1 \tag{2.14}$$

where we defined $\mathbf{e}_\alpha=(e_{\alpha 1},...,e_{\alpha N})$ and $\mathbf{q}=(q_1,...,q_N)$ with q_i being the coupling constants from the action (2.1), and the operation $\mathbf{A}\cdot\mathbf{B}\equiv\sum_{i=1}^N\chi_i A_i B_i$.

Equations (2.14) have many inequivalent solutions each defining a topological QH class. It is convenient to parametrize these classes with the help of the K-matrix:

$$K_{\alpha\beta}=\mathbf{e}_\alpha\cdot\mathbf{e}_\beta. \tag{2.15}$$

Consider now a QH fluid corresponding to a particular solution $\{\mathbf{e}_1,...,\mathbf{e}_N\}$ of Eqs. (2.14). The spectrum of the quasiparticles (2.10) present in the model is determined from the requirement of mutual locality with all the electron operators:

$$\psi_\alpha(x,t)V_g(x',t)+sV_g(x',t)\psi_\alpha(x,t)=0, \tag{2.16}$$

where s is either $+1$ or -1 depending on the particular quasiparticles.

This leads to the following restrictions on the parameters g_i in Eq. (2.10):

$$\mathbf{g}\cdot\mathbf{e}_\alpha=n_\alpha\in\mathbb{Z},\quad \alpha=1,...,N, \tag{2.17}$$

where $\mathbf{g} = (g_1, ..., g_N)$. The set of numbers n_α completely defines the properties of a quasiparticle operator.

For the following considerations two quantum numbers of the quasiparticle operator (2.10) are of particular importance: the electric charge Q and the scaling dimension δ. They are given by

$$Q(\mathbf{n}) = \mathbf{q} \cdot \mathbf{g} = \sum_{\alpha\beta} K^{-1}_{\alpha\beta} n_\beta, \tag{2.18}$$

$$\delta(\mathbf{n}) = \frac{1}{2} \sum_i g_i^2. \tag{2.19}$$

2.1.4.2 The minimal model of the $\nu = 2/3$ QH edge

Here we use the general principles discussed above to obtain the minimal model of the $\nu = 2/3$ QH edge. This model emerges from different semi-phenomenological theoretical approaches to the QH edge [39, 40] and is the most likely candidate to describe this fraction [32].

First, we note that it is impossible to satisfy the constraints (2.2) and (2.14) assuming that $N = 1$. For $N = 2$ we choose the chiralities

$$\chi_1 = 1, \quad \chi_2 = -1 \tag{2.20}$$

and the charge vector[5]

$$\mathbf{q} = (\sqrt{2/3}, 0). \tag{2.21}$$

Then equations (2.14) lead to an infinite one-parameter family of solutions:

$$\mathbf{e}_1 = \left(-\sqrt{\frac{3}{2}}, \sqrt{\frac{3}{2} + 2m + 1} \right), \tag{2.22}$$

$$\mathbf{e}_2 = \left(-\sqrt{\frac{3}{2}}, -\sqrt{\frac{3}{2} + 2m + 1} \right), \tag{2.23}$$

[5]Note that there exists an infinite freedom in the choice of the vector $\mathbf{q}$ giving rise to infinitely many physically inequivalent theories. However, as it was shown in [27, 28] by perturbative RG analysis, the choice (2.21) leads to a theory stable against disorder scattering.

where $m = -1, 0, 1, 2, ...$

The electron operators have the smallest scaling dimension for $m = -1$, which gives

$$\mathbf{e}_{1,2} = \left(-\sqrt{\frac{3}{2}}, \pm\sqrt{\frac{1}{2}} \right) \tag{2.24}$$

and the K-matrix

$$K = \begin{pmatrix} 1 & 2 \\ 2 & 1 \end{pmatrix}. \tag{2.25}$$

This defines the minimal model of the $\nu = 2/3$ QH edge.

The quasiparticle spectrum of the model is defined by Eq. (2.17). The parameters of the three excitations which are most relevant for tunnelling across the *QPC* are given in Table 2.1.

Table 2.1: Parameters of the most relevant excitations in the minimal model of the $\nu = 2/3$ QH edge (see Eqs. (2.10), (2.17), (2.18), and (2.19)).

Type	g_1	g_2	Q	δ
1	$\sqrt{1/6}$	$\sqrt{1/2}$	1/3	1/3
2	$\sqrt{1/6}$	$-\sqrt{1/2}$	1/3	1/3
3	$\sqrt{2/3}$	0	2/3	1/3

We find it convenient to define the neutral current (2.6) with

$$\mathbf{p} = (0, -1). \tag{2.26}$$

2.1.4.3 Tunnelling of quasiparticles across the *QPC*

Wherever the two QH edges approach each other at a distance on the order of the magnetic length processes of quasiparticle exchange between the edges are possible. It is widely accepted [36, 41, 42] that such processes can be described by adding the following term to the Hamiltonian:

$$H_T = \sum_{\mathbf{g}} \eta_{\mathbf{g}} V_{\mathbf{g}}^{(u)\dagger}(0,t) V_{\mathbf{g}}^{(l)}(0,t) + \text{h.c.}, \tag{2.27}$$

where the superscripts $(u), (l)$ label quantities relating to the upper and the lower edge respectively; for simplicity we assume that tunnelling occurs at the origin. In the case of weak tunnelling across the bulk of the QH state the sum runs over all quasiparticles in the model. However, at small energies quasiparticles with the smallest scaling dimension $\delta(\mathbf{g})$ have the largest tunnelling amplitude $\eta_{\mathbf{g}}$, thus giving the most important contribution.

2.1.5 Calculation of observable quantities

In this subsection we derive analytical expressions for two observable quantities as functions of the experimentally variable parameters. These quantities are the tunnelling rate, that is the ratio of the current tunnelling across the *QPC* to the *Source S* current I_s, and the excess noise in the *Voltage probe*, which is the noise in the *Voltage probe* in the presence of currents I_n, I_s less the equilibrium noise at $I_n = I_s = 0$. We further demonstrate that it is advantageous to consider the ratio of these quantities rather than each separate one. This way the influence of non-universal physics of the tunnelling contact can be reduced.

Our expressions for the excess noise and the tunnelling rate, presented in Eqs. (2.40)-(2.46), are in full agreement with Eqs. (10) and (11) of Ref. [43].

2.1.5.1 Tunnelling rate

As it was mentioned in the previous subsection, the most important contribution to the tunnelling processes is due to the most relevant excitations. Such excitations are listed in Table 2.1, and we restrict our considerations to these excitations only. To this end we introduce the following notation $\psi_i(x,t) = V_{\mathbf{g}_i}(x,t)$ where $\mathbf{g}_i$, $i = 1,2,3$ are the three most relevant quasiparticle vectors given in Table 2.1.

The tunnelling Hamiltonian can then be written as

$$H_T = \sum_{i=1}^{3} \eta_i A_i(t) + \eta_i^* A_i^\dagger(t), \tag{2.28}$$

$$A_i(t) = \psi_i^{(u)\dagger}(0,t)\psi_i^{(l)}(0,t) \tag{2.29}$$

where the superscripts $(u), (l)$ label quantities relating to the upper and the lower edge respectively and η_i are unknown complex phenomenological parameters.

We calculate the tunnelling current within the second order perturbation theory in the tunnelling Hamiltonian. The detailed derivation can be found in Appendix B.2. The resulting tunnelling rate is given by the Kubo formula:

$$r = \left|\frac{I_T}{I_s}\right| = \left|\frac{1}{I_s}\sum_i |\eta_i|^2 Q_i \int_{-\infty}^{\infty} d\tau \left\langle \left[A_i(\tau), A_i^\dagger(0)\right]\right\rangle\right|, \tag{2.30}$$

where I_T is the tunnelling current and I_s is the current originating from *Source S*. Note, that apart from r paper [1] also uses $t = 1 - r$.

2.1.5.2 Excess noise

Noise spectral density of the electric current flowing into the *Voltage probe* (see Fig. 2.2) can be calculated as the Fourier transform of the two-point correlation function of the current operator I,

$$S(\omega) = \int_{-\infty}^{\infty} d\tau \exp\big(i\omega\tau\big)\frac{1}{2}\Big\langle\Big\{\Delta I(0), \Delta I(\tau)\Big\}\Big\rangle, \tag{2.31}$$

where $\{\dots\}$ denotes the anti-commutator, and $\Delta I = I - \langle I\rangle$.[6]

It is convenient to separate the operator I of the full current flowing to the *Voltage probe* into $I_0 + I_T$ with $I_0 = J^{\mu(l)}(x = -0, t = 0)|_{\mu=1=x}$ being the spatial component of the operator $J^\mu(x,t)$ defined in Eq. (2.5) which represents the electric

[6]We must note here that there are two conventions concerning the definition of the noise spectral density. While some authors (see, e.g., [7]) use the same definition as we do, others (see, e.g., [44], [1]) adopt the definition which is twice as large as ours. Thus our results must be multiplied by 2 in order to be compared with the data of [1].

current flowing along the lower edge just before the tunnelling point, and I_T being the tunnelling current operator. Then the noise can be represented as follows:

$$S(\omega) = S_{00}(\omega) + S_{0T}(\omega) + S_{0T}(-\omega) + S_{TT}(\omega), \tag{2.32}$$

$$S_{ab}(\omega) = \int_{-\infty}^{\infty} d\tau \exp\big(i\omega\tau\big)\frac{1}{2}\Big\langle\Big\{\Delta I_a(0), \Delta I_b(\tau)\Big\}\Big\rangle, \tag{2.33}$$

with $\Delta I_a = I_a - \langle I_a\rangle$, indices a, b take values 0 and T.

We are interested in the low-frequency component measured in the experiment. To a good approximation this can be replaced by the zero-frequency component $S(\omega = 0)$. Within the second order perturbation theory we find

$$S_{00}(0) = \frac{\nu}{2\pi}T_s, \tag{2.34}$$

$$S_{TT}(0) = \sum_i |\eta_i|^2 Q_i^2 \int_{-\infty}^{\infty} d\tau\big\langle\{A_i(0), A_i^\dagger(\tau)\}\big\rangle, \tag{2.35}$$

$$S_{0T}(0) = \frac{1}{2}\sum_i |\eta_i|^2 Q_i \int_{-\infty}^{\infty} d\tau \int_{-\infty}^{\infty} d\tau'\big\langle\{\Delta I_0(0), [A_i(\tau'), A_i^\dagger(\tau)]\}\big\rangle. \tag{2.36}$$

We remind the reader that T_s is the lower edge temperature in the neighbourhood of the *QPC*. These formulae are derived in Appendix B.4.

The contribution S_{00} is the Johnson-Nyquist noise of the lower edge. If we restore e, $\hbar$, and k_B, we see that $S_{00}(0) = k_B T_s/R$, $R = 2\pi\hbar/(\nu e^2) = h/(\nu e^2)$. Since the *Voltage probe* contact not only absorbs the lower edge charged mode but also emits another charged mode which flows to the right of it, the actual Nyquist noise measured in the contact will be $S_{JN}(0) = 2k_B T_s/R$, in agreement with general theory of Johnson-Nyquist noise. The factor of 2 difference from the Nyquist noise expression used in [1] is due to the noise spectral density definition as discussed in footnote 6.

Following [1] we define the excess noise

$$\tilde{S}(0) = S(0) - S_{\rm eq}(0), \tag{2.37}$$

where $S_{\rm eq}$ is the equilibrium noise spectral density (i.e. the noise when $I_s = 0$ and $I_n = 0$, meaning that the edge temperatures are equal to the base temperature: $T_s = T_n = T_0$). It turns out that $S_{\rm eq}(0) = S_{00}(0)$ resulting in

$$\tilde{S}(0) = 2S_{0T}(0) + S_{TT}(0). \tag{2.38}$$

This fact is proven in Appendix B.7 using the explicit formulae for $S_{0T}(0)$, $S_{TT}(0)$ obtained in Appendices B.5 and B.6.

2.1.5.3 Noise to tunnelling rate ratio[7]

Expressions (2.30), (2.35), and (2.36) depend on the tunnelling amplitudes η_i. It is well known (see e.g. [45, 46, 47] and references therein) that the tunnelling amplitudes η_i in electrostatically confined QPCs strongly depend on the applied bias voltage in a non-universal way, probably due to charging effects. Therefore one would like to exclude this dependence from the quantities used for comparison with experiment.

Consider the ratio of the excess noise to the tunnelling rate:

$$X = \frac{\tilde{S}(0)}{r} = eI_s \frac{\sum_{i=1}^{3} \theta_i F_i}{\sum_{i=1}^{3} \theta_i G_i} = eI_s \frac{F_1 + \theta F_3}{G_1 + \theta G_3}, \tag{2.39}$$

where $\theta_i = |\eta_i|^2 (v_c/v_n)^{2((\mathbf{g}_i)_2)^2}$, $\theta = \theta_3/(\theta_1 + \theta_2)$, v_c and v_n are the propagation velocities of the charged and the neutral mode respectively, and e is the elementary charge. The number $(\mathbf{g}_i)_2$ is presented in the column g_2 of Table 2.1 for each of the three excitations enumerated by i. Functions F_i and G_i (see Appendices B.3, B.5, B.6 and B.8) represent contribution of different excitations to the excess noise and tunnelling current respectively. In particular, the excess noise is given by

$$\tilde{S}(0) = \frac{4e^2(\pi T_s)^{4\delta-1}}{\hbar^{4\delta+1} v_c^{4\delta}} \sum_i \theta_i F_i, \tag{2.40}$$

[7] In this paragraph we restore the elementary charge e, the Planck constant $\hbar = h/2\pi$, and the Boltzmann constant k_B in order to simplify use of our formulae for comparison with experimental data.

and the tunnelling rate is equal to

$$r = \frac{4e(\pi T_s)^{4\delta-1}}{I_s \hbar^{4\delta+1} v_c^{4\delta}} \sum_i \theta_i G_i. \tag{2.41}$$

The explicit form of these functions is presented below. Note that $F_1 = F_2$ and $G_1 = G_2$.

$$G_i = \sin 2\pi\delta \int_0^\infty dt \frac{Q_i \lambda^{2\delta} \sin Q_i j_s t}{(\sinh t)^{2\delta} (\sinh \lambda t)^{2\delta}} \tag{2.42}$$

$$F_i = F_i^{TT} \cos 2\pi\delta - \frac{2}{\pi} F_i^{0T} \sin 2\pi\delta, \tag{2.43}$$

$$F_i^{TT} = Q_i^2 \times \lim_{\varepsilon \to +0} \left(\frac{\varepsilon^{1-4\delta}}{1-4\delta} + \int_\varepsilon^\infty dt \frac{\lambda^{2\delta} \cos Q_i j_s t}{(\sinh t)^{2\delta} (\sinh \lambda t)^{2\delta}} \right) \tag{2.44}$$

$$F_i^{0T} = \int_0^\infty dt \frac{Q_i^2 \lambda^{2\delta} t \cos Q_i j_s t}{(\sinh t)^{2\delta} (\sinh \lambda t)^{2\delta}} \tag{2.45}$$

$$j_s = \frac{I_s}{I_0}, \quad I_0 = \nu \frac{e}{h} \pi k_B T_s = \nu \frac{e}{h} \pi k_B T_0, \tag{2.46}$$

where $\lambda = T_n/T_s$, T_n is the local upper edge temperature at the QPC, $T_s = T_0$ is the local lower edge temperature at the QPC, e is the elementary charge, $h = 2\pi\hbar$ is the Planck constant, k_B is the Boltzmann constant, $\nu = 2/3$ is the filling factor, and the scaling dimension δ and the quasiparticle charges in the units of the elementary charge Q_i can be found in Table 2.1.

Remarks on non-universality in the noise to tunnelling rate ratio. It is easy to see that if any one quasiparticle dominates tunnelling (for example, if $\theta \to \infty$) then the unwanted non-universal dependence of the tunnelling amplitudes on the applied bias voltage does not enter the expression (2.39). If we assume that the SU(2) symmetry of the edge [27, 28] is for some reason preserved at the tunnelling contact so that $|\eta_1|^2 = |\eta_2|^2 = |\eta_3|^2$, then again the non-universal behavior of the tunnelling amplitudes does not enter the expression X; moreover, in this case finding θ allows us to determine the v_c/v_n ratio. In general, though, θ

may exhibit some non-universal behavior. Anticipating results, we can say that, surprisingly, θ does not seem to exhibit any strong dependence on I_s or I_n.

For the following considerations we also give the large-I_s asymptotic behavior of the noise to tunnelling rate ratio (2.39) which we derive using Eqs. (2.42)-(2.46):

$$X_{\lambda,\theta}(I_s)|_{I_s\to\infty} = Q_1 e|I_s|\frac{1+\theta(I_n,I_s)(Q_3/Q_1)^{4\delta+1}}{1+\theta(I_n,I_s)(Q_3/Q_1)^{4\delta}} = \frac{e}{3}|I_s|\frac{1+2^{7/3}\theta(I_n,I_s)}{1+2^{4/3}\theta(I_n,I_s)}. \quad (2.47)$$

This asymptotic expression can give the reader an idea as to the effect introduced by the non-universal function $\theta(I_n, I_s)$. One can see, for example, that the gradient of the asymptote increases by a factor of 2 as θ increases from zero to infinity.

2.1.6 Comparison with the experiment

In this subsection we compare our analytical results with the experimental data.

The following data are available from the paper [1]: the transmission rate $t = 1-r$ dependence on the currents I_n and I_s (Fig. 3(a) of [1]), the dependence of the excess noise at zero frequency on the currents I_n and I_s (Fig. 3(a) of [1]) and the dependence of the excess noise at zero frequency on the current I_n for $I_s = 0$ (Fig. 2 of [1]).

It is a well-known problem (see, e.g., [45, 46, 47] and references therein) that the dependence of the transmission rate t on the current I_s does not have the form predicted by the minimal model of tunnelling defined in Eqs. (2.28), (2.29). A possible explanation is the non-universal dependence of the tunnelling amplitudes η_i on I_s due to electrostatic effects. As discussed in the previous subsection this problem can be avoided in simple cases by considering the ratio of the excess noise to the tunnelling rate $r = 1 - t$. However, in the present case a certain degree of non-universality remains due to the non-universal function $\theta(I_n, I_s)$. The theoretical expression for the noise to tunnelling rate ratio $X_{\lambda,\theta}(I_s)$ is given by Eq. (2.39), where $\lambda = T_n/T_s$ is the ratio of the two edges' temperatures. Neither

θ, nor λ can be calculated theoretically and we will deduce them from fits of the experimental data. We assume that λ depends on I_n but not on I_s; we also assume that the non-universal behaviour of the tunnelling amplitudes does not lead to any significant dependence of θ on the currents I_n, I_s. While the former assumption is physically plausible in the weak tunnelling regime, the latter one is motivated by our intention to reduce the number of fitting parameters as much as we can.

In Fig. 2.3 the results of fitting $X_{\lambda,\theta}(I_s)$ to the experimental data taken from Fig. 3(a) of [1] are shown. Optimal fits are found for each set of points corresponding to a given value of I_n with θ and λ being fitting parameters. The corresponding values and standard deviations of fitting parameters are shown in Table 2.2. For $I_n = 0$ we have set $\lambda = 1$ by definition.

Table 2.2: Results of fitting the experimental points from Fig. 3(a) of [1] by the function $X_{\lambda,\theta}(I_s)$ defined in Eq. (2.39). Fitting parameters λ and θ are defined independently for each value of the current I_n. $\Delta\lambda$ and $\Delta\theta$ are standard deviations of λ and θ respectively.

#	I_n (nA)	λ	$\Delta\lambda$	θ	$\Delta\theta$
1	0.0	1.00	–	0.53	0.04
2	0.5	4.48	0.19	0.44	0.03
3	1.0	6.16	0.15	0.35	0.02
4	1.5	7.32	0.17	0.30	0.02
5	2.0	8.65	0.13	0.36	0.03

As one can see from the Table 2.2, the values of θ do not vary significantly. Thus we repeat the fitting procedure with θ equal to the mean of the five values and λ being the only fitting parameter. The resulting fits and values of λ are presented in Fig. 2.4 and Table 2.3. As one can see the fits remain good, thus we cannot reliably find the extent of deviation of θ from a constant value with the available experimental data.

Table 2.3 gives us some data on the dependence of $T_n = \lambda T_s = \lambda T_0$ on the current I_n. We further investigate this by fitting it with the following function:

$$T_n = T_0 \left(1 + C \ |I_n|^a \right), \tag{2.48}$$

Table 2.3: Results of fitting the experimental points from Fig. 3(a) of [1] by the function $X_{\lambda,\theta}(I_s)$ defined in Eq. (2.39). Fitting parameter λ is defined independently for each value of the current I_n for fixed $\theta = \theta_{\rm mean} = \sum_i \theta_i/5 = 0.39$. $\Delta\lambda$ is the standard deviation of λ.

#	I_n (nA)	λ	$\Delta\lambda$
1	0.0	1.00	–
2	0.5	4.62	0.18
3	1.0	5.98	0.14
4	1.5	6.99	0.17
5	2.0	8.55	0.11

where C and a are fitting parameters. The resulting fit is shown in Fig. 2.5. The corresponding values of fitting parameters are $a = 0.54(5)$, $C = 5.05(13)\,\mathrm{nA}^{-a}$. This disagrees with the claim of Ref. [43] that the experimental data are consistent with a linear T_n dependence on I_n. We cannot analyze the source of this discrepancy because Ref. [43] does not contain sufficient detail as to how the comparison with the experiment was done.

Using the phenomenological dependence (2.48) it is possible to predict the noise to tunnelling rate ratio at any I_s, I_n without any further fitting procedures (we still take $\theta = \theta_{\rm mean} = 0.39$). So we can test the formula (2.48) by comparing the theoretical prediction of $X_{\lambda,\theta}(I_s)$ to another data set. We take the experimental data for the excess noise $\tilde{S}(0)$ dependence on I_n for $I_s = 0$ from Fig. 2 of the paper [1] for $t = 1 - r = 80\%$. The resulting comparison of the noise to tunnelling rate ratio X is shown in Fig. 2.6. An excellent agreement of the theoretical curve and the experimental points gives an independent confirmation of the result (2.48).

2.1.7 Discussion

Here we discuss the results of the comparison of theoretical predictions with the experimental data, and emphasize some important aspects of our analysis.

The good quality of the fits shown in Fig. 2.4 suggests that the minimal model of the $\nu = 2/3$ quantum Hall edge is consistent with the experimental data. Note, that the existence of good fits is not trivial because of the following reasons. The

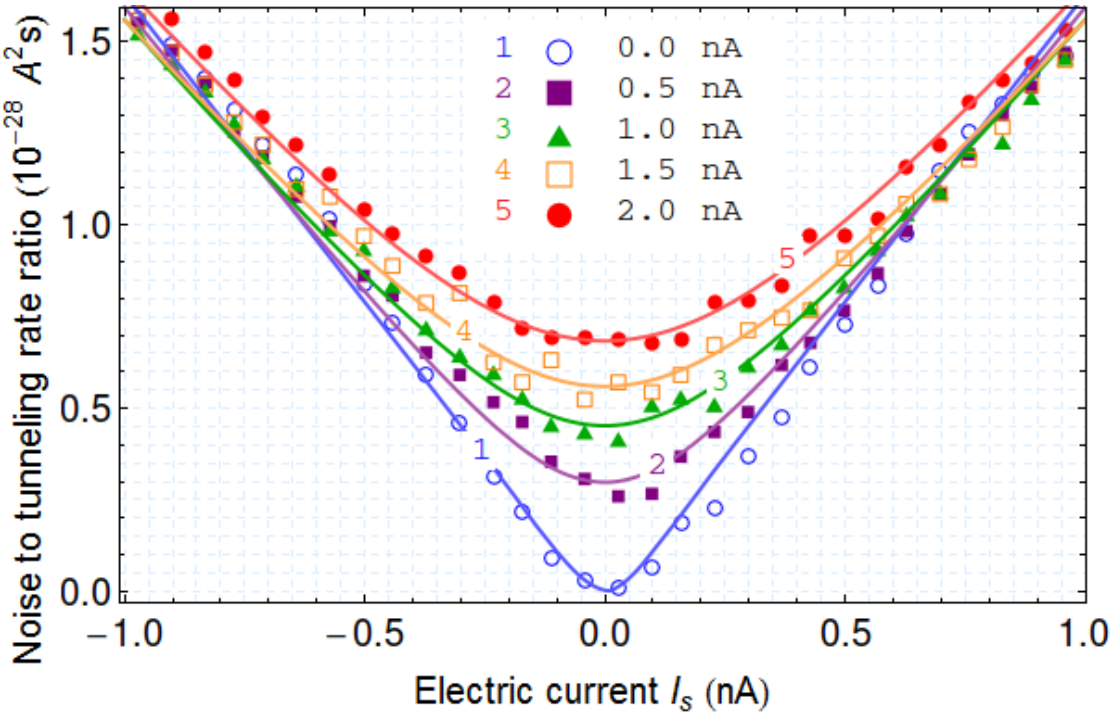

Figure 2.3: **Excess noise to tunnelling rate ratio as a function of the current I_s.** Shown are experimental points and fits thereof by theoretical curves for different values of the current I_n. The legend shows the I_n value in nA for each curve (plot symbol). Fitting parameters λ and θ are defined independently for each value of I_n.

number of fitting parameters is small; namely, two fitting parameters are used to get Fig. 2.3, only one is used for Fig. 2.4 and no fitting parameters are involved in obtaining Fig. 2.6. Moreover, our theory imposes strong constraints on the shape of the function $X_{\lambda,\theta}(I_s)$ in the whole region of parameters λ, θ. For example, as can be seen from Eq. (2.47), the gradient of the large I_s asymptote of the curve $X_{\lambda,\theta}(I_s)$ varies between $e/3$ and $2e/3$ as θ increases from zero to infinity. The fact that the experimental curve lies between these bounds is non-trivial.

The fact that the gradient of the large I_s asymptote of the curve $X_{\lambda,\theta}(I_s)$ does not coincide with the limiting values of $e/3$ and $2e/3$ provides an indirect confirmation of the presence of more than one quasiparticle species taking part in tunnelling. Indeed, in the case of a single quasiparticle species of charge Q, the asymptote gradient would equal Q. From considerations similar to the flux insertion argument [3, Section 7.5] one can deduce that the natural $\nu = 2/3$ fractional charges are integer multiples of $e/3$. Interpreting the asymptotic behavior of the

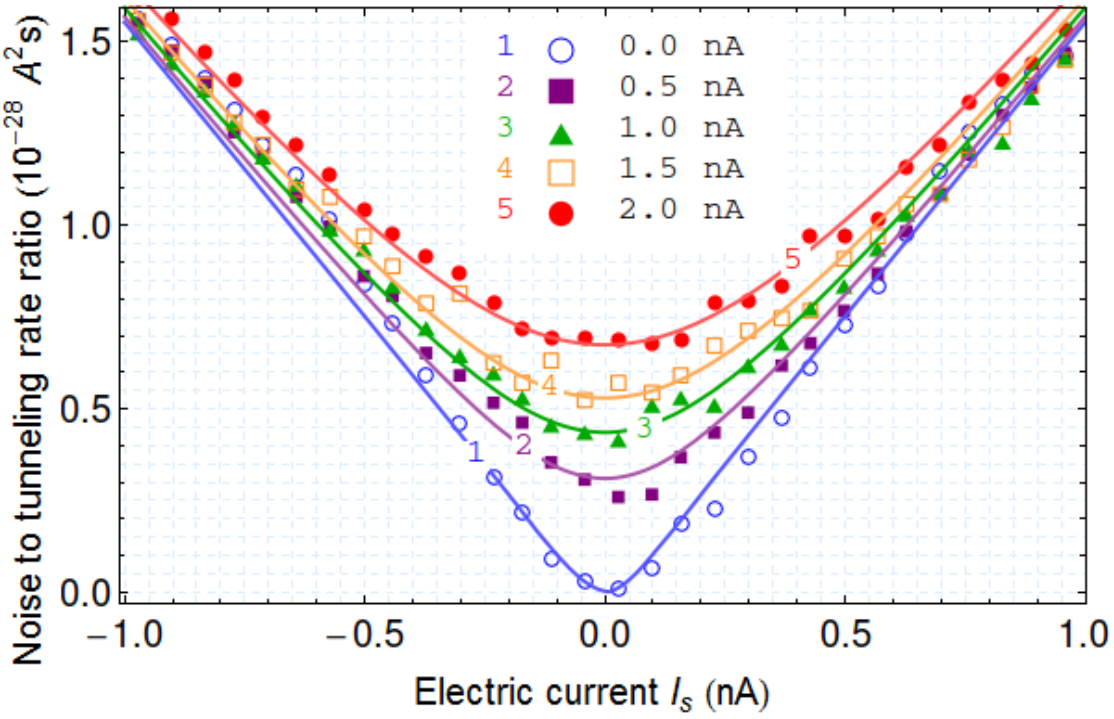

Figure 2.4: **Excess noise to tunnelling rate ratio as a function of the current I_s.** Shown are experimental points and fits thereof by theoretical curves for different values of the current I_n. The legend shows the I_n value in nA for each curve (plot symbol). Fitting parameter λ is defined independently for each value of I_n. Parameter θ is set to $\theta = \theta_{\text{mean}} = \sum_i \theta_i/5 = 0.39$.

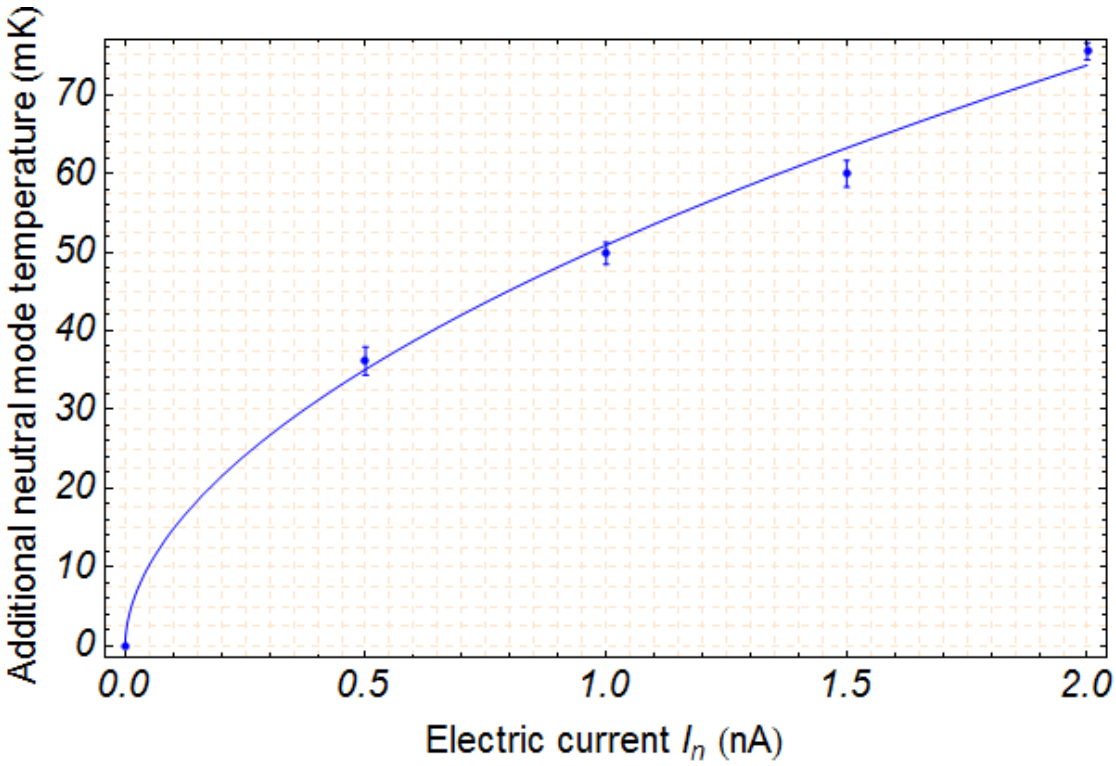

Figure 2.5: **Excess temperature of the upper edge $T_n - T_0$ as a function of the current I_n.** (Color online). Comparison of the points obtained from the data in Table 2.3 with the fit of these points by formula (2.48) is shown.

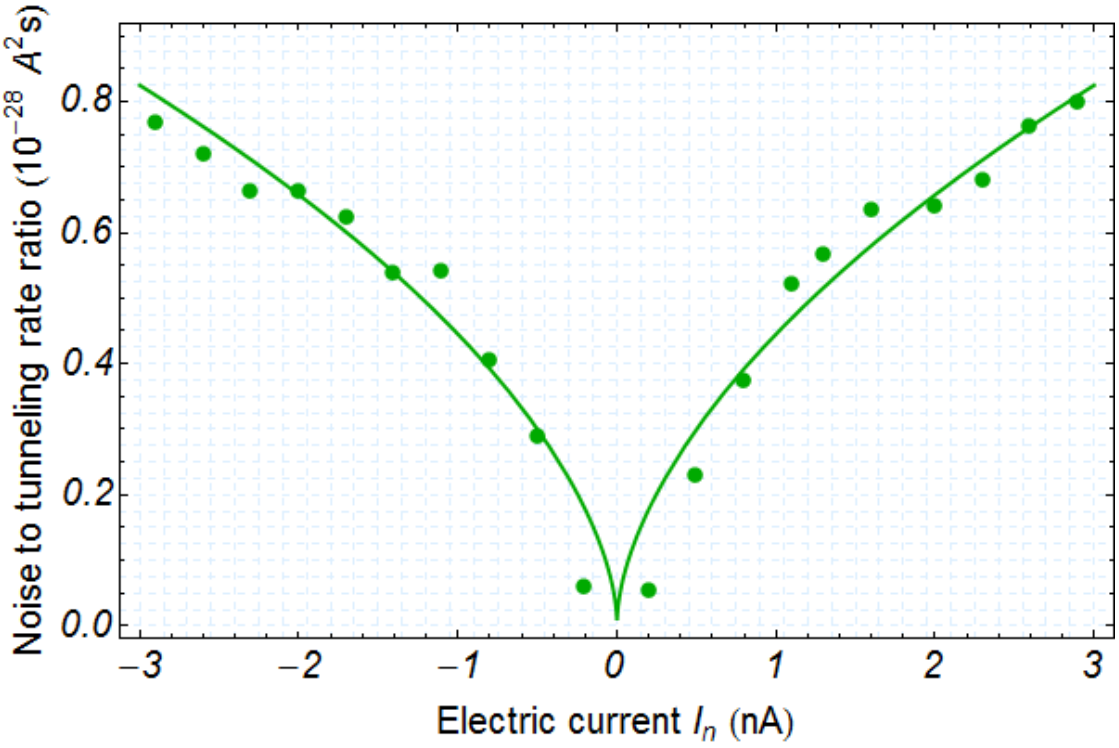

Figure 2.6: **Excess noise to tunnelling rate ratio for $I_s = 0$ as a function of current I_n.** (Color online). Experimental points are taken from Fig. 2 of [1] for the tunnelling rate $r \approx 0.2$. The theoretical curve is obtained for $\theta = \theta_{mean} = \sum_i \theta_i/5 = 0.39$. The values of λ are given by Eq. (2.48). No fitting procedure is involved.

noise to tunnelling rate ratio in terms of a single quasiparticle tunnelling, one would get an unnatural value of Q lying between $e/3$ and $2e/3$. The minimal model of the $\nu = 2/3$ edge explains this contradiction in a natural way: the experimentally observed "charge" is a weight average of the charges of two equally relevant quasiparticles with weights defined by non-universal tunnelling amplitudes' ratio θ. This gives an extra argument in favour of the minimal model of the $\nu = 2/3$ edge with the K-matrix (2.25). A similar point was made in paper [35] in relation to the experiment [33].

Note, that the minimal model analyzed here can also be regarded as the low-energy limit of the extended models proposed in Refs. [35, 34]. At higher energies both extended models predict tunnelling contact physics to be dominated by a quasiparticle with charge $e/3$. Since we do not see this in our analysis, we conclude that either the extended physics is not present in the system or occurs above the energies probed in the experiment of Ref. [1].

It should, however, be emphasized that the minimal $\nu = 2/3$ edge model alone is not sufficient to describe the present experiment. Extra assumptions are needed to model the non-universal physics of Ohmic contacts, edge equilibration mechanisms, and the tunnelling contact. Such assumptions have been discussed throughout the text, here we summarize them:

- injection of electric current into an Ohmic contact induces non-equilibrium noise in the neutral mode but not in the charged mode;
- injection of electric current into an Ohmic contact does not induce a shift in the neutral mode chemical potential (that is the thermodynamic potential dual to the neutral charge defined through Eqs. (2.6) and (2.26));
- strong equilibration of the charged and the neutral modes takes place along the edge resulting in some current-dependent local temperature of the edge;
- the tunnelling contact can be modelled by the minimal tunnelling Hamiltonian (2.28) with tunnelling amplitudes depending on the edge chemical

potential in some non-universal way.

While these phenomenological assumptions are plausible, they may not be accurate. Moreover, their validity may depend on the experimental conditions.

The theoretical framework presented here enables a more detailed experimental investigation and refinement of our understanding of non-equilibrium processes at the edge. For example, in the present work we use experimental data to establish a phenomenological law (2.48) describing the dependence of the neutral mode temperature at the QPC on the current I_n (see Figs. 2.5 and Fig. 2.6). Recently there has been some theoretical progress in understanding of the interaction of Ohmic contacts with the quantum Hall edge [48]. However, at present a complete theoretical predictive model of Ohmic contacts is still missing, and the information on the neutral mode heating may contribute to its development.

It is also interesting to note that we do not find any significant dependence of the ratio of the tunnelling amplitudes of different species of quasiparticles on the currents I_n, I_s (see discussion of Figs. 2.3 and 2.4). This is surprising since the tunnelling amplitudes themselves appear to vary significantly to explain the tunnelling rate dependence on I_s observed in [1]. This fact suggests the existence of a mechanism which ensures roughly equal participation of all three quasiparticles species in the tunnelling. It is known [27, 28] that disorder scattering at the edge enforces the SU(2) symmetry between the quasiparticle species. A similar mechanism might be responsible for the discussed phenomenon.

We emphasize that our theoretical predictions are derived in the limit of perturbatively weak tunnelling of the quasiparticles. Therefore, the tunnelling rate at which the comparison with the experimental data is made should be small enough so that our theory remains valid, but large enough in order to minimize statistical errors of the noise to tunnelling rate ratio.

2.1.8 Summary of the section

Using the chiral Luttinger liquid theory of the quantum Hall edge we develop a quantitative model of the experiment reported in [1]. This model enables us to extract important quantitative information about non-equilibrium processes in Ohmic and tunnelling contacts from the experimental data. In particular, for $\nu = 2/3$, we find a power-law dependence of the neutral mode temperature on the charge current injected from the Ohmic contact. We also find a surprising behavior of quasiparticle tunnelling amplitudes which may be a signature of the SU(2) symmetry in the quasiparticle tunnelling across the QPC.

2.2 Tunnelling quasiparticle's scaling dimension from tunnelling current noise measurements

2.2.1 Introduction

The effective low-energy edge theories' methodology provides a powerful framework for theoretical study of FQHE. However, typically for a given filling factor ν there are several candidate theories with similar main properties (such as the Hall conductance) but different in other ones (such as the presence of non-abelian quasiparticles). Thus, it is desirable to be able to discriminate between them. It is even more valuable to extract explicit constraints on some of the parameters of the theories from the experimental data. If no existing theory fits the data, the explicit restrictions on theory parameters can provide clues on how to find the correct one.

An important characteristic of an edge theory is the spectrum of local quasiparticles the theory contains. Each quasiparticle has two important quantum numbers: the electric charge and the scaling dimension. In the case of weak tunnelling at a quantum point contact (QPC) the quasiparticle with the smallest scaling dimension (the most relevant quasiparticle) provides the most important

contribution to the measured quantities. One may expect to extract the charge and scaling dimension of the particle from transport measurements in such a system. Even such a small amount of data as the properties of the most relevant quasiparticle can significantly reduce the number of candidate theories. This can be seen, for example, from the theoretical study of Ref. [49], relating to $\nu = 5/2$.

It is, in principle, possible to extract the charge and the scaling dimension from the tunnelling current measurements only (see an experimental work of Ref. [50] and references to theory therein). Though, it is well known (see e.g. [45, 46, 47] and references therein) that the tunnelling amplitudes in electrostatically confined QPCs strongly depend on the applied bias voltage in an unknown non-universal way, probably due to charging effects. Thus, the charge and scaling dimension provided by such approach cannot be considered as 100% reliable. Even in the simplest FQHE case of $\nu = 1/3$ experimental and theoretical curves agree only qualitatively but not quantitatively (see e.g. Ref. [51]).[8]

It has been shown in the previous section of this chapter that considering the ratio of the tunnelling current noise to the tunnelling rate allows one to exclude the unwanted non-universal dependence in the weak tunnelling regime in the case of a single quasiparticle type tunnelling. The fractional charge of the most relevant quasiparticle for $\nu = 1/3$ was first confirmed [8, 9] by methods essentially equivalent to the analysis of the noise to tunnelling rate ratio. In this section we focus on the possibility to extract the scaling dimension of the most relevant quasiparticle from such data, paying particular attention to the $\nu = 1/3$ case as the simplest one.

[8]Moreover, in the case of $\nu = 1$ the experimental curves also deviate from the behaviour one would expect theoretically [52]. Ref. [52] explains this by emergence of isles of fractional QHE in the QPC region. However, phenomenologically one can interpret this as the bias voltage dependence of the tunnelling amplitudes that determine tunnelling between the $\nu = 1$ edges.

2.2.2 Scaling dimension from the noise to tunnelling rate ratio

It turns out that the results (2.39)-(2.46) are valid not only for the case when a FQHE edge is described by the minimal $\nu = 2/3$ edge model but also for a wide class of typical abelian and non-abelian FQHE edge models.[9] One should only modify the number of the parameters θ_i (according to the number of the most relevant excitations), use the excitation charges Q_i and scaling dimension δ appropriate for the edge model.[10] Thence the results of this subsection are also applicable for a wide class of models.

Consider the large I_s limit of the Eq. (2.39). For $|I_s| \gg \lambda I_0 \geq I_0$ one gets[11]

$$X(I_s)\big|_{|j_s|\gg\lambda\geq 1} = \frac{\tilde{S}(\omega=0)}{r} = eI_s\frac{\sum_i \theta_i F_i}{\sum_i \theta_i G_i} = \\ = e|I_s|\frac{\sum_i \theta_i Q_i^{4\delta+1}}{\sum_i \theta_i Q_i^{4\delta}} + eI_0\frac{2-8\delta}{\pi} + O\left(|j_s|^{-1}\right). \quad (2.49)$$

We remind the reader that

$$j_s = \frac{I_s}{I_0}, \quad I_0 = \nu\frac{e}{h}\pi k_B T_s = \nu\frac{e}{h}\pi k_B T_0, \quad (2.50)$$

where I_s is the electric current flowing along the lower edge before the *QPC*, $\lambda = T_n/T_s$, T_n is the local upper edge temperature at the *QPC*, $T_s = T_0$ is the local lower edge temperature at the *QPC*, e is the elementary charge, $h = 2\pi\hbar$ is the Planck constant, k_B is the Boltzmann constant, ν is the filling factor, δ is the scaling dimension of the most relevant excitations, and Q_i are the electric charges (in the units of the elementary charge) of the quasiparticles contributing to tunnelling.

[9] See Appendix B.9 for a detailed discussion of this issue.

[10] The definition of the parameters θ_i should also be modified for some edge models: the ratio of the velocities becomes more complex if there are several charged or neutral modes, or disappears if there is only one mode in the model. However, as long as we are going to treat θ_i as phenomenological parameters related to the tunnelling amplitudes of the different excitations that doesn't affect the following considerations.

[11] See Appendix B.10 for derivation.

The leading term of the asymptotic behaviour (2.49) gives the well-known result that in the regime of weak tunnelling the gradient of the noise to tunnelling rate ratio is equal to the tunnelling quasiparticle's charge. In our case it is some average of the charges in the case of several quasiparticles participating in tunnelling. Note the subleading term: constant offset contains information about the quasiparticles' scaling dimension. It is important that all the quasiparticles which significantly contribute to tunnelling have the same scaling dimension.

Thus, in principle, by fitting large I_s experimental data with a linear function one can find not only the "effective charge" of the tunnelling quasiparticles but also their scaling dimension (which is the same for all of the most relevant quasiparticles). However, in practice there are significant restrictions to the useability of this approach. They are discussed below.

2.2.2.1 What experimental conditions are necessary for successful extraction of the scaling dimension?

Now we discuss the possibility to extract the scaling dimension from real experimental data. The result (2.49) shows that it is, in principle, possible to extract the scaling dimension of the tunnelling quasiparticles from experimental data on noise to tunnelling rate ratio without knowing fully the specific edge theory. However, there are few practical aspects which should be discussed.

First of all, the parameters θ_i related to the quasiparticles' tunnelling amplitudes depend on the current I_s in a non-universal way. In the study of the previous section of this chapter, concerning $\nu = 2/3$, we found that the ratios $\theta_i/\theta_{i'}$ do not depend on the current I_s. However, there is no known reason why this should be true for general experimental conditions (other filling factors, other sample etc.). For the sake of simplicity, from now on we concentrate on the case when all the charges of the quasiparticles contributing to tunnelling are equal: $Q_i = Q$. Then,

independently of θ_i,

$$X(I_s)\big|_{|j_s|\gg\lambda\geq 1} = eQ|I_s| + eI_0\frac{2-8\delta}{\pi} + O\left(|j_s|^{-1}\right). \tag{2.51}$$

Let us note that in this case for $\lambda = 1$ it is possible to write a simple analytic expression for the original noise to tunnelling rate ratio[12]:

$$X(I_s)\,|_{\lambda=1} = \frac{2eQI_s}{\pi}\mathrm{Im}\left[\psi\left(2\delta + \frac{iQj_s}{2}\right)\right], \tag{2.52}$$

where the digamma function $\psi(x) = (\ln\Gamma(x))'$ is the logarithmic derivative of the Euler gamma function $\Gamma(x)$, and Im[...] denotes taking of the imaginary part.

Second issue is that the dynamics of the system changes near a characteristic energy scale in the FQHE system. Namely, there is a bulk gap Δ. As the typical energies of the system exceed Δ bulk dynamics starts being involved. Thus one should restrict oneself to

$$|I_s| \lesssim \nu\frac{e}{h}\pi\Delta. \tag{2.53}$$

Deviations from our theory can be expected beyond this threshold.[13]

Third issue is the lower boundary above which the result (2.51) is applicable. Fig. 2.7 shows the comparison of the noise to tunnelling rate ratio (2.52) against its asymptotic behaviour (2.51) for $Q = 1/3$ and $\delta = 1/6$. These parameters correspond to the most relevant quasiparticle of the simplest $\nu = 1/3$ edge model. As one can see, for $|I_s| \geq 3I_0$ the NtTRR and its large I_s asymptote almost coincide.

To estimate how close are the asymptote and the original curve we have done some fitting. Namely, we took part of the original curve with $|I_s|$ between αI_0 and $10I_0$ and fitted it with (2.51) using Q and δ as fitting parameters. For $\alpha \geq 3$ the fitted charge and scaling dimension deviate from their correct values by no more

[12]Derivation is given in Appendix B.11.

[13]Similar applicability restrictions are put by the energy cutoffs of charged and neutral modes, which are considered in some works, e.g. [35]. However, typically these cutoffs are of the same order as or greater than the bulk gap Δ.

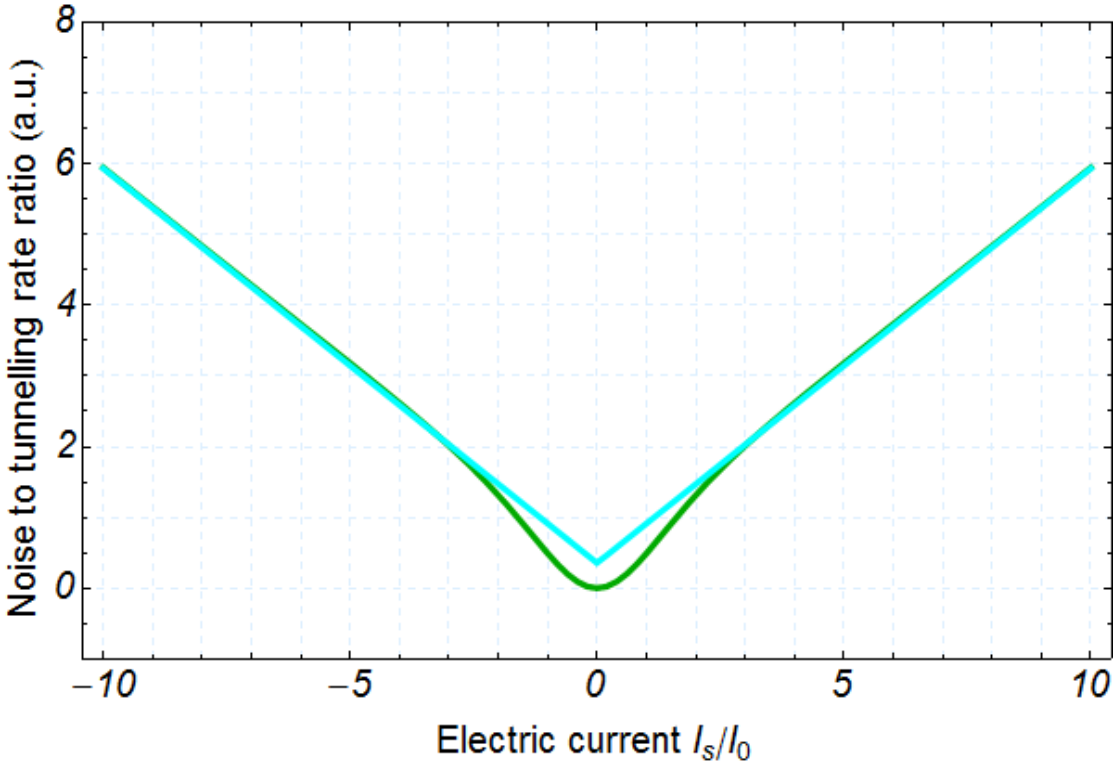

Figure 2.7: **Noise to tunnelling rate ratio vs its asymptotic behaviour**. The green curve is the original noise to tunnelling rate ratio at $\lambda = 1$ (2.52) for $Q = 1/3$, $\delta = 1/6$. The cyan curve is the large I_s asymptote (2.51) for the same values of Q and δ. The asymptote almost coincides with the original curve for $|I_s| \geq 3I_0$.

than 1% and 11% respectively. This gives an idea how accurate can be estimates of Q and δ obtained from fitting experimental data if there are no other sources of errors.

Thus, for equal temperatures of the edges one can use the asymptotic expression (2.51) for $|I_s| \gtrsim \alpha I_0$, $\alpha = 3$. Of course, the border value of the multiplier α somewhat differs for different models (different Q, δ).

Note that the greater is I_0 the more significant is the term containing the scaling dimension in Eq. (2.51). At the same time, the less is the interval $\nu \frac{e}{h} \pi \Delta \gtrsim |I_s| \gtrsim \alpha I_0$. Thus the choice of the system temperature should be a matter of trade-off between these to restrictions in order to allow as good determining of the scaling dimension δ as possible.

Fourthly. The asymptotic behaviour (2.51) is valid only when the contribution of less relevant quasiparticles (with greater scaling dimensions) to the tunnelling processes can be neglected. Otherwise the corrections due to less relevant quasiparticles can hinder finding the scaling dimension using the large I_s NtTRR behaviour. Unfortunately, there are no known reliable ways to estimate theoretically how significant are these corrections. Thus, it should be done in practice by comparing experimental data with different possible theoretical answers for NtTRR (the answers including and not including less relevant quasiparticles).

Fifth issue is related to measurement errors. Scaling dimension enters Eq. (2.51) as a subleading term. Thus finding the scaling dimension demands a very high quality experimental data with very small statistical errors. The tunnelling current noise errors can be made less significant by using greater values of tunnelling rate. This, however, worsens the accuracy of theoretical result (2.51) which was derived perturbatively in the limit of small tunnelling rate. Therefore, the choice of the strength of tunnelling in experimental data should be balanced between worsening the applicability of the theory and bettering the quality of data for NtTRR. The most appropriate choice should probably be found by trial and error method.

Sixth issue has just been mentioned above. The theoretical result (2.51) was derived perturbatively in the limit of weak tunnelling of the quasiparticles. One can reasonably expect that if the tunnelling rate is about, e.g., 10% the next perturbative correction to (and the inaccuracy of) the NtTRR should also be around 10%. While such inaccuracy would bring an error of the same order to the determined charge Q, the effect on the subleading term may be much more significant. This compromises the possibility to find the scaling dimension with this approach. The question, how small should be the tunnelling rate for the result (2.51) to be applicable enough, is investigated in detail in the next subsection. There we find that for $\nu = 1/3$ for typical experimental parameters one needs the tunnelling rate $r \lesssim 5\%$ so that the inaccuracy of the perturbative formulae does not bring in a too large error, allowing to find δ reasonably accurately.

To summarize, the large I_s asymptotic behaviour of NtTRR (2.51) can, in principle be used to find the scaling dimension of the most relevant quasiparticle. However, in practice this is somewhat restricted due to several reasons. The degree of some of these restrictions can only be estimated by trying to apply this method practically, which will be the matter of future research.

One of the restrictions is due to the perturbative nature of Eq. (2.51). Fortunately, for the simplest model of $\nu = 1/3$ edge the tunnelling rate and the tunnelling current noise can be found exactly [41, 53, 54]. In the next subsection we compare our answer with the exact one in order to investigate the significance of the corrections to our answer.

2.2.3 Exact answers for $\nu = 1/3$ and the conditions to extract the scaling dimension by perturbative formulae

In this subsection we concentrate on the filling factor $\nu = 1/3$. The minimal edge model for this filling factor has only one edge mode represented by the chiral bosonic field and can be constructed in the way described in subsection 2.1.4. The electric charge and the scaling dimension of the most relevant quasiparticle in this

model are respectively equal to $Q = 1/3$, $\delta = 1/6$.

This model is usually considered to be the one which should actually describe the FQHE at $\nu = 1/3$. However, that statement has not been reliably confirmed yet. While the charge of the most relevant quasiparticle has been confirmed long time ago [8, 9], this is not true for its statistics or other properties of the model.[14] Therefore, finding the most relevant quasiparticle's scaling dimension would be an important check of the validity of the minimal model.

However, as is was noted in the previous subsection finding the scaling dimension from large I_s asymptotic behaviour of NtTRR has a number of difficulties, one of which is related to the perturbative nature of the theoretical formulae. Fortunately, for the minimal model of the $\nu = 1/3$ edge there is an exact solution of the problem of the most relevant quasiparticle tunnelling at QPC which allows for finding of the tunnelling rate and the tunnelling current noise [41, 53, 54].

In this subsection we compare the perturbative answer for NtTRR with the exact one in order to find out at what tunnelling rates the perturbative result can be applied for finding the scaling dimension. While in order to use exact answers at non-zero temperature involves some complication[15], we concentrate on the case of zero temperature of both edges ($T_n = T_s = T_0 = 0$) where analytic expressions are available.

The exact answer for the tunnelling rate $r = |I_T/I_s|$ at zero temperature is as

[14] Moreover, recently there has been a report [55], results of which may be interpreted as a signature of presence of additional neutral modes in the $\nu = 1/3$ FQHE. However, in the present work we are not going to discuss this evidence.

[15] In that case one has to solve equations of thermodynamical Bethe anzatz either numerically or by some other means in order to find NtTRR. We haven't done this yet and this is a matter of future research.

follows:

$$r\left(|I_s| > \Xi e^{\zeta}\right) = \nu \sum_{n=1}^{\infty} A_n(\nu) \left(\frac{|I_s|}{\Xi}\right)^{2n(\nu-1)}, \quad (2.54)$$

$$r\left(|I_s| < \Xi e^{\zeta}\right) = 1 - \nu^{-1} \sum_{n=1}^{\infty} A_n(\nu^{-1}) \left(\frac{|I_s|}{\Xi}\right)^{2n(\nu^{-1}-1)}, \quad (2.55)$$

$$A_n(x) = (-1)^{n+1} \frac{\sqrt{\pi}\Gamma(nx)}{2\Gamma(n)\Gamma(3/2 + n(x-1))}, \quad (2.56)$$

$$\zeta = \frac{1}{2}\ln(1-\nu) + \frac{\nu}{2(1-\nu)}\ln\nu. \quad (2.57)$$

The tunnelling amplitude η in the perturbative formulae (2.39)-(2.41) and the parameter Ξ here are related: $\Xi \propto |\eta|^{1/(1-\nu)}$. Thus Ξ characterizes the tunnelling strength. The restrictions on $|I_s|$ in the first two formulae represent the radii of convergence of the series.[16]

According to Ref. [53], at zero temperature the excess noise at zero frequency $\tilde{S}(\omega = 0)$ is connected to the tunnelling rate r via

$$\tilde{S}(\omega = 0, I_s) = \frac{\nu e}{2(1-\nu)} |I_s| \times \Xi \frac{\partial}{\partial \Xi} r(I_s). \quad (2.58)$$

The explicit series are

$$\tilde{S}\left(\omega = 0, |I_s| > \Xi e^{\zeta}\right) = \nu^2 e |I_s| \sum_{n=1}^{\infty} n A_n(\nu) \left(\frac{|I_s|}{\Xi}\right)^{2n(\nu-1)}, \quad (2.59)$$

$$\tilde{S}\left(\omega = 0, |I_s| < \Xi e^{\zeta}\right) = \nu^{-1} e |I_s| \sum_{n=1}^{\infty} n A_n(\nu^{-1}) \left(\frac{|I_s|}{\Xi}\right)^{2n(\nu^{-1}-1)}. \quad (2.60)$$

It is easy to see expansion in the orders of the tunnelling amplitude η in the formulae (2.54), (2.59). Taking only the first term in the sums in Eqs. (2.54), (2.59) one should recover the lowest order perturbation theory result for the regime of weak tunnelling. This is indeed the case.[17] Note that while the perturbative noise

[16] In Ref. [53] the definition of ζ (which is called Δ there) contains a misprint. However, one can check and find that the radius of convergence of the series leads to the definition of ζ presented here.

[17] There is a small subtlety here. To adapt the perturbative answers (2.39)-(2.46) for $T = 0$ one should take the limit $T \to 0$ which coincides with the limit $|j_s| >> 1$. Then up to a factor one recovers the expression one can get from taking only the first term in the sums in Eqs. (2.54),

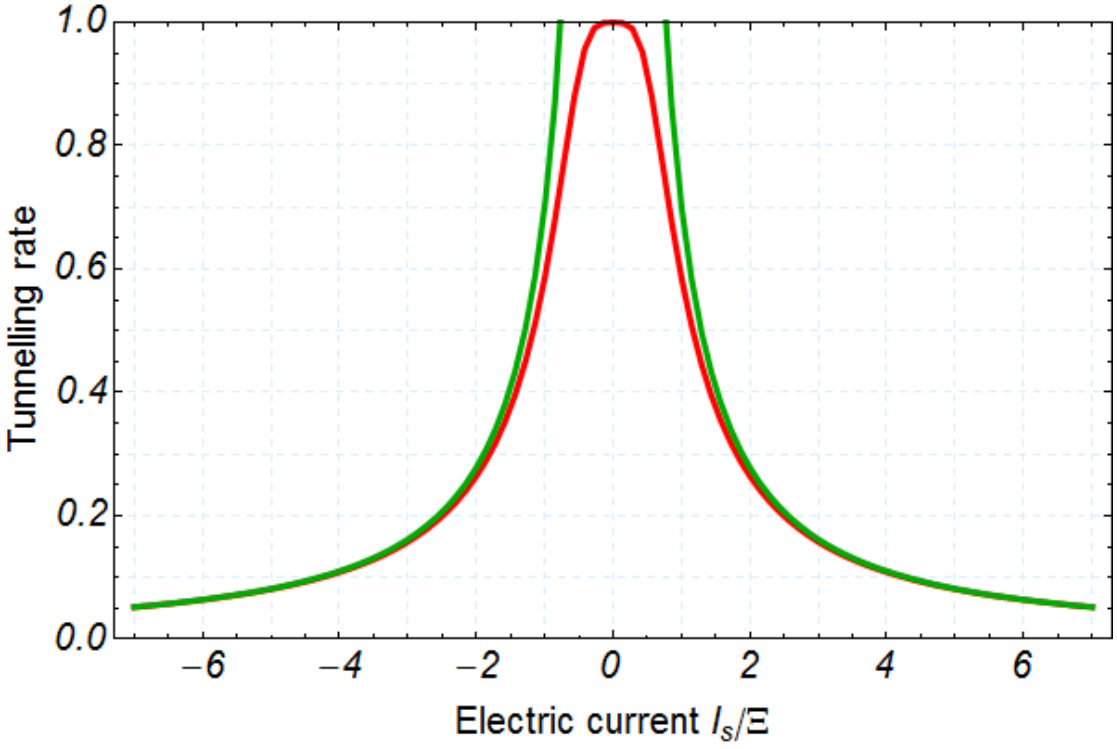

Figure 2.8: **Tunnelling rate at $\nu = 1/3$. Perturbative answer vs exact answer.** The red curve is the exact tunnelling rate given by Eqs. (2.54), (2.55). The green curve is the lowest order perturbation theory answer for the tunnelling rate, which can be obtained by taking only the first term in the sum in Eq. (2.54). We remind the reader that the system temperature is equal to $T_0 = 0$.

to tunnelling rate ratio $X(I_s) = \tilde{S}(\omega = 0, I_s)/r(I_s)$ does not depend on the value of the tunnelling amplitude η (or Ξ, which is equivalent), the exact NtTRR does.

We now compare the exact answers with the perturbative ones. Fig. 2.8 shows the comparison of the perturbative and the exact answers for the tunnelling rate. For tunnelling rates[18] not exceeding 0.2 the two answers are reasonably close. Note, that knowing the tunnelling rate at a certain value of the current I_s one can find the corresponding value of the tunnelling amplitude Ξ.

Fig. 2.9 shows the comparison of the perturbative and the exact answers for the noise to tunnelling rate ratio. Since the temperature $T_0 = 0$ the perturbative answer for NtTRR is just $X_{\text{pert}}(I_s) = eQ|I_s|$. The deviation of the perturbative NtTRR from the exact one can be noticed even in the regime when the perturbative tunnelling rate almost coincides with the exact one.

(2.59). This factor is related to the proportionality factor between Ξ and $|\eta|^{1/(1-\nu)}$.

[18] We remind that the tunnelling rate lies between 0 and 1 by definition.

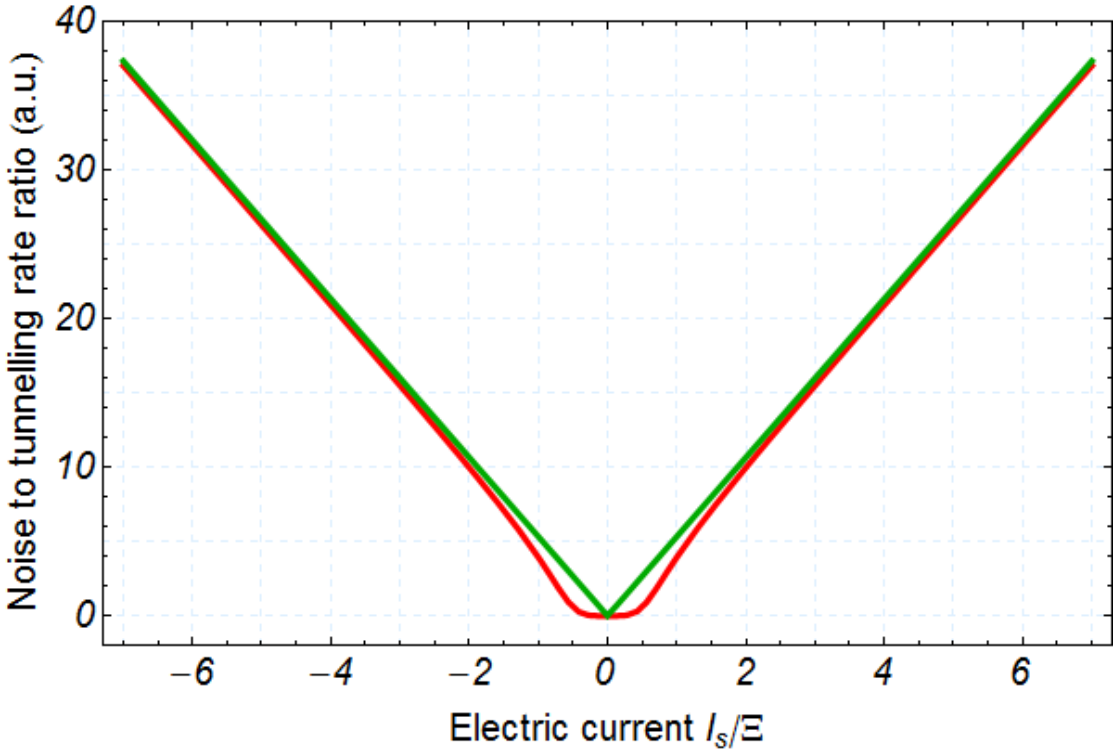

Figure 2.9: **Noise to tunnelling rate ratio at $\nu = 1/3$. Perturbative answer vs exact answer.** The red curve is the exact NtTRR plotted using the Eqs. (2.54)–(2.60). The green curve is the lowest order perturbation theory answer for the NtTRR, which can be obtained by taking only the first term in the sums in Eqs. (2.54), (2.59). We remind the reader that the system temperature is equal to $T_0 = 0$.

While the comparison made in Fig. 2.9 allows one to estimate the deviation of the exact answer from the perturbative one, it does not resemble the expected comparison of experimental curves with the perturbative answer. This is because the tunnelling amplitude Ξ in a real experiment exhibits a non-universal dependence on I_s. Experimentalists like to work (see e.g. [1]) in the regime of constant tunnelling rate. As can be seen from Fig. 2.8 this regime corresponds to the ratio $|I_s|/\Xi$ being constant.

Fig. 2.10 shows the comparison of the perturbative and the exact answers for the noise to tunnelling rate ratio for $|I_s|/\Xi = 2$. Since the temperature $T_0 = 0$ the perturbative answer for NtTRR is just $X_{\rm pert}(I_s) = eQ|I_s|$. The exact answer in the regime $|I_s|/\Xi = \text{const} > e^{\zeta}$ is equal to $X_{\rm exact}(I_s) = eQ^*|I_s|$. So the exact answer differs from the perturbative one by the gradient value determined by the "effective charge" Q^*. In the limit of infinitely small tunnelling rate $|I_s|/\Xi \to \infty$ the effective charge coincides with the true charge of the tunnelling quasiparticle: $Q^* \to Q$. However, at finite values of $|I_s|/\Xi > e^{\zeta}$ the charges do not coincide: $Q^* < Q$.

Although at the moment we are not able to estimate the deviation of the perturbative answer for NtTRR from the exact one at non-zero temperature, the observation that has just been made allows to formulate some qualitative conditions for applicability of the formula (2.51). Namely, one can compare the difference between the answers at zero temperature $e(Q - Q^*)|I_s|$ at maximum value of $|I_s|$ which is going to be used with the term $eI_0(2 - 8\delta)/\pi = (2 - 8\delta)k_B T_0 \nu e^2/h$ in Eq. (2.51), where T_0 is the system temperature.

For example, at $T_0 = 10$ mK for $|I_s|/\Xi = 2$ (which corresponds to the tunnelling rate $r \approx 26\%$) at $I_s = 1$ nA for Lauglin quasiparticle ($Q = 1/3$, $\delta = 1/6$) the term containing δ is about three times smaller than the error $e(Q - Q^*)|I_s|$. Therefore, finding the scaling dimension of the Laughlin quasiparticle with the help of Eq. (2.51) is not possible under these experimental conditions.

For typical experimental values of $T_0 = 30$ mK and $I_s = 1$ nA the error term

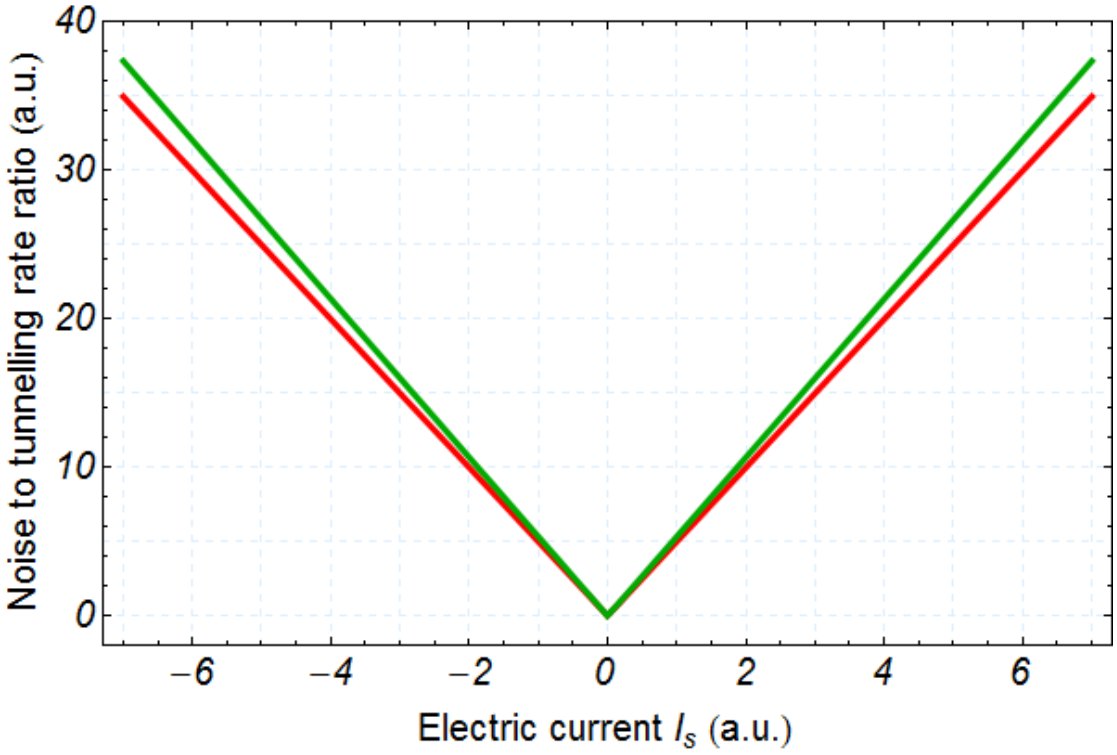

Figure 2.10: **Noise to tunnelling rate ratio at $\nu = 1/3$. Perturbative answer vs exact answer in the regime of constant tunnelling rate ratio.** The red curve is the exact NtTRR plotted using the Eqs. (2.54)–(2.60) for $\Xi = 0.5|I_s|$. The green curve is the lowest order perturbation theory answer for the NtTRR, which can be obtained by taking only the first term in the sums in Eqs. (2.54), (2.59). We remind the reader that the system temperature is equal to $T_0 = 0$.

does not exceed $(2-8\delta)k_BT_0\nu e^2/h$ for $r \leq 27\%$ and does not exceed $0.1 \times (2-8\delta)k_BT_0\nu e^2/h$ for $r \leq 4\%$. When $e(Q-Q^*)|I_s|$ is 10 times smaller than the term containing δ, one can hope to find δ with a reasonably small error. Thus, if the quality of the experimental data at $r \approx 4\%$ is high enough, it should be possible to find δ reasonably accurately (with the systematic relative error $\approx 10-20\%$ due to (a) difference between the exact answer and the perturbative one and (b) difference between the perturbative answer and its large-I_s asymptotic behaviour) by fitting the experimental data for NtTRR with Eq. (2.51).

Apart from that, the deviation of the effective charge Q^* from the quasiparticle charge Q at higher values of the tunnelling rate r gives an opportunity to further check the edge model and the tunnelling contact model at $\nu = 1/3$.

2.2.4 Summary of the section

Using chiral Luttinger liquid theory of QH edge and perturbative treatment of tunnelling processes, we develop a method for finding the scaling dimension of the most relevant quasiparticle at a QH edge using tunnelling current and tunnelling current noise measurements. The advantages of the method are (a) reduced sensitivity to the non-universal physics of tunnelling contacts (compared to methods based solely on tunnelling current measurements), (b) certain degree of model independence. By comparing our perturbative results with the exact results of Ref. [53] in the case of $\nu = 1/3$ we find that our method should be applied for small enough tunnelling rates $r \lesssim 5\%$.

Using the exact solution of Ref. [53] at $\nu = 1/3$ for higher tunnelling rates, we find that the effective charge Q^* which can be found from an experiment using standard perturbative formulae deviates from the true charge of the most relevant quasiparticle Q. We propose to measure and study this difference in order to check the minimal $\nu = 1/3$ edge model and the tunnelling contact model.

Conclusions

In the present work we study two different problems: (a) problem of realizing specific fractional quantum Hall states in bilayer graphene and (b) problem of characterization of fractional quantum Hall states using tunnelling current noise measurements.

Regarding the first problem, we develop a method for taking into account the corrections due to interaction of different Landau levels. Using the developed method we study the possibility to realize the Pfaffian FQHE state in bilayer graphene and plot the phase diagram. We find that reliable predictions can be made only for large enough substrate dielectric constants. The developed methodology can be straightforwardly applied to study the possibility to realize any specific FQHE state in bilayer graphene.

Regarding the second problem, we develop a methodology for quantitative comparison of the tunnelling current noise measurements with corresponding theory. We test this methodology by successfully applying it to the data of the experiment of Ref. [1]. We further develop this methodology and propose a method for model-independent determination of the scaling dimension of the most relevant quasiparticle excitation.

Appendix A

Appendices related to Chapter 1

A.1 Derivation of the expression for pseudopotentials through the Fourier transform of the interaction potential

By definition,

$$|n_1, n_2, m, M\rangle = \frac{1}{\sqrt{2^{m+M} m! M!}} (\hat{b}_1^\dagger - \hat{b}_2^\dagger)^m (\hat{b}_1^\dagger + \hat{b}_2^\dagger)^M (\psi_{n_1,-n_1})_1 (\psi_{n_2,-n_2})_2, \quad \text{(A.1)}$$

$$V_m^{(n_1,n_2)} = \langle n_1, n_2, m, M|\hat{V}|n_1, n_2, m, M\rangle = \langle n_1, n_2, m, 0|\hat{V}|n_1, n_2, m, 0\rangle. \quad \text{(A.2)}$$

The direct Fourier transform for the interaction potential is defined in (1.31), the inverse Fourier transform looks like

$$V(r) = \int \frac{d^2q}{(2\pi)^2} \tilde{V}(q) e^{i\vec{qr}/l}. \quad \text{(A.3)}$$

Now we can rewrite the definition (A.2) as follows:

$$V_m^{(n_1,n_2)} = \langle n_1, n_2, m, M|\hat{V}|n_1, n_2, m, M\rangle = \int d^2r_1 d^2r_2 \bar{\psi}_{n_1,n_2,m,M}(\vec{r}_1,\vec{r}_2)V(r)\psi_{n_1,n_2,m,M}(\vec{r}_1,\vec{r}_2) = \int \frac{d^2q}{(2\pi)^2}\tilde{V}(q)\langle n_1, n_2, m, M|e^{i\vec{q}\hat{\vec{r}}/l}|n_1, n_2, m, M\rangle. \quad (A.4)$$

Introducing $x = q_x + iq_y$, we can write $\vec{q}\vec{r}/l = (x\bar{w} + \bar{x}w)/2$. $w, \bar{w}$ can be expressed through the $\hat{a}, \hat{a}^\dagger, \hat{b}, \hat{b}^\dagger$ operators:

$$w = \sqrt{2}(\hat{a} + \hat{b}^\dagger),\ \bar{w} = \sqrt{2}(\hat{a}^\dagger + \hat{b}). \quad (A.5)$$

Thus, we need to find the matrix element

$$\langle n_1, n_2, m, M|e^{i\vec{q}\hat{\vec{r}}/l}|n_1, n_2, m, M\rangle = \langle n_1, ...|e^{\frac{i}{\sqrt{2}}(x(\hat{a}_1^\dagger - \hat{a}_2^\dagger + \hat{b}_1 - \hat{b}_2) + \bar{x}(\hat{a}_1 - \hat{a}_2 + \hat{b}_1^\dagger - \hat{b}_2^\dagger))}|n_1, ...\rangle. \quad (A.6)$$

This matrix element can be easily rearranged into a product of three different matrix elements:

$$\langle n_1, n_2, m, M|e^{i\vec{q}\hat{\vec{r}}/l}|n_1, n_2, m, M\rangle = \mathrm{ME}_{n_1}\mathrm{ME}_{n_2}\mathrm{ME}_m, \quad (A.7)$$

$$\mathrm{ME}_{n_1} = \langle n_1|e^{\frac{i}{\sqrt{2}}(x\hat{a}_1^\dagger + \bar{x}\hat{a}_1)}|n_1\rangle, \quad (A.8)$$

$$|n_1\rangle = \frac{1}{\sqrt{n_1!}}(\hat{a}_1^\dagger)^{n_1}|\Omega\rangle, \quad (A.9)$$

$$\hat{a}_1|\Omega\rangle = 0, \quad (A.10)$$

$$\mathrm{ME}_{n_2} = \langle n_2|e^{-\frac{i}{\sqrt{2}}(x\hat{a}_2^\dagger + \bar{x}\hat{a}_2)}|n_2\rangle, \quad (A.11)$$

$$|n_2\rangle = \frac{1}{\sqrt{n_2!}}(\hat{a}_2^\dagger)^{n_2}|\Omega\rangle, \quad (A.12)$$

$$\hat{a}_2|\Omega\rangle = 0, \quad (A.13)$$

$$\begin{aligned} \mathrm{ME}_m &= \langle m|e^{\frac{i}{\sqrt{2}}(x(\hat{b}_1-\hat{b}_2)+\bar{x}(\hat{b}_1^\dagger-\hat{b}_2^\dagger))}|m\rangle, && \text{(A.14)} \\ |m\rangle &= \frac{1}{\sqrt{2^m m!}}(\hat{b}_1^\dagger-\hat{b}_2^\dagger)^m|\Omega\rangle, && \text{(A.15)} \\ (\hat{b}_1-\hat{b}_2)|\Omega\rangle &= 0. && \text{(A.16)} \end{aligned}$$

It is easy to see that all the three expressions are very similar. Let's see how to calculate, e.g., ME_{n_1}. Baker-Campbell-Hausdorff identity says that

$$e^{\alpha\hat{a}_1^\dagger+\beta\hat{a}_1} = e^{\alpha\hat{a}_1^\dagger}e^{\beta\hat{a}_1}e^{\alpha\beta/2}. \tag{A.17}$$

Thus

$$e^{\frac{i}{\sqrt{2}}(x\hat{a}_1^\dagger+\bar{x}\hat{a}_1)} = e^{\frac{i}{\sqrt{2}}x\hat{a}_1^\dagger}e^{\frac{i}{\sqrt{2}}\bar{x}\hat{a}_1}e^{-|x|^2/4}. \tag{A.18}$$

Then

$$\begin{aligned} \mathrm{ME}_{n_1} = \langle n_1|e^{\frac{i}{\sqrt{2}}(x\hat{a}_1^\dagger+\bar{x}\hat{a}_1)}|n_1\rangle = \\ e^{-|x|^2/4}\langle n_1|e^{\frac{i}{\sqrt{2}}x\hat{a}_1^\dagger}e^{\frac{i}{\sqrt{2}}\bar{x}\hat{a}_1}|n_1\rangle = \\ e^{-|x|^2/4}\sum_{n=0}^{\infty}\langle n_1|e^{\frac{i}{\sqrt{2}}x\hat{a}_1^\dagger}|n\rangle\langle n|e^{\frac{i}{\sqrt{2}}\bar{x}\hat{a}_1}|n_1\rangle, \end{aligned} \tag{A.19}$$

where we used the identity $\hat{1} = \sum_{n=0}^{\infty}|n\rangle\langle n|$.

After a calculation of the expression

$$\begin{aligned} \langle n|e^{\frac{i}{\sqrt{2}}\bar{x}\hat{a}_1}|n_1\rangle = \sum_{k=0}^{\infty}\frac{1}{k!}\left(\frac{i}{\sqrt{2}}\bar{x}\right)^k\langle n|\hat{a}_1^k|n_1\rangle = \\ = \sum_{k=0}^{\infty}\frac{1}{k!}\left(\frac{i}{\sqrt{2}}\bar{x}\right)^k\delta_{k,n_1-n}\sqrt{\frac{n_1!}{n!}} = \\ \frac{1}{(n_1-n)!}\left(\frac{i}{\sqrt{2}}\bar{x}\right)^{n_1-n}\sqrt{\frac{n_1!}{n!}}, \end{aligned} \tag{A.20}$$

and its complex conjugate, we get

$$\mathrm{ME}_{n_1} = e^{-|x|^2/4} \sum_{n=0}^{n_1} \left(-\frac{|x|^2}{2}\right)^{n_1-n} \frac{n_1!}{n!(n_1-n)!^2} =$$

$$|k = n_1 - n| =$$

$$e^{-|x|^2/4} \sum_{k=0}^{n_1} \left(-\frac{|x|^2}{2}\right)^{k} \frac{n_1!}{(n_1-k)!(k)!^2} =$$

$$e^{-|x|^2/4} \sum_{k=0}^{n_1} \left(-\frac{|x|^2}{2}\right)^{k} \frac{1}{k!} C_{n_1}^k = e^{-|x|^2/4} L_{n_1}(|x^2|/2), \quad \text{(A.21)}$$

where L_{n_1} is the Laguerre polynomial.

Calculation of ME_{n_2}, ME_m is absolutely similar. Gathering all the three matrix elements together we finally get formula (1.32):

$$V_m^{(n_1,n_2)} = \langle n_1, n_2, m, M|\hat{V}|n_1, n_2, m, M\rangle =$$

$$\int_0^\infty \tilde{V}(q) L_m(q^2) L_{n_1}(q^2/2) L_{n_2}(q^2/2) e^{-q^2} \frac{qdq}{2\pi}. \quad \text{(A.22)}$$

A.2 Full Hartree energy of a Landau level

The electrostatic (Hartree) energy per electron of a fully filled Landau level can be expressed as

$$E_{\text{Hartree pp}} = \frac{1}{2N_e} \int d^2x \; d^2y \rho(\mathbf{x})\rho(\mathbf{y}) V(|\mathbf{x}-\mathbf{y}|), \quad \text{(A.23)}$$

where N_e is the number of electrons in the LL, $\mathbf{x}$ and $\mathbf{y}$ are the coordinate vectors of points in the plane, $V(r)$ is the electron-electron interaction potential, and $\rho(\mathbf{x})$ is the electron density, integration is done over the whole plane[1]. Using the fact that for a fully filled LL $\rho(\mathbf{x}) = 1/(2\pi l^2) = \rho$ and changing integration variables

[1]Over the whole sample of area $S \to \infty$ with N_e electrons in the LL so that $S/N_e = 2\pi l^2$. l is the magnetic length.

to $\mathbf{R} = (\mathbf{x} + \mathbf{y})/2$ and $\mathbf{r} = \mathbf{x} - \mathbf{y}$, we get

$$E_{\text{Hartree pp}} = \frac{\rho^2}{2N_e} \int d^2R \; d^2r V(r), \tag{A.24}$$

where $r = |\mathbf{r}|$. $\int d^2R$ is equal to the sample area S. $\rho \times S = N_e$, therefore

$$E_{\text{Hartree pp}} = \frac{\rho}{2} \int d^2r V(r) = \frac{1}{4\pi l^2} 2\pi \int dr V(r) = \frac{1}{2l^2} \int_0^\infty dr \; rV(r), \tag{A.25}$$

in agreement with Eq. (1.84).

This derivation is valid for the potentials that decay sufficiently fast as $r \to \infty$, and the Coulomb interaction does not satisfy this condition. However, only differences of the energies have physical meaning. If we consider two energies for differently screened interaction potentials (1.67):

$$E^{(1)}_{\text{Hartree pp}} - E^{(2)}_{\text{Hartree pp}} = \frac{1}{2l^2} \int_0^\infty dr \; r \left(V^{(1)}(r) - V^{(2)}(r) \right), \tag{A.26}$$

the integral of the difference is convergent since the Coulomb part cancels out and what remains decays sufficiently fast at large distances. Therefore, we can express such difference through the interaction potential Fourier transforms $\tilde{V}(q)$ defined in Eq. (1.31):

$$E^{(1)}_{\text{Hartree pp}} - E^{(2)}_{\text{Hartree pp}} = \frac{1}{4\pi} \lim_{q \to 0} \left(\tilde{V}^{(1)}(q) - \tilde{V}^{(2)}(q) \right). \tag{A.27}$$

Recalling (1.67) and taking into account that $\Pi(q) = \Pi(q, \omega = 0) \sim \text{const} \times q^2 + O(q^4)$ for $q \to 0$, one gets

$$E^{(1)}_{\text{Hartree pp}} - E^{(2)}_{\text{Hartree pp}} = \frac{\pi e^4}{\kappa^2} \lim_{q \to 0} \left(\frac{\Pi^{(2)}(q) - \Pi^{(1)}(q)}{q^2} \right). \tag{A.28}$$

Basing on this consideration, naively one might think that Hartree energies contribute to the population order reversal effect and that the contribution is characterized by the quantity $\lim_{q \to 0} \Pi(q)/q^2$. However, this consideration does

not take into account the electrostatic energy of interaction with the compensating positive charge (as the system is electrically neutral as a whole). Although, the screening processes happen at the BLG plane, they influence the interaction potential of charges outside of the plane.

Consider a simple model: the compensating positive charge is evenly distributed in the plane at a distance d from the BLG plane; for simplicity, all the system is in the environment with the dielectric constant $\kappa = 1$. Suppose the screening processes happen only in the BLG sheet. Then one can calculate the potential of interaction of the charges situated in different points of space. We are going to do that now.

We need several definitions: Coulomb electrostatic potential $\varphi(r = \sqrt{x^2+y^2+z^2}) = 1/r$, the spatial polarization function with screening happening only in the $z = 0$ plane $\Pi(\mathbf{r}) = \Pi(x, y, z) = \Pi(x, y)\delta(z)$[2], and their Fourier transforms w.r.t. plane coordinates x, y defined similarly to Eq. (1.31) and to Eq. (1.73) respectively: $\tilde{\varphi}(q = |\mathbf{q}|, z) = 2\pi \exp(-q|z|/l)/(ql)$ and $\Pi(q, z) = \Pi(q)\delta(z)$.

Then the interaction potential of two charges e_1 and e_2 placed in $\mathbf{r}$ and $\mathbf{r}'$ is

$$V_{\text{scr}}(\mathbf{r}, \mathbf{r}') = e_1 e_2 \varphi_{\text{scr}}(|\mathbf{x}-\mathbf{y}|, z, z') =$$
$$e_1 e_2 \varphi(\mathbf{r}, \mathbf{r}') -$$
$$- e_1 e_2 e^2 \int d^3x d^3y \varphi(|\mathbf{r}-\mathbf{x}|)\Pi(\mathbf{x}-\mathbf{y})\varphi(|\mathbf{y}-\mathbf{r}'|) +$$
$$+ e_1 e_2 e^4 \int d^3x d^3y d^3z d^3w \varphi(|\mathbf{r}-\mathbf{x}|)\Pi(\mathbf{x}-\mathbf{y})\varphi(|\mathbf{y}-\mathbf{z}|)\Pi(\mathbf{z}-\mathbf{w})\varphi(|\mathbf{w}-\mathbf{r}'|) -$$
$$- \ldots \quad \text{(A.29)}$$

Here e is the elementary charge — the absolute value of the charge of the electrons participating in the screening processes.

One can show then that the in-plane Fourier transform of the screened inter-

[2] $\delta(z)$ is the Dirac delta-function.

action potential of the two charges has the form

$$\tilde{V}_{\rm scr}(q,z,z',e_1,e_2) = e_1e_2\tilde{\varphi}_{\rm scr}(q,z,z') = e_1e_2\tilde{\varphi}(q,z-z') - e_1e_2\tilde{\varphi}(q,z)\frac{e^2l^2\Pi(q)}{1+e^2l^2\tilde{\varphi}(q,0)\Pi(q)}\tilde{\varphi}(q,-z') = e_1e_2\left(\frac{2\pi\exp\left(-q|z-z'|/l\right)}{ql} - \frac{2\pi\exp\left(-q|z|/l\right)}{ql}\frac{e^2l^2\Pi(q)}{1+e^2l^2\frac{2\pi}{ql}\Pi(q)}\frac{2\pi\exp\left(-q|z'|/l\right)}{ql}\right). \quad \text{(A.30)}$$

For $e_1 = e_2 = e$ and $z = z' = 0$ one restores the expression (1.31), as it should be.

The electrostatic energy of interaction of all the electrons in the fully filled LL and the charge-compensating background is equal to

$$E_{\rm Hartree} = e^2\int d^2x\ d^2y\rho(\mathbf{x})\rho(\mathbf{y})\left(\frac{1}{2}\varphi_{\rm scr}(|\mathbf{x}-\mathbf{y}|,z=z'=0) + \frac{1}{2}\varphi_{\rm scr}(|\mathbf{x}-\mathbf{y}|,z=z'=d) - \varphi_{\rm scr}(|\mathbf{x}-\mathbf{y}|,z=d,z'=0)\right). \quad \text{(A.31)}$$

Performing same operations as in the beginning of the current appendix for the Hartree energy of electrons in the LL only, we get:

$$E_{\rm Hartree} = \frac{e^2N_e}{2\pi}\lim_{q\to 0}\left(\frac{1}{2}\tilde{\varphi}_{\rm scr}(q,z=z'=0) + \frac{1}{2}\tilde{\varphi}_{\rm scr}(q,z=z'=d) - \tilde{\varphi}_{\rm scr}(q,z=d,z'=0)\right) = \frac{e^2N_e}{2\pi}\lim_{q\to 0}\left(\frac{2\pi(1-\exp\left(-qd/l\right))}{ql} - \frac{4\pi^2e^2\Pi(q)}{2q^2\left(1+e^2l^2\frac{2\pi}{ql}\Pi(q)\right)}(1+\exp\left(-2qd/l\right)-2\exp\left(-qd/l\right))\right) = \frac{e^2N_e}{2\pi}\frac{2\pi d}{l^2} = \frac{e^2N_ed}{l^2}, \quad \text{(A.32)}$$

where we have used the fact that $\Pi(q) = \Pi(q,\omega=0) \sim \text{const}\times q^2 + O(q^4)$ for $q\to 0$.

First of all, the answer does not depend on the polarization function $\Pi(q)$. Secondly, it coincides with the energy of a capacitor made of two parallel planes of area S at a distance d with charge $Q = eN_e$ on its plates. Indeed, such a capacitor has the capacitance $C = S/(4\pi d)$ and energy $E_{\text{cap}} = Q^2/(2C)$. Since $S = 2\pi l^2 N_e$, one easily finds that $E_{\text{Hartree}} = E_{\text{cap}}$.

So, in this simple model, the full Hartree energy of a filled Landau level and the compensating charge layer does not depend on screening. Of course, this model does not take into account many features of real experimental systems. However, it clearly illustrates that one can hardly expect to have different Hartree energies for differently screened potentials. Therefore, the Hartree energy does not contribute to the population reversal effect.

A.3 Peculiarities of calculations of virtual hopping corrections

In the paragraph 1.3.2.3 we presented the derivation of the corrections to the pseudopotentials which correspond to the diagram in Fig. 1.2b. The derivation presented there is based on a consideration of two interacting particles, which interact through the screened potential, within the methodology of quantum mechanics. In fact, the full expression for this correction comes from the consideration within the quantum field theory methodology and the second quantization approach. Thus, the diagram should take into account not only the potential screening but also the corrections to the electron propagator (self-energy), and also the dependence of the polarization function on the frequency (within the screened potential approach we neglect this dependence, and it is not important until the calculation of this correction). The applicability of the "quantum-mechanical" approximation is discussed in this appendix.

We denote the electron propagator as $G(\omega, \vec{q}_1, \vec{q}_2, j)$ (j is the LL in which the electron propagates; $\vec{q}_{1/2}$ are the 2-momentums — the electron propagator in uni-

form magnetic field is not translation-invariant, so it contains two momenta coming from the Fourier transforms with respect to two spatial coordinates). We denote the photonic propagator as $D(\omega, \vec{q})$ (it is translation-invariant, so depends only on one spatial momentum). Then the propagators can be expressed as follows (infinitely small imaginary parts of the denominators are not written out explicitly):

$$G(\omega, \vec{q}_1, \vec{q}_2, j) = \frac{f_j(\vec{q}_1, \vec{q}_2)}{\omega - E_j + \Sigma(\omega, \vec{q}_1, \vec{q}_2)}, \tag{A.33}$$

$$D(q) = \frac{v(\vec{q})}{1 + v(\vec{q}) \sum_{j',j''} (\frac{\Pi_{j',j''}(\vec{q})}{\omega - E_{j'} + E_{j''}} + \frac{\Pi_{j'',j'}(\vec{q})}{\omega - E_{j''} + E_{j'}})}, \tag{A.34}$$

$f_j(\vec{q})$ is a smooth function (without poles).

The diagram we are interested in can be expressed then via the propagators (we will need only the ω dependence for our analysis, so the dependence on the spatial momenta is not written explicitly):

$$Diag = \int_{\text{over momenta}} \int d\omega \; G(\omega, j_1) \times$$
$$D(E_1 - \omega) G(-\omega + E_1 + E_2, j_2) D(-\omega + E_1 + E_2 - E_4), \tag{A.35}$$

where E_i are the energies of the incoming and outcoming electrons, in our case those are all in one LL j: $E_i = E_j^{kin}$. j_1 and j_2 denote the levels to which the electrons hop, just like in the paragraph 1.3.2.3.

All the functions (propagators) participating in the expression are the time-ordered correlation functions at zero temperature and their poles are situated in such a way that one can do Wick rotation $\omega \to -i\omega$ (the zero of energies is the partially filled LL $E_j^{kin} = 0$). Then, concentrating on the denominators, we can

write the diagram via the integral over Euclidean frequency:

$$Diag \sim \int_{\text{over momenta}} \int d\omega \frac{...}{-i\omega - E^{kin}_{j_1} + \Sigma(...)} \times \frac{...}{i\omega - E^{kin}_{j_2} + \Sigma(...)} \times \frac{...}{1 + v(...) \sum_{j',j''} (\frac{\Pi_{j',j''}(...)}{i\omega - E^{kin}_{j'} + E^{kin}_{j''}} + \frac{\Pi_{j'',j'}(...)}{i\omega - E^{kin}_{j''} + E^{kin}_{j'}})} \times \frac{...}{1 + v(...) \sum_{j',j''} (\frac{\Pi_{j',j''}(...)}{i\omega - E^{kin}_{j'} + E^{kin}_{j''}} + \frac{\Pi_{j'',j'}(...)}{i\omega - E^{kin}_{j''} + E^{kin}_{j'}})}. \quad \text{(A.36)}$$

Evidently, the denominators of the electron propagators determine the region of frequencies which give dominating contribution to the integral. And this region is the interval centered at zero frequency with the width about the energy distance to the closest higher LL. Self-energy of the electron is proportional to the typical interaction energy $\sim e^2/(\kappa l)$. The self-energy can change the important frequencies region, for small enough interaction this should be just a change of the interval's width by something proportional to the $e^2/(\kappa l)$. Thus taking the self-energy into account or neglecting it changes the value of the diagram by a correction, introducing a relative error proportional to the ratio between the typical interaction energy and the distance to the closest higher LL.

Typical change of the photon propagator when one takes into account the frequency dependence of the polarization function (as compared to neglecting the dependence) inside the important region is also proportional to the ratio of the typical interaction energy to the distance to the closest LL (here — not necessarily higher).

Thus, taking into account the electron self-energy and the frequency dependence of the polarization function changes the diagram value (which itself is a small, not more than a 10% correction to the pseudopotential) by a relative correction of the order of the ratio of the typical interaction energy to the distance to the closest LL. This is the parameter which controls the level mixing, and in the region of applicability of the perturbative analysis it is smaller than 1. Deep in the

region of applicability the parameter is much less than 1, so it is only a small correction to a small correction, thus not important. However, in a realistic situation this ratio is around 0.5, so it can change the small correction to a pseudopotential from 5% of the pseudopotential to $2.5 - 7.5\%$. This may be significant.

However, taking into account that the effect of the corrections in the quantum-mechanical approximation is rather small quantitative than a qualitative one we would expect that taking the self-energy and the frequency dependence into account would only lead to small quantitative corrections. Taking into account the last argument and technical difficulties of such a calculation we do not deem at the moment that it is necessary to compute the diagram exactly.

A.4 Supplemental material

In this appendix we provide additional details regarding the stability of the Pfaffian state.

Figures A.1a and A.1b show the numerically found gap between the exact ground state of the system with 12 particles and its exact first excited state. In these figures, the gap is plotted as a function of the magnetic field and the dielectric constant at $U = 50$ meV for the $(1, -1)$ LL (Fig. A.1a) and at $U = 30$ meV for the $(2, -1)$ LL (Fig. A.1b) respectively. We do not show the data in the region where the perturbative analysis is not applicable according to type S estimate (with typical interaction energy scale needed for estimates taken to be the *screened* potential zeroth pseudopotential at the LL under consideration). The region of inapplicability of our theory according to the type C estimate (with typical interaction energy scale taken to be the bare *Coulomb* potential zeroth pseudopotential) is hatched. Figures A.2a and A.2b show the same data on the gaps in the units of typical Coulomb energy $e^2/(\kappa\ell)$, where ℓ is the magnetic length $\ell = \sqrt{\hbar c/(eB)}$.

As one can see, for both levels gaps increase as the magnetic field increases (staring from points where maximum overlap occurs) and as the dielectric constant

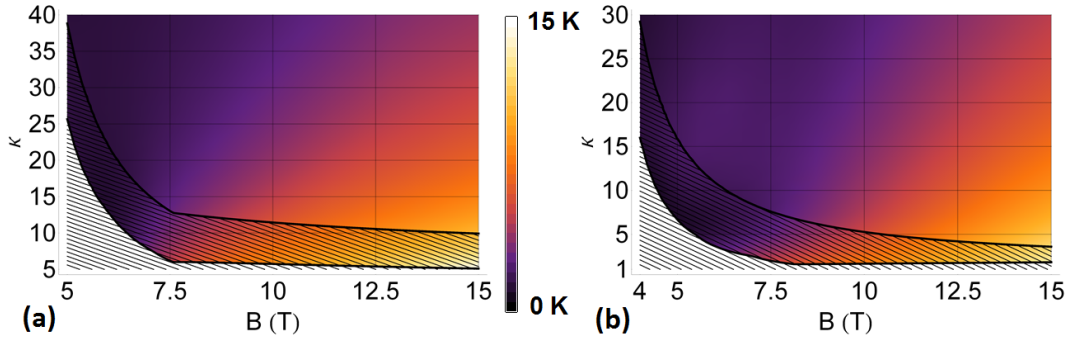

Figure A.1: **Color plot of the gap between the ground state and the first excited state computed for 12 particles as a function of the magnetic field B and the dielectric constant κ.** (a) – for the $(1,-1)$ LL at $U = 50$ meV, (b) – for the $(2,-1)$ LL at $U = 30$ meV. The region where perturbative analysis is not applicable according to the type C estimate is hatched. Data is not shown beyond the region where perturbative analysis is applicable according to the type S estimate.

decreases. This can be partially (for magnetic field) or fully (for the dielectric constant) attributed to the increase of $e^2/\kappa\ell$. This result, obtained for a finite number of particles, suggests that the system may still be in the same topological phase at higher magnetic fields. The same holds for low dielectric constants down to boundary of the perturbative approach applicability region: for smaller dielectric constants the physics is essentially non-single Landau level.

Figures A.3a and A.3b show the dependence of the gap on the magnetic field at $U = 50$ meV and $\kappa = 25$ for the $(1,-1)$ LL in K and in $e^2/(\kappa\ell)$ units respectively.

Figures A.4a and A.4b show the dependence of the gap on the dielectric constant at $U = 50$ meV and fixed $B = 6.5$ T for the $(1,-1)$ LL in K and in $e^2/(\kappa\ell)$ units respectively.

Figures A.5a and A.5b show the dependence of the gap on the magnetic field at $U = 30$ meV and $\kappa = 6, 12.5,$ and 25 for the $(2,-1)$ LL in K and in $e^2/(\kappa\ell)$ units respectively.

Figures A.6a and A.6b show the dependence of the gap on the dielectric constant at $U = 30$ meV and fixed $B = 8$ T for the $(2,-1)$ LL in K and in $e^2/(\kappa\ell)$ units respectively.

It is interesting to note that as a function of the magnetic field the gap has a dip around the point of maximum overlap with the Pfaffian state (see Fig. 1.5) in

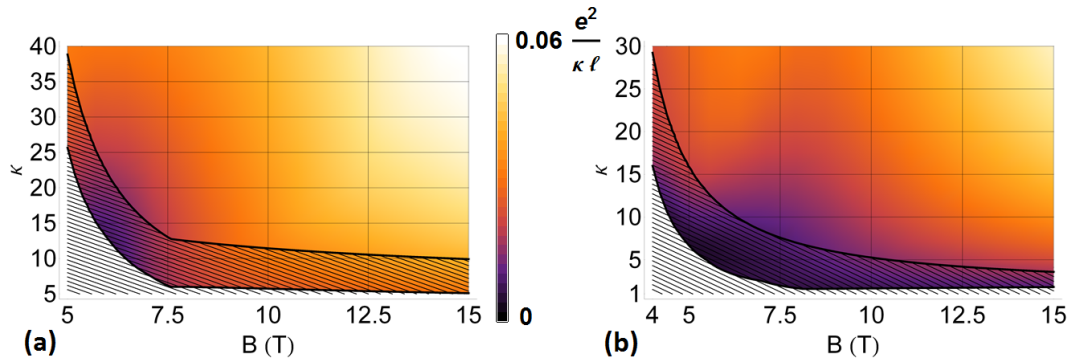

Figure A.2: **Color plot of the gap between the ground state and the first excited state computed for** 12 **particles as a function of the magnetic field** B **and the dielectric constant** κ**.** (a) – for the $(1,-1)$ LL at $U = 50$ meV, (b) – for the $(2,-1)$ LL at $U = 30$ meV. The region where perturbative analysis is not applicable according to the type C estimate is hatched. Data is not shown beyond the region where perturbative analysis is applicable according to the type S estimate.

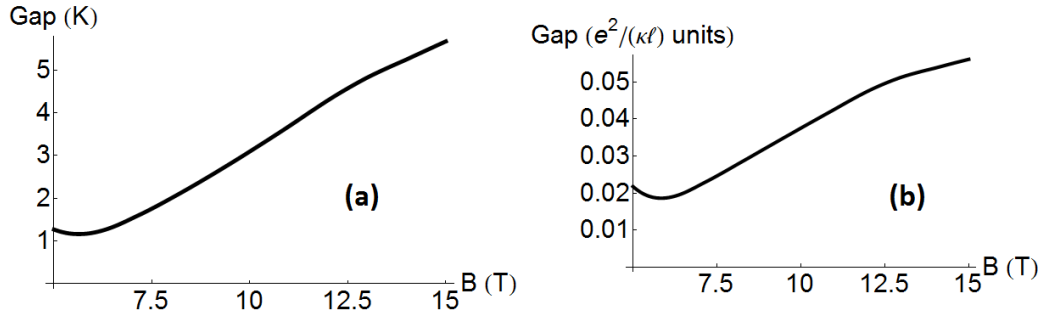

Figure A.3: **Dependence of the gap between the ground state and the first excited state computed for** 12 **particles at the** $(1,-1)$ **LL for** $U = 50$ **meV and** $\kappa = 25$ **as a function of the magnetic field** B**.** (a) – in K, (b) – in $e^2/(\kappa\ell)$ units. Only the part where perturbative analysis is applicable is shown.

all the cases both in K and in $e^2/(\kappa\ell)$ units.

Now we give some data on overlaps and gaps from numerical diagonalization for different numbers of particles $N = 8, 10, 12, 14$.

Figure A.7 compares the data on the overlap with the Pfaffian and the gap to the first excited state for the $(1,-1)$ and the $(2,-1)$ LLs in BLG and the non-relativistic $n = 1$ LL. The data are shown for different numbers of particles $N = 8, 10, 12, 14$. For the $(1,-1)$ and the $(2,-1)$ LLs in BLG external parameters are set to be near the maximum overlap regions at several values of the dielectric constant κ. The gap is presented in units of the typical Coulomb energy $e^2/\kappa\ell$. The results for BLG levels appear to be more stable as the number of particles

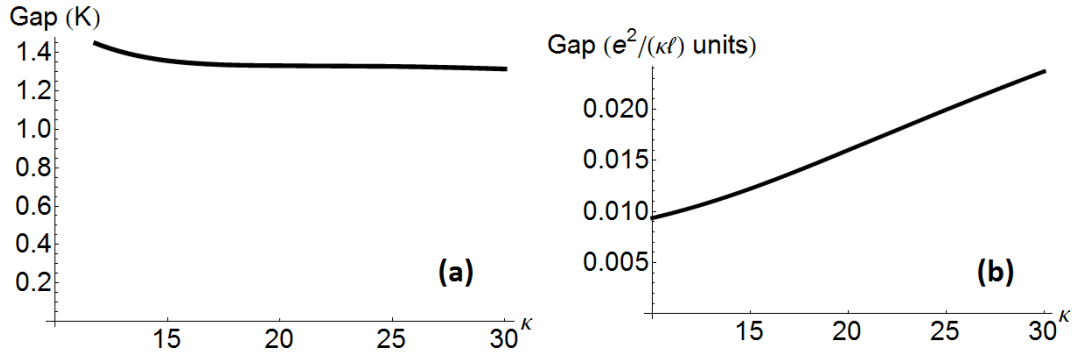

Figure A.4: **Dependence of the gap between the ground state and the first excited state computed for 12 particles at the $(1,-1)$ LL for $U = 50$ meV and $B = 6.5$ T as a function of the dielectric constant κ.** (a) – in K, (b) – in $e^2/(\kappa\ell)$ units. Only the part where perturbative analysis is applicable is shown.

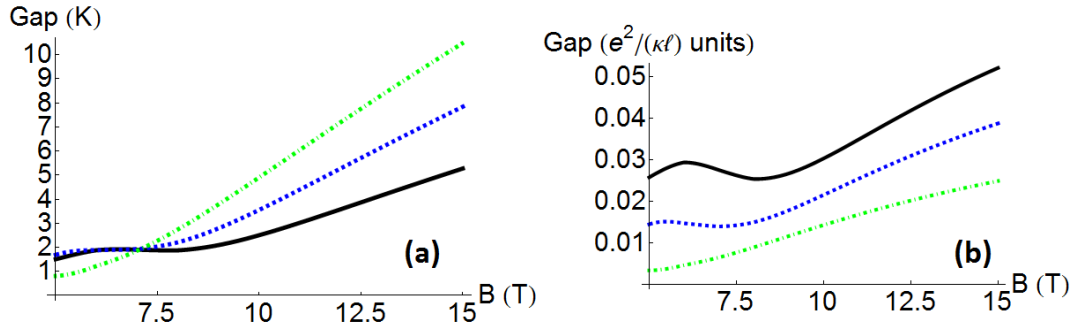

Figure A.5: **Dependence of the gap between the ground state and the first excited state computed for 12 particles at the $(2,-1)$ LL for $U = 30$ meV and $\kappa = 6$ (green dotdashed), 12.5 (blue dashed), and 25 (black solid line) as a function of the magnetic field B.** (a) – in K, (b) – in $e^2/(\kappa\ell)$ units. Only the part where perturbative analysis is applicable is shown.

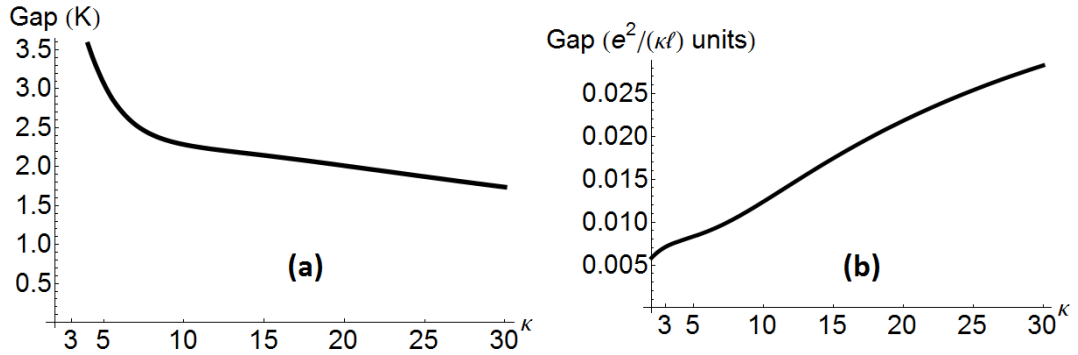

Figure A.6: **Dependence of the gap between the ground state and the first excited state computed for 12 particles at the $(2,-1)$ LL for $U = 30$ meV and $B = 8$ T as a function of the dielectric constant κ.** (a) – in K, (b) – in $e^2/(\kappa\ell)$ units. Only the part where perturbative analysis is applicable is shown.

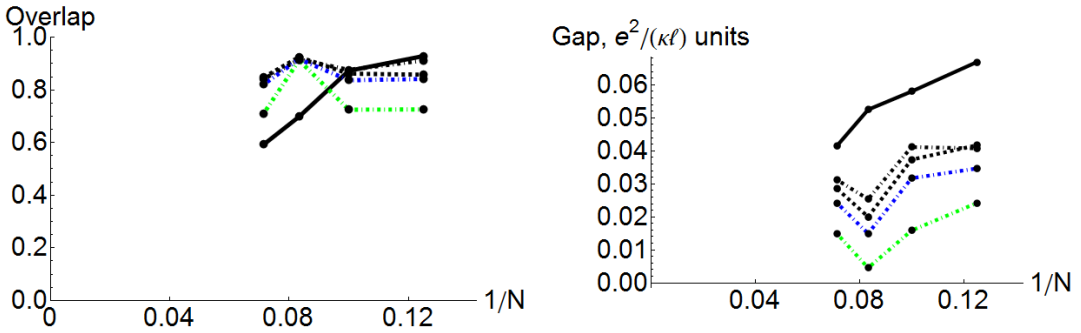

Figure A.7: **Dependence of the overlap with the Pfaffian and gap to the first excited state on the number of particles N ($N = 8, 10, 12, 14$).** Solid black line is for the non-relativistic $n = 1$ LL. Dashed black line is for the $(1, -1)$ LL at $U = 50$ meV, $\kappa = 25$ and $B = 6.5$ T. Dot-dashed lines are for the $(2, -1)$ LL at $U = 30$ meV, $\kappa = 25$ and $B = 8$ T (black), $\kappa = 12.5$ and $B = 8$ T (blue), $\kappa = 6$ and $B = 6$ T (green). The gap is presented in units of typical Coulomb energy $e^2/\kappa\ell$.

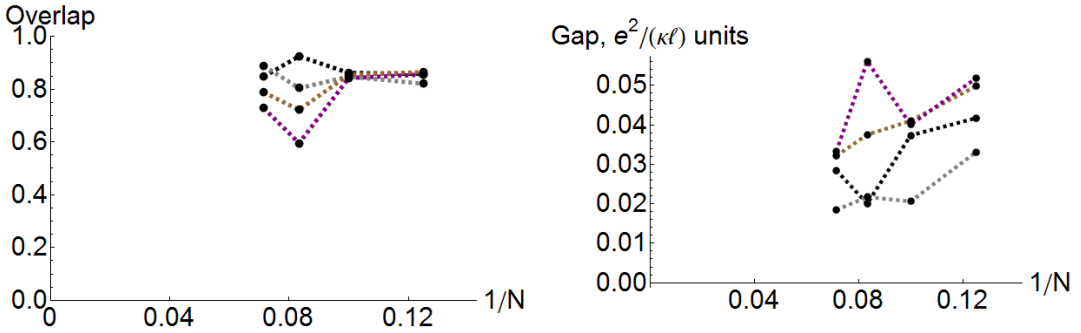

Figure A.8: **Dependence of the overlap with the Pfaffian and gap to the first excited state on the number of particles N ($N = 8, 10, 12, 14$) for the $(1, -1)$ LL at $U = 50$ meV, $\kappa = 25$.** Shown are the dependences for $B = 6.5$ T (dashed black line), $B = 5$ T (dashed grey line), $B = 10$ T (dashed brown line), and $B = 15$ T (dashed purple line).

grows than for the non-relativistic system.

Figures A.8, A.9, A.10, A.11, present the dependence of the overlap and the gap at several parameter points for $(1, -1)$ LL and $(2, -1)$ LL respectively. Points are taken to be at the same mini-gap and the dielectric constant values as in the previous figure, but the magnetic field changes. We took the points in the maximum overlap region, slightly to the left and to the right of it, and $B = 15$ T, which is a lot to the right of the high-overlap region.

Finally, figures A.12a and A.12b show the dependence of the overlap of the exact ground state of the system with the Pfaffian for $N = 12$ particles on the

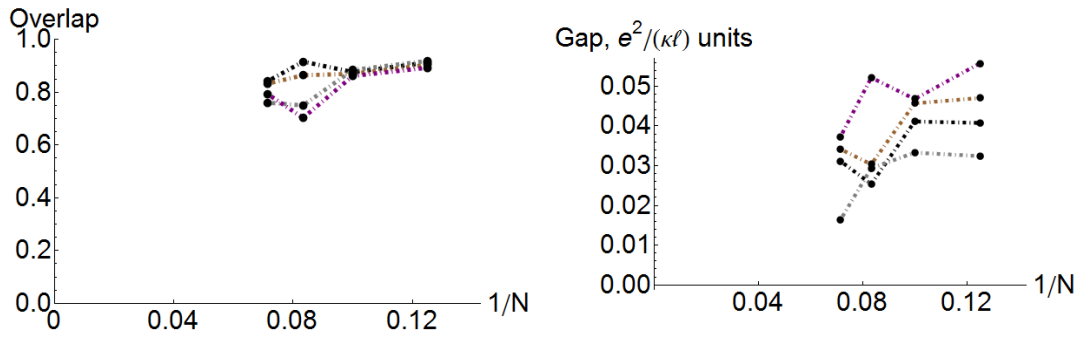

Figure A.9: **Dependence of the overlap with the Pfaffian and gap to the first excited state on the number of particles N ($N = 8, 10, 12, 14$) for the $(2, -1)$ LL at $U = 30$ meV, $\kappa = 25$.** Shown are the dependences for $B = 8$ T (dot-dashed black line), $B = 6$ T (dot-dashed grey line), $B = 10$ T (dot-dashed brown line), and $B = 15$ T (dot-dashed purple line).

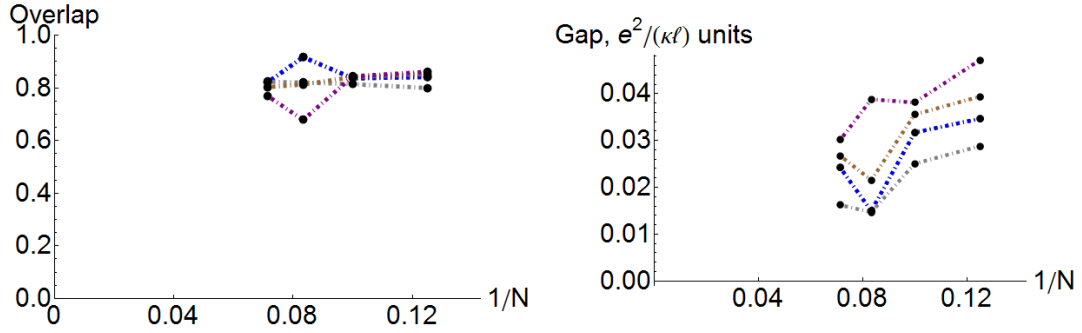

Figure A.10: **Dependence of the overlap with the Pfaffian and gap to the first excited state on the number of particles N ($N = 8, 10, 12, 14$) for the $(2, -1)$ LL at $U = 30$ meV, $\kappa = 12.5$.** Shown are the dependences for $B = 8$ T (dot-dashed blue line), $B = 6$ T (dot-dashed grey line), $B = 10$ T (dot-dashed brown line), and $B = 15$ T (dot-dashed purple line).

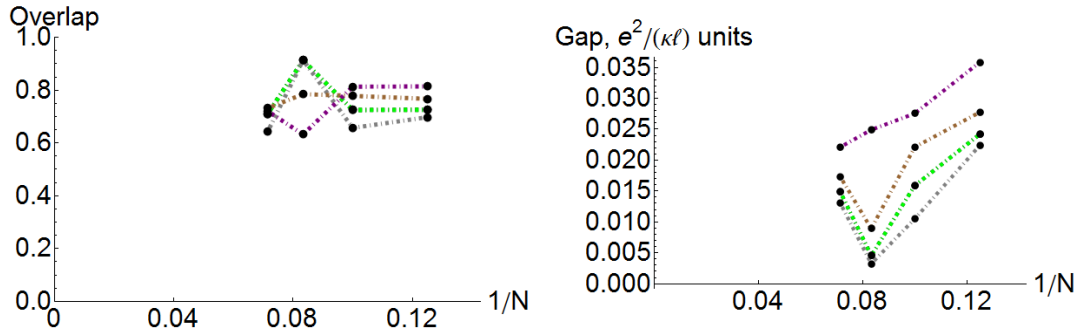

Figure A.11: **Dependence of the overlap with the Pfaffian and gap to the first excited state on the number of particles N ($N = 8, 10, 12, 14$) for the $(2, -1)$ LL at $U = 30$ meV, $\kappa = 6$.** Shown are the dependences for $B = 6$ T (dot-dashed green line), $B = 5$ T (dot-dashed grey line), $B = 8$ T (dot-dashed brown line), and $B = 15$ T (dot-dashed purple line).

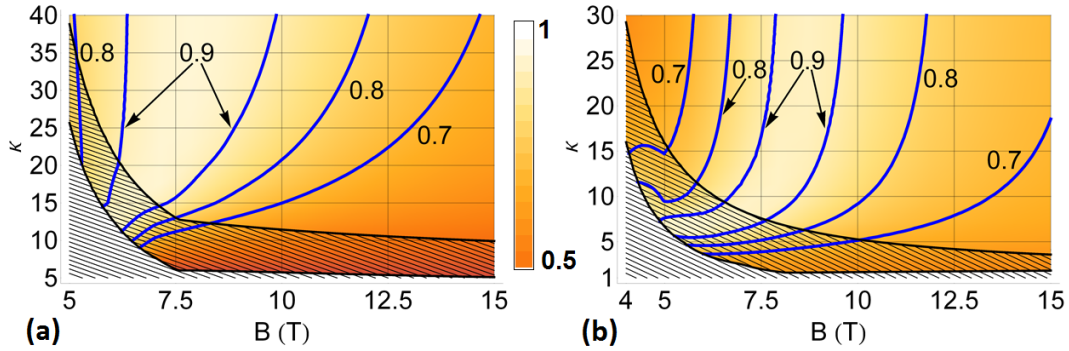

Figure A.12: **Color plot of the overlap of the ground state with the Moore-Read Pfaffian for** 12 **particles as a function of the magnetic field** B **and the dielectric constant** κ **with no virtual hopping corrections taken into account.** (a) – for the $(1,-1)$ LL at $U = 50$ meV, (b) – for the $(2,-1)$ LL at $U = 30$ meV. Contours show the lines of constant overlap. The region where perturbative analysis is not applicable according to the type C estimate is hatched. Data is not shown beyond the region where perturbative analysis is applicable according to the type S estimate.

magnetic field and the dielectric constant at $U = 50$ meV for the $(1,-1)$ LL and at $U = 30$ meV for the $(2,-1)$ LL respectively *with no virtual hopping to the nearby LL taken into account.* Screening is still taken into account. We do not show the data in the region where the perturbative analysis is not applicable according to type S estimate. The region of inapplicability of our theory according to the type C estimate is hatched. As one can see (compare with Fig. 1.5), within the region of applicability of perturbative treatment of LL mixing the effect virtual hopping corrections, defined in paragraph 1.3.2.3, have on the phase diagram is rather relatively small quantitative than a qualitative.

Appendix B

Appendices related to Chapter 2

B.1 Useful one-edge correlation functions

Here we give explicit expressions for the correlation functions at a single edge without tunnelling (described by the minimal model for $\nu = 2/3$ defined in the main text) which are used to calculate the quantities of experimental interest. In all the correlation functions of this appendix we assume the infinite system size limit $L \to \infty$.

The two-point correlation function of quasi-particle operators is equal to

$$\left\langle V^{\dagger}_{\mathbf{g}}(x_1,t_1)V_{\mathbf{g}'}(x_2,t_2)\right\rangle = \left\langle V_{-\mathbf{g}}(x_1,t_1)V_{\mathbf{g}'}(x_2,t_2)\right\rangle = \\ = \delta_{\mathbf{g},\mathbf{g}'}\prod_{p=c,n} F_p(x_1-x_2,t_1-t_2-i\varepsilon,\mathbf{g}) \quad \text{(B.1)}$$

$$F_p(x,t,\mathbf{g}) = \frac{(\pi T)^{g_p^2}}{(iv_p \sinh \pi T X_p)^{g_p^2}} \exp\left(iQ^{(p)}\mu^{(p)}X_p/v_p\right) \quad \text{(B.2)}$$

where $V_{\mathbf{g}}(x,t)$ is a quasiparticle excitation operator defined in Eq. (2.10), $\mathbf{g} = (g_1,g_2) = (g_c,g_n)$ is the excitation vector, p enumerates charged (c or 1) and neutral (n or 2) modes, $X_p = -\chi_p x + v_p t$, χ_p and v_p are the mode chirality and velocity respectively which enter the action (2.1) (in our case $\chi_1 = -\chi_2 = 1$), and T is the temperature of the edge. The electric charge $Q^{(c)} = Q = g_1'\sqrt{\nu}$, $\nu = 2/3$, $\mu^{(c)} = \mu$ is the chemical potential of the charged mode at the edge. It coincides with

the chemical potential of the Ohmic contact where the charged mode originates. The neutral charge $Q^{(n)} = g_2'$ and the chemical potential $\mu^{(n)}$ do not enter the formulae in chapter 2 as we assume $\mu^{(n)} = 0$, though, in principle, injection of the current from an Ohmic contact could shift the neutral mode chemical potential. We have also introduced an infinitesimally small positive number $\varepsilon \to +0$.

The electric current along the edge in the equilibrium is given by the average of the current operator $J^{\mu=1}$ defined in Eq. (2.5):

$$\left\langle J^1(x,t)\right\rangle = \chi_c v_c \left\langle J^0(x,t)\right\rangle = -v_c \frac{\sqrt{\nu}}{L} \left\langle \pi^0_{(c)}\right\rangle = \chi_c \frac{\nu}{2\pi}\mu^{(c)} = \frac{\nu}{2\pi}\mu^{(c)} \tag{B.3}$$

in agreement with the quantization law of Hall conductance [56].

The two-point correlation function of quasi-particle operators with the current operator inserted is given by

$$\begin{aligned}\left\langle J^1(x_0,t_0)V^\dagger_{\mathbf{g}}(x_1,t_1)V_{\mathbf{g}'}(x_2,t_2)\right\rangle = \\ = \left\langle V^\dagger_{\mathbf{g}}(x_1,t_1)V_{\mathbf{g}'}(x_2,t_2)\right\rangle \times \Big(\left\langle J^1(x_0,t_0)\right\rangle + \\ + \frac{Q^{(c)}\chi_c \pi T}{2\pi i}\left(\coth \pi T(Y_0 - Y_1) - \coth \pi T(Y_0 - Y_2)\right)\Big),\end{aligned} \tag{B.4}$$

where $Y_i = t - \chi_c x/v_c + i\kappa_i$. $\kappa_0 = 0$, $\kappa_1 = \kappa \to +0$ is an infinitesimally small positive number, $\kappa_2 = \kappa_1 + \varepsilon$, and ε is the same as in the two-particle correlation function.

Finally, the current-current correlation function is

$$\begin{aligned}\left\langle J^1(x_0,t_0)J^1(x_1,t_1)\right\rangle = \\ \left\langle J^1(x_0,t_0)\right\rangle\left\langle J^1(x_1,t_1)\right\rangle + \frac{\nu}{(2\pi)^2}\frac{(\pi T)^2}{(i\sinh \pi T(Y_0 - Y_1))^2},\end{aligned} \tag{B.5}$$

where $Y_i = t - \chi_c x/v_c + i\kappa_i$, $\kappa_0 = 0$, $\kappa_1 = \kappa \to +0$ is an infinitesimally small positive number.

B.2 Tunnelling current

Here a derivation of the expressions for the tunnelling current I_T and the tunnelling rate r is presented.

The tunnelling current can be defined as the time derivative of the total charge at the lower edge:

$$I_T = \frac{d}{dt}Q^{(l)} = i[H, Q^{(l)}] = i[H_T, Q^{(l)}], \tag{B.6}$$

$$Q^{(l)} = \int_{-\infty}^{\infty} J^{0(l)}(x,t)dx. \tag{B.7}$$

Here $J^{0(l)}$ is the lower edge charge density operator J^0 defined in Eq. (2.5), H is the full system Hamiltonian and H_T is the tunnelling Hamiltonian (2.28). Using the latter we get an explicit expression

$$I_{T,\mathrm{int}}(t) = i\sum_i Q_i\big(\eta_i A_i(t) - \eta_i^* A_i^\dagger(t)\big), \tag{B.8}$$

where Q_i are the quasiparticle charges Q in Table 2.1 and A_i are the operators defined in Eq. (2.29). This is the tunnelling current operator in the *interaction picture* with interaction H_T (which is emphasized by the subscript "int"). We calculate the expression for the tunnelling current operator in the *Heisenberg picture* within the perturbation theory in H_T:

$$\begin{aligned} I_T(t) = I_{T,\mathrm{int}}(t) + i\int_{-\infty}^{t} d\tau\,[H_T(\tau), I_{T,\mathrm{int}}(t)] + O(|\eta_i|^3) = \\ = i\sum_i Q_i\big(\eta_i A_i(t) - \eta_i^* A_i^\dagger(t)\big) - \\ - \sum_{i,j} Q_i \int_{-\infty}^{t} d\tau\left[\eta_j A_j(\tau) + \eta_j^* A_j^\dagger(\tau), \eta_i A_i(t) - \eta_i^* A_i^\dagger(t)\right] + O(|\eta_i|^3). \end{aligned} \tag{B.9}$$

The observed tunnelling current is then

$$\langle I_T(t)\rangle = \sum_i Q_i|\eta_i|^2 \int_{-\infty}^{t} d\tau \left\langle \left[A_i(\tau), A_i^\dagger(t)\right] - \left[A_i^\dagger(\tau), A_i(t)\right]\right\rangle + O(|\eta_i|^3). \quad \text{(B.10)}$$

We have used the relationships $\langle A_i(t)\rangle = \langle A_j(\tau)A_i(t)\rangle = 0$, $\left\langle A_j^\dagger(\tau)A_i(t)\right\rangle \propto \delta_{ij}$.

It can be checked with explicit correlation functions (B.2) that the integral of each of the summands in the formula (B.10) is convergent. Thus, one can split them and manipulate separately. Using time translational invariance of the correlation functions in both summands and changing sign of the integration variable in the second one we finally get

$$\langle I_T(t)\rangle = \sum_i Q_i|\eta_i|^2 \int_{-\infty}^{+\infty} d\tau \left\langle \left[A_i(\tau), A_i^\dagger(0)\right]\right\rangle + O(|\eta_i|^3), \quad \text{(B.11)}$$

which leads to the expression (2.30) for the tunnelling rate r.

B.3 Tunnelling current (continued)

Starting from the expression (B.11) for the tunnelling current expectation value and using the explicit form of the correlation functions (B.1) and (B.2), we obtain up to corrections of $O(|\eta_i|^3)$

$$\langle I_T(t)\rangle = 2i \sum_i Q_i|\eta_i|^2 v_c^{-4\delta} \left(\frac{v_c}{v_n}\right)^{2((\mathbf{g}_i)_2)^2} \times \int_{-\infty}^{+\infty} d\tau \frac{(\pi T_n)^{2\delta}(\pi T_s)^{2\delta} \sin Q_i \Delta\mu\tau}{(i\sinh \pi T_n(\tau - i\varepsilon))^{2\delta}(i\sinh \pi T_s(\tau - i\varepsilon))^{2\delta}}, \quad \text{(B.12)}$$

where $T_n = T^{(u)}$ is the upper edge temperature, $T_s = T^{(l)}$ is the lower edge temperature, $\Delta\mu = \mu^{(c,u)} - \mu^{(c,l)}$ is the difference of the chemical potentials of the upper and the lower edges' charged modes, the numbers $(\mathbf{g}_i)_1$, $(\mathbf{g}_i)_2$ are presented in the columns g_1, g_2 respectively of Table 2.1 for each of the three excitations

enumerated by i, and δ is the scaling dimension of the excitations presented in the column δ of Table 2.1, and $\varepsilon \to +0$ is an infinitesimally small positive number.

For $0 < \delta < 1/2$ the last formula can be further simplified:

$$I_T = \langle I_T(t) \rangle = \sum_i 4Q_i |\eta_i|^2 v_c^{-4\delta} \left(\frac{v_c}{v_n}\right)^{2((\mathbf{g}_i)_2)^2} \sin 2\pi\delta \int_0^{+\infty} d\tau \frac{(\pi T_n)^{2\delta}(\pi T_s)^{2\delta} \sin Q_i \Delta\mu\tau}{(\sinh \pi T_n \tau)^{2\delta}(\sinh \pi T_s \tau)^{2\delta}}. \quad \text{(B.13)}$$

B.4 Noise

In this appendix we derive expressions for the noise spectral density $S(\omega)$ at zero frequency ω.

The operator $I(t)$ of the full current flowing to the *Voltage probe* can be presented as a sum of the tunnelling current $I_T(t)$ defined in Eq. (B.9) and the current I_0 flowing along the lower edge just before the *QPC*:

$$I(t) = I_0(t) + I_T(t), \quad \text{(B.14)}$$

$$I_0(t) = J^{1(l)}(x = -0, t), \quad \text{(B.15)}$$

here $I(t)$ and $I_0(t)$ are operators in the *Heisenberg picture*.

The noise spectral density $S(\omega)$ defined in Eq. (2.31) then separates into four terms, see Eqs. (2.32) and (2.33), where the identity $S_{ab}(\omega) = S_{ba}(-\omega)$ following from the time translational invariance of the correlation functions has been used.

Using Eq. (B.5) one obtains

$$S_{00}(\omega = 0) = \frac{1}{2}\frac{\nu}{(2\pi)^2} \int_{-\infty}^{\infty} d\tau \frac{(\pi T^{(l)})^2}{(i \sinh \pi T^{(l)}(-\tau - i\varepsilon))^2} + \text{c.c.} = \frac{\nu}{2\pi} T^{(l)}, \quad \text{(B.16)}$$

where $T^{(l)}$ is the lower edge temperature, and $\varepsilon \to +0$ is an infinitesimally small positive number. This is the identity (2.34).

Since $\langle A_i(t) \rangle = 0$, $S_{TT}(\omega)$ can be expressed in the following way up to correc-

tions $O(|\eta_i|^3)$:

$$S_{TT}(\omega) = \int_{-\infty}^{\infty} d\tau \exp\bigl(i\omega\tau\bigr) \frac{1}{2} \Bigl\langle \Bigl\{ I_T(0), I_T(\tau) \Bigr\} \Bigr\rangle. \tag{B.17}$$

Using $\langle A_j(\tau) A_i(t) \rangle = 0$, $\Bigl\langle A_j^\dagger(\tau) A_i(t) \Bigr\rangle \propto \delta_{ij}$ and neglecting terms $O(|\eta_i|^3)$ we further simplify this expression to

$$S_{TT}(\omega) = \frac{1}{2} \sum_i Q_i^2 |\eta_i|^2 \int_{-\infty}^{\infty} d\tau \exp\bigl(i\omega\tau\bigr) \Bigl\langle \Bigl\{ A_i(0), A_i^\dagger(\tau) \Bigr\} \Bigr\rangle + \text{c.c.}, \tag{B.18}$$

which at $\omega = 0$ is equivalent to Eq. (2.35) due to the time translational invariance of the correlation functions.

Moving to $S_{0T}(\omega)$, we find up to the corrections $O(|\eta_i|^3)$ that

$$S_{0T}(\omega) = \frac{1}{2} \sum_i Q_i |\eta_i|^2 \int_{-\infty}^{\infty} d\tau \int_{-\infty}^{\tau} d\tau' \exp\bigl(i\omega\tau\bigr) \times \\ \times \Bigl\langle \Bigl\{ \Delta I_0(0), \Bigl[A_i(\tau'), A_i^\dagger(\tau) \Bigr] - \Bigl[A_i^\dagger(\tau'), A_i(\tau) \Bigr] \Bigr\} \Bigr\rangle. \tag{B.19}$$

In analogy with the calculation of the tunnelling current expectation value, the integral of each of the two summands in the last formula is convergent, thus we can manipulate the two summand integrals separately. Changing the order of integration and renaming $\tau \leftrightarrow \tau'$ in the second summand we arrive at the expression (2.36) for $\omega = 0$.

B.5 Noise — the TT term

Starting from the expression (2.35) for the TT component of the current noise and using the explicit form of the correlation functions (B.1) and (B.2), we obtain

up to corrections of $O(|\eta_i|^3)$

$$S_{TT}(0) = 2\sum_i Q_i^2 |\eta_i|^2 v_c^{-4\delta} \left(\frac{v_c}{v_n}\right)^{2((\mathbf{g}_i)_2)^2} \times \int_{-\infty}^{+\infty} d\tau \frac{(\pi T_n)^{2\delta}(\pi T_s)^{2\delta}\cos Q_i \Delta\mu\tau}{(i\sinh \pi T_n(\tau - i\varepsilon))^{2\delta}(i\sinh \pi T_s(\tau - i\varepsilon))^{2\delta}}, \quad \text{(B.20)}$$

where $T_n = T^{(u)}$ is the upper edge temperature, $T_s = T^{(l)}$ is the lower edge temperature, $\Delta\mu = \mu^{(c,u)} - \mu^{(c,l)}$ is the difference of the chemical potentials of the upper and the lower edges' charged modes, the numbers $(\mathbf{g}_i)_1$, $(\mathbf{g}_i)_2$ are presented in the columns g_1, g_2 respectively of Table 2.1 for each of the three excitations enumerated by i, and δ is the scaling dimension of the excitations presented in the column δ of Table 2.1, and $\varepsilon \to +0$ is an infinitesimally small positive number.

For $0 < \delta < 3/4$ the last formula can be rewritten as

$$S_{TT}(0) = 4\sum_i Q_i^2 |\eta_i|^2 v_c^{-4\delta} \left(\frac{v_c}{v_n}\right)^{2((\mathbf{g}_i)_2)^2} \cos 2\pi\delta \times \lim_{\varepsilon\to+0}\left(\int_{\varepsilon}^{+\infty} d\tau \frac{(\pi T_n)^{2\delta}(\pi T_s)^{2\delta}\cos Q_i\Delta\mu\tau}{(\sinh \pi T_n\tau)^{2\delta}(\sinh \pi T_s\tau)^{2\delta}} + \frac{\varepsilon^{1-4\delta}}{1-4\delta}\right). \quad \text{(B.21)}$$

B.6 Noise — the 0T term

Starting from the expression (2.36) for the $0T$ component of the current noise and using the explicit form of the correlation functions (B.1), (B.2), and (B.4), we obtain up to corrections of $O(|\eta_i|^3)$

$$S_{0T}(0) = \sum_i \frac{Q_i^2}{2\pi} |\eta_i|^2 v_c^{-4\delta} \left(\frac{v_c}{v_n}\right)^{2((\mathbf{g}_i)_2)^2} \times \int_{-\infty}^{+\infty} dt \int_{-\infty}^{+\infty} d\tau \frac{i(\pi T_n)^{2\delta}(\pi T_s)^{2\delta+1}\cos Q_i\Delta\mu(\tau - t)}{(i\sinh \pi T_n(\tau - t - i(\kappa - \varepsilon)))^{2\delta}(i\sinh \pi T_s(\tau - t - i(\kappa - \varepsilon)))^{2\delta}} \times (\coth \pi T_s(-\tau - i\varepsilon) - \coth \pi T_s(-t - i\kappa)) + \text{c.c.}, \quad \text{(B.22)}$$

where $T_n = T^{(u)}$ is the upper edge temperature, $T_s = T^{(l)}$ is the lower edge temperature, $\Delta\mu = \mu^{(c,u)} - \mu^{(c,l)}$ is the difference of the chemical potentials of the upper and the lower edges' charged modes, the numbers $(\mathbf{g}_i)_1$, $(\mathbf{g}_i)_2$ are presented in the columns g_1, g_2 respectively of Table 2.1 for each of the three excitations enumerated by i, and δ is the scaling dimension of the excitations presented in the column δ of Table 2.1, and $\varepsilon \to +0$, $\kappa \to +0$ are infinitesimally small positive numbers such that $\kappa > \varepsilon$.

It is tempting to integrate each of the two hyperbolic cotangents separately, however, the integrals of a signle cotangent diverge as t and τ go to $\pm\infty$ with $t-\tau$ being finite. Yet, the integral of the difference of the two cotangents is absolutely convergent. After a change of variables $\tau = t + y$ we get:

$$S_{0T}(0) = \sum_i \frac{Q_i^2}{2\pi} |\eta_i|^2 v_c^{-4\delta} \left(\frac{v_c}{v_n}\right)^{2((\mathbf{g}_i)_2)^2} \times$$
$$\times \int_{-\infty}^{+\infty} dy \int_{-\infty}^{+\infty} dt \frac{i(\pi T_n)^{2\delta}(\pi T_s)^{2\delta+1} \cos Q_i \Delta\mu y}{(i \sinh \pi T_n(y - i(\kappa-\varepsilon)))^{2\delta}(i \sinh \pi T_s(y - i(\kappa-\varepsilon)))^{2\delta}} \times$$
$$\times (\coth \pi T_s(-t - y - i\varepsilon) - \coth \pi T_s(-t - i\kappa)) + \text{c.c.} \quad \text{(B.23)}$$

Since

$$\int_{-\infty}^{+\infty} dt (\coth \pi T_s(-t - y - i\varepsilon) - \coth \pi T_s(-t - i\kappa)) =$$
$$= \int_{-\infty}^{+\infty} dt (\coth \pi T_s(t - y - i\varepsilon) - \coth \pi T_s(t - i\kappa)) =$$
$$\frac{1}{\pi T_s} \ln \frac{\sinh \pi T_s(t - y - i\varepsilon)}{\sinh \pi T_s(t - i\kappa)} \Bigg|_{-\infty}^{+\infty} = -2(y - i(\kappa - \varepsilon)), \quad \text{(B.24)}$$

we get

$$S_{0T}(0) = \sum_i \frac{2Q_i^2}{\pi}|\eta_i|^2 v_c^{-4\delta}\left(\frac{v_c}{v_n}\right)^{2((\mathbf{g}_i)_2)^2} \times$$
$$\times \int_{-\infty}^{+\infty} dy \frac{-i(\pi T_n)^{2\delta}(\pi T_s)^{2\delta+1}(y - i(\kappa-\varepsilon))\cos Q_i \Delta\mu y}{(i\sinh \pi T_n(y - i(\kappa-\varepsilon)))^{2\delta}(i\sinh \pi T_s(y - i(\kappa-\varepsilon)))^{2\delta}} =$$
$$= \sum_i \frac{2Q_i^2}{\pi}|\eta_i|^2 v_c^{-4\delta}\left(\frac{v_c}{v_n}\right)^{2((\mathbf{g}_i)_2)^2} \times$$
$$\times \int_{-\infty}^{+\infty} dy \frac{-i(\pi T_n)^{2\delta}(\pi T_s)^{2\delta+1} y\cos Q_i \Delta\mu y}{(i\sinh \pi T_n(y - i(\kappa-\varepsilon)))^{2\delta}(i\sinh \pi T_s(y - i(\kappa-\varepsilon)))^{2\delta}}. \quad \text{(B.25)}$$

For $0 < \delta < 1/2$ the last formula can be rewritten as

$$S_{0T}(0) = -4\sum_i \frac{Q_i^2}{\pi}|\eta_i|^2 v_c^{-4\delta}\left(\frac{v_c}{v_n}\right)^{2((\mathbf{g}_i)_2)^2} \sin 2\pi\delta \times$$
$$\int_0^{+\infty} d\tau \frac{(\pi T_n)^{2\delta}(\pi T_s)^{2\delta+1}\tau\cos Q_i\Delta\mu\tau}{(\sinh \pi T_n\tau)^{2\delta}(\sinh \pi T_s\tau)^{2\delta}}. \quad \text{(B.26)}$$

B.7 Excess noise

In the equilibrium ($\Delta\mu = 0$ and $T_n = T_s = T_0$) one can represent the integrals in formulae (B.21) and (B.26) in terms of Euler gamma function which leads to

$$S_{TT}(0)|_{\text{eq}} = 4\sum_i Q_i^2|\eta_i|^2 v_c^{-4\delta}\left(\frac{v_c}{v_n}\right)^{2((\mathbf{g}_i)_2)^2} \cos 2\pi\delta \times$$
$$(\pi T_0)^{4\delta-1}\frac{1}{2\sqrt{\pi}}\Gamma\left(\frac{1}{2} - 2\delta\right)\Gamma(2\delta), \quad \text{(B.27)}$$

$$S_{0T}(0)|_{\text{eq}} = -\frac{4}{\pi}\sum_i Q_i^2|\eta_i|^2 v_c^{-4\delta}\left(\frac{v_c}{v_n}\right)^{2((\mathbf{g}_i)_2)^2} \sin 2\pi\delta \times$$
$$(\pi T_0)^{4\delta-1}\frac{\sqrt{\pi}}{4}\cot(2\pi\delta)\Gamma\left(\frac{1}{2} - 2\delta\right)\Gamma(2\delta). \quad \text{(B.28)}$$

Thus,

$$S_{TT}(0)|_{\text{eq}} + 2S_{0T}(0)|_{\text{eq}} = 0. \tag{B.29}$$

Taking into account that the Johnson-Nyquist noise of the lower edge $S_{00}(0)$ does not depend on the currents I_n, I_s, we get the expression (2.38) for the excess noise $\tilde{S}(0)$.

B.8 Putting things together

The expressions (2.39)-(2.46) for the ratio X of the excess noise $\tilde{S}(0) = S_{TT}(0) + 2S_{0T}(0)$ (2.38) and the tunnelling rate $r = |I_T/I_s|$ (2.30) can be straightforwardly obtained using the explicit expressions for I_T, $S_{TT}(0)$, $S_{0T}(0)$ in formulae (B.13), (B.21), (B.26) respectively. We only changed the integration variable $\tau \to \pi T_s t$ and restored the fundamental constants: the elementary charge e, the Planck constant $h = 2\pi\hbar$, and the Boltzmann constant k_B.

We remind the reader that in the main text of the paper we assumed the neutral mode chemical potentials of both edges $\mu^{(n,u)}, \mu^{(n,l)}$ to be zero. However, if needed, the neutral mode chemical potentials can be easily incorporated into the formulae (2.42)-(2.45) by the substitution $Q_i j_s t \to \left(Q_i j_s - Q_i^{(n)}(\mu^{(n,u)} - \mu^{(n,l)})\right) t$. The neutral charges of the quasiparticles $Q_i^{(n)} = (\mathbf{g}_i)_2$ are given in the column g_2 of Table 2.1.

B.9 How general are the answers of the subsection 2.1.5?

The formulae (2.39)-(2.46) for the tunnelling rate, tunnelling current noise and their ratio within the second order perturbation theory in tunnelling Hamiltonian were obtained for the case of the minimal $\nu = 2/3$ edge model under certain phenomenological assumptions. However, these formulae and the calculations leading to them are straightforward to generalize to a much wider class of edge theories.

A general abelian QH edge theory can be constructed with the help of action (2.1) in the way outlined in subsection 2.1.4. One typically expects all the modes which carry electric charge to have same chirality χ_i. If a theory contains counter-flowing charged modes, in the low-energy limit it can become a theory with a set of charged modes propagating in one direction and a set of neutral modes (possibly, with different directions of propagation) according to the mechanism described in Refs. [27, 28].

Under the same assumptions on the interaction between the Ohmic contacts and the edge as were used in section 2.1, in the case of such theories one can show that the formulae (2.39)-(2.46) still hold for tunnelling of the quasiparticles with $\delta < 1/2$. The only adjustment which has to be made concerns the number of the parameters θ_i (according to the number of the most relevant excitations) and their definition (the ratio of the velocities becomes more complex if there are several charged or neutral modes, or disappears if there is only one mode in the model). For tunnelling of the quasiparticles with $\delta \geq 1/2$ only the formulae (2.42), (2.44), (2.45) should be modified with the terms cancelling divergencies of the integrals at $t \to 0$ similar to the $\varepsilon^{1-4\delta}$ term in Eq. (2.44).

A more general class of QH edge theories is where the charged sector is still described in terms of free bosons like in action (2.1), while the neutral sector is described in terms of a more complicated model — some conformal field theory (CFT). Examples of such edge theories can be found, e.g., in [49]. For more details on CFT see Ref. [57]. For the purposes of the present work it suffices to say that the second order perturbation theory results (2.39)-(2.46) hold for this class of models as well as they do for the abelian ones.

We remind the reader that the phenomenological assumptions from the subsection 2.1.3 are important for the derivation of the formulae (2.39)-(2.46). Some of these assumptions are not necessary for the derivation of the results of the subsection 2.2.2.[1] However, for simplicity, we do not release them. It is worth noting,

[1]For example, the assumption of the same temperature of all the edge modes at a given point can be weakened. Different temperatures of the different edge modes at the upper edge would

however, that the assumption that the lower edge temperature does not depend on the current I_s is crucial for the results of that subsection.

So, the formulae (2.39)-(2.46) (up to a modification of the number and the exact expression of the parameters θ_i) are valid for a wide class of typical abelian and non-abelian FQHE edge models.

B.10 Large I_s asymptotic behaviour of the noise to tunnelling rate ratio

Consider the large I_s limit of the Eq. (2.42). For $|j_s| \gg \lambda \geq 1$ one gets

$$G_i = \frac{j_s}{|j_s|} Q_i^{4\delta} |j_s|^{4\delta-1} \sin 2\pi\delta \times \left(\int_0^\infty dx \frac{\sin x}{x^{4\delta}} + O\left(\frac{\lambda^2}{Q_i^2 j_s^2}\right)\right) = \\ = \frac{j_s}{|j_s|} \frac{\pi}{2\Gamma(4\delta)} Q_i^{4\delta} |j_s|^{4\delta-1} \times \left(1 + O\left(\frac{\lambda^2}{Q_i^2 j_s^2}\right)\right), \quad \text{(B.30)}$$

where $\Gamma(x)$ is the Euler gamma function.

Similarly, for Eqs. (2.44), (2.45), (2.43) in the limit $|j_s| \gg \lambda \geq 1$ one gets

$$F_i^{TT} = \frac{\pi}{2\Gamma(4\delta)\cos 2\pi\delta} Q_i^{4\delta+1} |j_s|^{4\delta-1} \times \left(1 + O\left(\frac{\lambda^2}{Q_i^2 j_s^2}\right)\right), \quad \text{(B.31)}$$

$$F_i^{0T} = \frac{\pi(4\delta-1)}{2\Gamma(4\delta)\sin 2\pi\delta} Q_i^{4\delta} |j_s|^{4\delta-2} \times \left(1 + O\left(\frac{\lambda^2}{Q_i^2 j_s^2}\right)\right), \quad \text{(B.32)}$$

$$F_i = \frac{\pi}{2\Gamma(4\delta)} Q_i^{4\delta} |j_s|^{4\delta-2} \left(Q_i|j_s| + \frac{2-8\delta}{\pi} + O\left(\frac{\lambda^2}{Q_i|j_s|}\right)\right). \quad \text{(B.33)}$$

Using Eqs. (2.39)-(2.41), (B.30), (B.33) one finally gets the asymptotic expres-

not affect the results of that subsection concerning the large I_s asymptotic behaviour.

sion for the noise to tunnelling rate ratio (2.49):

$$X = \frac{\tilde{S}(0)}{r} = eI_s \frac{\sum_i \theta_i F_i}{\sum_i \theta_i G_i} = \\ = eI_s \frac{\sum_i \theta_i \left(Q_i^{4\delta+1}|j_s| + Q_i^{4\delta} \frac{2-8\delta}{\pi} + O\left(\frac{\lambda^2}{Q_i|j_s|}\right)\right)}{j_s \sum_i \theta_i Q_i^{4\delta} \left(1 + O\left(\frac{\lambda^2}{Q_i^2 j_s^2}\right)\right)} = \\ = e|I_s| \frac{\sum_i \theta_i Q_i^{4\delta+1}}{\sum_i \theta_i Q_i^{4\delta}} + eI_0 \frac{2-8\delta}{\pi} + O\left(|j_s|^{-1}\right). \quad \text{(B.34)}$$

B.11 Analytic expressions for NtTRR for equal temperatures of the upper and the lower edges

For the following derivation we need several facts about Euler beta function $\mathrm{B}(x, y)$ and Euler gamma function $\Gamma(x)$.

$$\Gamma(x)\Gamma(1-x) = \frac{\pi}{\sin \pi x}, \quad \text{(B.35)}$$

$$\Gamma(\bar{x}) = \overline{\Gamma(x)}, \quad \text{(B.36)}$$

$$\mathrm{B}(x, y) = \frac{\Gamma(x)\Gamma(y)}{\Gamma(x+y)}, \quad \text{(B.37)}$$

$$\mathrm{B}\Big(1 - 4\delta, \frac{\alpha}{2} + 2\delta\Big) = \int_0^\infty dt \frac{e^{-\alpha t}}{(\sinh t)^{4\delta}}. \quad \text{(B.38)}$$

The bars in the second equation denote complex conjugation. The last identity holds for $\delta < 1/4$ and $\mathrm{Re}\,[\alpha]\,/2 + 2\delta > 0$, where Re[...] denotes taking of the real part. However, with it can be analytically continued beyond these restrictions.

Throughout this appendix we consider the case of equal temperatures of the upper and the lower edge, i.e. $\lambda = 1$.

Using Eqs. (B.35)-(B.38), one can get the following analytic expressions for the

functions defined in Eqs. (2.42), (2.44):

$$G_i\,|_{\lambda=1} = \frac{Q_i 2^{4\delta-2}}{\Gamma(4\delta)}\left|\Gamma\left(2\delta+\frac{iQ_i j_s}{2}\right)\right|^2 \sinh\frac{\pi Q_i j_s}{2}, \tag{B.39}$$

$$F_i^{TT}\,|_{\lambda=1} = \frac{Q_i^2 2^{4\delta-2}}{\Gamma(4\delta)\cos 2\pi\delta}\left|\Gamma\left(2\delta+\frac{iQ_i j_s}{2}\right)\right|^2 \cosh\frac{\pi Q_i j_s}{2}. \tag{B.40}$$

For the function defined in Eq. (2.45), noting that[2]

$$F^{0T} = \frac{1}{\sin 2\pi\delta}\frac{\partial}{\partial j_s}G_i, \tag{B.41}$$

one gets

$$F_i^{0T}\,|_{\lambda=1} = \frac{Q_i^2 2^{4\delta-2}}{\Gamma(4\delta)\sin 2\pi\delta}\left|\Gamma\left(2\delta+\frac{iQ_i j_s}{2}\right)\right|^2 \sinh\frac{\pi Q_i j_s}{2}\times$$
$$\times\left(\frac{\pi}{2}\coth\frac{\pi Q_i j_s}{2}+\frac{i}{2}\psi\left(2\delta+\frac{iQ_i j_s}{2}\right)-\frac{i}{2}\psi\left(2\delta-\frac{iQ_i j_s}{2}\right)\right), \tag{B.42}$$

where the digamma function $\psi(x) = (\ln\Gamma(x))'$ is the logarithmic derivative of the Euler gamma function $\Gamma(x)$.

Thus, for F_i defined in Eq. (2.43) we have

$$F_i\,|_{\lambda=1} = \frac{Q_i^2 2^{4\delta-1}}{\pi\Gamma(4\delta)}\left|\Gamma\left(2\delta+\frac{iQ_i j_s}{2}\right)\right|^2 \sinh\frac{\pi Q_i j_s}{2}\mathrm{Im}\left[\psi\left(2\delta+\frac{iQ j_s}{2}\right)\right], \tag{B.43}$$

where Im[...] denotes taking of the imaginary part.

Using Eqs. (2.39)-(2.41), one straightforwardly gets the analytic expression for the noise to tunnelling rate ratio $X(I_s)\,|_{\lambda=1}$. In the case of coinciding charges of all the quasiparticles participating in tunnelling this expression simplifies significantly leading to the result (2.52).

[2] An interesting relation between this fact and the Ward identity arising due to the conservation of electric charge was noted in [58].

Bibliography

[1] Aveek Bid, Nissim Ofek, Hiroyuki Inoue, Moty Heiblum, C. L. Kane, Vladimir Umansky, and Diana Mahalu. Observation of neutral modes in the fractional quantum Hall regime. *Nature*, 466(7306):585–590, 2010.

[2] Quantum Hall effect, Wikipedia. http://en.wikipedia.org/wiki/quantum_hall_effect. Accessed on April 21, 2014.

[3] R.E. Prange and S.M. Girvin. *The Quantum Hall Effect*. Graduate Texts in Contemporary Physics. Springer-Verlag, 1990.

[4] C. Nayak, S. H. Simon, A. Stern, M. Freedman, and S. Das Sarma. Non-abelian anyons and topological quantum computation. *Reviews of Modern Physics*, 80(3):1083–1159, 2008.

[5] G. Moore and N. Read. Nonabelions in the fractional quantum Hall-effect. *Nuclear Physics B*, 360(2-3):362–396, 1991.

[6] V. M. Apalkov and T. Chakraborty. Stable Pfaffian state in bilayer graphene. *Physical Review Letters*, 107(18):5, 2011.

[7] GB Lesovik. Excess quantum noise in 2d ballistic point contacts. *ZhETF Pis ma Redaktsiiu*, 49:513, 1989. (JETP Lett. 49, 592 (1989)).

[8] R De-Picciotto, M Reznikov, M Heiblum, V Umansky, G Bunin, and D Mahalu. Direct observation of a fractional charge. *Nature*, 389(6647):162–164, 1997.

[9] L Saminadayar, DC Glattli, Y Jin, and B Etienne. Observation of the e/3 fractionally charged Laughlin quasiparticle. *Physical Review Letters*, 79(13):2526, 1997.

[10] F. D. M. Haldane. Fractional quantization of the Hall-effect - a hierarchy of incompressible quantum fluid states. *Physical Review Letters*, 51(7):605–608, 1983.

[11] M. R. Peterson, T. Jolicoeur, and S. Das Sarma. Orbital Landau level dependence of the fractional quantum Hall effect in quasi-two-dimensional electron layers: Finite-thickness effects. *Physical Review B*, 78(15):25, 2008.

[12] R. B. Laughlin. Anomalous quantum Hall-effect - an incompressible quantum fluid with fractionally charged excitations. *Physical Review Letters*, 50(18):1395–1398, 1983.

[13] D. S. L. Abergel, V. Apalkov, J. Berashevich, K. Ziegler, and T. Chakraborty. Properties of graphene: a theoretical perspective. *Advances in Physics*, 59(4):261–482, 2010.

[14] E. McCann and V. I. Fal'ko. Landau-level degeneracy and quantum Hall effect in a graphite bilayer. *Physical Review Letters*, 96(8):4, 2006.

[15] V. V. Cheianov, I. L. Aleiner, and V. I. Fal'ko. Gapped bilayer graphene: A tunable strongly correlated band insulator. *Physical Review Letters*, 109(10):5, 2012.

[16] R. Morf and N. d'Ambrumenil. Disorder in fractional quantum Hall states and the gap at $\nu = 5/2$. *Physical Review B*, 68(11):4, 2003.

[17] Maxim Kharitonov. Antiferromagnetic state in bilayer graphene. *Physical Review B*, 86(19):195435, 2012.

[18] Z. Papic, R. Thomale, and D. A. Abanin. Tunable electron interactions and fractional quantum Hall states in graphene. *Physical Review Letters*, 107(17):5, 2011.

[19] K. Snizhko, V. Cheianov, and S. H. Simon. Importance of interband transitions for the fractional quantum Hall effect in bilayer graphene. *Physical Review B*, 85(20):4, 2012.

[20] Dong-Keun Ki, Vladimir I Falko, Dmitry A Abanin, and Alberto Morpurgo. Observation of even denominator fractional quantum Hall effect in suspended bilayer graphene. *Nano Letters*, 2014.

[21] Z Papić and DA Abanin. Topological phases in the zeroth Landau level of bilayer graphene. *Physical Review Letters*, 112(4):046602, 2014.

[22] S. M. Song and B. J. Cho. Investigation of interaction between graphene and dielectrics. *Nanotechnology*, 21(33):6, 2010.

[23] K. I. Bolotin, F. Ghahari, M. D. Shulman, H. L. Stormer, and P. Kim. Observation of the fractional quantum Hall effect in graphene. *Nature*, 462:196, 2009.

[24] CR Dean, AF Young, P Cadden-Zimansky, L Wang, H Ren, K Watanabe, T Taniguchi, P Kim, J Hone, and KL Shepard. Multicomponent fractional quantum Hall effect in graphene. *Nature Physics*, 7(9):693–696, 2011.

[25] Patrick Maher, Lei Wang, Yuanda Gao, Carlos Forsythe, Takashi Taniguchi, Kenji Watanabe, Dmitry Abanin, Zlatko Papić, Paul Cadden-Zimansky, and James Hone. Tunable fractional quantum Hall phases in bilayer graphene. *arXiv preprint arXiv:1403.2112*, 2014.

[26] Xiao-Gang Wen. Theory of the edge states in fractional quantum Hall effects. *International Journal of Modern Physics B*, 6(10):1711–1762, 1992.

[27] C. L. Kane and Matthew P. A. Fisher. Impurity scattering and transport of fractional quantum Hall edge states. *Physical Review B*, 51(19):13449–13466, 1995.

[28] C. L. Kane, Matthew P. A. Fisher, and J. Polchinski. Randomness at the edge: Theory of quantum Hall transport at filling $\nu = 2/3$. *Physical Review Letters*, 72(26):4129–4132, 1994.

[29] I. L. Aleiner and L. I. Glazman. Novel edge excitations of two-dimensional electron liquid in a magnetic field. *Physical Review Letters*, 72(18):2935–2938, 1994.

[30] Yaron Gross, Merav Dolev, Moty Heiblum, Vladimir Umansky, and Diana Mahalu. Upstream neutral modes in the fractional quantum Hall effect regime: Heat waves or coherent dipoles. *Physical Review Letters*, 108(22):226801, 2012.

[31] Zi-Xiang Hu, Hua Chen, Kun Yang, E. H. Rezayi, and Xin Wan. Ground state and edge excitations of a quantum Hall liquid at filling factor 2/3. *Physical Review B*, 78(23):235315, 2008.

[32] Ying-Hai Wu, G. J. Sreejith, and Jainendra K. Jain. Microscopic study of edge excitations of spin-polarized and spin-unpolarized $\nu = 2/3$ fractional quantum Hall effect. *Physical Review B*, 86(11):115127, 2012.

[33] Aveek Bid, N. Ofek, M. Heiblum, V. Umansky, and D. Mahalu. Shot noise and charge at the 2/3 composite fractional quantum Hall state. *Physical Review Letters*, 103(23):236802, 2009.

[34] Jianhui Wang, Yigal Meir, and Yuval Gefen. Edge reconstruction in the $\nu = 2/3$ fractional quantum Hall state. *Physical Review Letters*, 111(24):246803, 2013.

[35] D. Ferraro, A. Braggio, N. Magnoli, and M. Sassetti. Charge tunneling in fractional edge channels. *Physical Review B*, 82(8):085323, 2010.

[36] X. G. Wen. Chiral Luttinger liquid and the edge excitations in the fractional quantum Hall states. *Physical Review B*, 41(18):12838–12844, 1990.

[37] J Fröhlich and T Kerler. Universality in quantum Hall systems. *Nuclear Physics B*, 354(2):369–417, 1991.

[38] Ivan P Levkivskyi, Alexey Boyarsky, Jürg Fröhlich, and Eugene V Sukhorukov. Mach-Zehnder interferometry of fractional quantum Hall edge states. *Physical Review B*, 80(4):045319, 2009.

[39] X. G. Wen. Electrodynamical properties of gapless edge excitations in the fractional quantum Hall states. *Physical Review Letters*, 64(18):2206–2209, 1990.

[40] A. H. MacDonald. Edge states in the fractional-quantum-Hall-effect regime. *Physical Review Letters*, 64(2):220–223, 1990.

[41] P. Fendley, A. W. W. Ludwig, and H. Saleur. Exact nonequilibrium transport through point contacts in quantum wires and fractional quantum Hall devices. *Physical Review B*, 52(12):8934–8950, 1995.

[42] C. L. Kane and Matthew P. A. Fisher. Nonequilibrium noise and fractional charge in the quantum Hall effect. *Physical Review Letters*, 72(5):724–727, 1994.

[43] So Takei and Bernd Rosenow. Neutral mode heat transport and fractional quantum Hall shot noise. *Physical Review B*, 84(23):235316, 2011.

[44] Th Martin and R. Landauer. Wave-packet approach to noise in multichannel mesoscopic systems. *Physical Review B*, 45(4):1742–1755, 1992.

[45] A. M. Chang. Chiral Luttinger liquids at the fractional quantum Hall edge. *Reviews of Modern Physics*, 75(4):1449–1505, 2003.

[46] M. Grayson, D. C. Tsui, L. N. Pfeiffer, K. W. West, and A. M. Chang. Continuum of chiral Luttinger liquids at the fractional quantum Hall edge. *Physical Review Letters*, 80(5):1062–1065, 1998.

[47] M Heiblum. Quantum shot noise in edge channels. *physica status solidi (b)*, 243(14):3604–3616, 2006.

[48] Artur O. Slobodeniuk, Ivan P. Levkivskyi, and Eugene V. Sukhorukov. Equilibration of quantum Hall edge states by an Ohmic contact. *Physical Review B*, 88(16):165307, 2013.

[49] Alexey Boyarsky, Vadim Cheianov, and Jürg Fröhlich. Effective-field theories for the $\nu = 5/2$ quantum Hall edge state. *Physical Review B*, 80(23):233302, 2009.

[50] Iuliana P Radu, JB Miller, CM Marcus, MA Kastner, LN Pfeiffer, and KW West. Quasi-particle properties from tunneling in the $\nu = 5/2$ fractional quantum Hall state. *Science*, 320(5878):899–902, 2008.

[51] Stefano Roddaro, Vittorio Pellegrini, Fabio Beltram, Giorgio Biasiol, Lucia Sorba, Roberto Raimondi, and Giovanni Vignale. Nonlinear quasiparticle tunneling between fractional quantum Hall edges. *Physical Review Letters*, 90(4):046805, 2003.

[52] Stefano Roddaro, Vittorio Pellegrini, Fabio Beltram, Loren N Pfeiffer, and Ken W West. Particle-hole symmetric luttinger liquids in a quantum Hall circuit. *Physical Review Letters*, 95(15):156804, 2005.

[53] P Fendley, AWW Ludwig, and H Saleur. Exact nonequilibrium dc shot noise in Luttinger liquids and fractional quantum Hall devices. *Physical Review Letters*, 75(11):2196, 1995.

[54] P Fendley and H Saleur. Nonequilibrium dc noise in a Luttinger liquid with an impurity. *Physical Review B*, 54(15):10845, 1996.

[55] Hiroyuki Inoue, Anna Grivnin, Yuval Ronen, Moty Heiblum, Vladimir Umansky, and Diana Mahalu. Proliferation of neutral modes in fractional quantum Hall states. *arXiv preprint arXiv:1312.7553*, 2013.

[56] Anton Yu Alekseev, Vadim V. Cheianov, and Jürg Fröhlich. Comparing conductance quantization in quantum wires and quantum Hall systems. *Physical Review B*, 54(24):R17320–R17322, 1996.

[57] P. Di Francesco, P. Mathieu, and D. Senechal. *Conformal Field Theory.* Springer, 1997.

[58] Olaf Smits, JK Slingerland, and Steven H Simon. Non-equilibrium noise in the (non-) Abelian fractional quantum Hall effect. *arXiv preprint arXiv:1401.4581*, 2014.